# PHYSICAL PROPERTIES OF NANOTUBE MATERIALS

by

John F. Niven

Submitted in partial fulfillment of the
requirements for the degree of
Master of Science

at

Dalhousie University
Halifax, Nova Scotia
July 2015

*For my Grandfather.*

# Table of Contents

# List of Tables

# List of Figures

## Abstract

Nanotubes, including carbon nanotubes (CNTs) and boron nitride nanotubes (BNNTs), are monolayer tubes with diameters on the order of nanometers and lengths up to millimetres. CNTs have outstanding properties at the individual nanotube level, including high strength, flexibility, and high thermal and electrical conductivities. These properties have inspired potential applications such as transparent electrodes, supercapacitors, nanoscale electronics, and nanocomposites. However, to be utilized in real-world applications, novel 3D macroscopic CNT materials must be designed, and their physical properties must be understood and optimized.

Although macroscopic CNT materials such as sheets and yarns show promise for their high strength, low density, and high conductivities, their properties are still orders of magnitude lower than those of individual CNTs. One feasible route to improve these properties is high-temperature thermal annealing, which has been shown to improve the crystallinity and transport properties of CNT materials.

In this work, CNT yarns were prepared and annealed at temperatures up to 2700 °C in Ar atmosphere. Raman spectroscopy showed a four fold increase in the relative CNT crystallinity after annealing to 2700 °C. The thermal and electrical conductivities of yarns with annealing temperature of 2300 °C and 2700 °C and diameters between 35 to 60 $\mu$m were measured as a function of temperature. Both conductivities increased by over 200 % at 300 K after annealing. Other properties studied include IV-curves, magnetoresistance, and the effects of adsorbed $O_2$and $H_2O$.

In addition, the thermal conductivities of various boron nitride nanotube materials were measured, and initial measurements were carried out for the thermal conductivities of $\sim$10 $\mu$m reactor-spun CNT fibres.

## List of Abbreviations and Symbols Used

$A$ . . . . . cross-sectional area

$a$ . . . . . lattice parameter

$\vec{a}_1$ . . . . . unit vectors

$A$, $B$, $C$ . . . . . constants

AP . . . . . as-prepared BNNT sheet

$\beta$ . . . . . force constant

BNNT . . . . . boron nitride nanotube

BP . . . . . BNNT buckypaper

$C$ . . . . . heat capacity per unit volume

$\mathbf{C}_h$ . . . . . chiral vector

CNT . . . . . carbon nanotube

CVD . . . . . chemical vapour deposition

$\Delta T$ . . . . . a temperature difference

$d$ . . . . . diameter

$\omega(k)$ . . . . . dispersion relation

DOS . . . . . density of states

$e$ . . . . . elementary charge

$E_F$ . . . . . Fermi energy

$E_g$ . . . . . energy gap

FIB . . . . . focused ion beam

FWHM . . . . . full-width at half maximum

$\mathbf{G}$ . . . . . a reciprocal lattice vector

$H$ . . . . . magnetic field

$h$ . . . . . Planck constant = $6.62606957\times10^{-34}$ J·s

$H$ . . . . . Hamiltonian operator

h-BN . . . . . hexagonal boron nitride

$I$ . . . . . electric current

$J_x$ . . . . . current flux

$K$ . . . . . thermal conductance

$k$, $k_x$, $k_y$, $k_z$ . . . . . wave vectors

$\kappa_{app}$ . . . . . apparent thermal conductivity

$\kappa$ . . . . . thermal conductivity

$k_B$ . . . . . Boltzmann constant = $1.3806488\times10^{-23}$ $\mathrm{m^2{\cdot}kg{\cdot}s^{-2}{\cdot}K^{-1}}$

$L$ . . . . . sample length

$L_0$ . . . . . Lorenz number, $L_0 \approx 2.44 \times 10^{-8}$ W $\Omega$ $\mathrm{K^{-2}}$ for metals.

$\lambda$ . . . . . mean free path

$M_1$, $M_2$ . . . . . atomic masses

$m_e$ . . . . . electron mass

$\mu$ . . . . . chemical potential

MWCNT . . . . . multi-walled carbon nanotube

$N$ . . . . . number of samples

$(n, m)$ . . . . . chiral indices

NP . . . . . nano-particle

$\nu$ . . . . . mean speed of sound

PPMS . . . . . Physical Properties Measurement System

$\psi$ . . . . . electron wave function

PTC . . . . . parallel thermal conductance

PVD . . . . . physical vapour deposition

$\mathbf{Q}$ . . . . . heat flux through a material

$R$ . . . . . electrical resistance

$\mathbf{r}$ . . . . . position vector

$r$ . . . . . radius

RBM . . . . . radial breathing mode

$\rho$ . . . . . density

sccm . . . . . standard cubic centimeters per minute

SEM . . . . . scanning electron microscopy

$\sigma$ . . . . . electrical conductivity

SWCNT . . . . . single-walled carbon nanotube

$T_0$, $T_s$, $T_m$, $T_p$ . . . . . fit parameters

$\tau$ . . . . . residual twist density

TEM . . . . . transmission electron microscopy

$T$ . . . . . temperature

TGA . . . . . thermogravimetric analysis

$\theta$ . . . . . an angle

$\mathbf{T}$ . . . . . translational vector

$u$, $v$ . . . . . atomic displacements

$V$ . . . . . voltage

$v_g$ . . . . . group velocity

VRH . . . . . variable range hopping

XRD . . . . . x-ray diffraction

## Acknowledgements

I would like to thank Professor Mary Anne White for her supervision and inspiration over the past several years several years, first while I was a summer student, then an honours student, and finally as a Masters student.

A special thanks to Mike Johnson for his tireless and invaluable assistance with the Physical Properties Measurement System during my work. Thanks also to Stefan Jukes for his assistance with various measurements, Jan Pöhls for useful discussions and comments, and the other current and former White group members for making the lab an enjoyable place to work.

I am extremely grateful to the members of the Nanoworld Laboratories at the University of Cincinnati, led by Dr. Vesselin Shanov and Dr. Mark Shultz, for allowing me to use their facilities. Specifically I would like to thank Dr. Noe Alvarez for his assistance with the production of the CNT yarns, and Aaron Johnson for his assistance with high-temperature annealing.

I would also like to thank Dr. Mike Jakubinek at the National Research Council Canada for providing the boron nitride nanotube materials, Professor Alan Windle and Dr. Thurid Gspann from the University of Cambridge for providing CNT fibre samples, and finally, Andy George and Patricia Scallion for assistance with SEM measurements.

I also gratefully acknowledge financial support from NSERC, IRM, and the Nova Scotia Research and Innovation Graduate Scholarship, without whom this work could not have been done.

Finally, and most importantly, a huge thanks my girlfriend Katie, my parents, and the rest of my family for their love, support, and understanding during my time at Dalhousie.

# Chapter 1

# Introduction

Modern technology continues to push the limits of materials science, demanding increasingly light-weight, energy efficient, cost-effective, and sustainable materials. For decades nano-scale materials have been touted as one way to meet these demands. Nanotubes, including carbon nanotubes (CNTs) and boron nitride nanotubes (BNNTs) are among the most exciting nanomaterials.

Carbon nanotubes are hollow graphene cylinders with diameters typically between 2 nm and 20 nm. CNTs are the most studied nanomaterial because of their unique combination of excellent mechanical [1], thermal [2], and electrical properties [3]. Carbon nanotubes have been researched extensively for the past two decades, with the publication rate now at 20,000 per year according to Web of Science.

Although the properties of individual CNTs are extremely exciting, most real-world applications of CNTs require 3D bulk CNT materials, including arrays [4], sheets [5], and yarns [6]. These materials have shown promise for a variety of applications. However, the synthesis and processing of CNT yarns involves a large number variables, which has slowed understanding of the structure-property relationships.

This thesis focuses on the physical properties of three types of bulk nanotube materials: array-spun CNT yarns; reactor-spun CNT yarns; and BNNT sheets and composites.

The main goal was to understand how high-temperature annealing affects the thermal and electrical properties of CNT yarns. CNT yarns were produced by the author at the University of Cincinnati in collaboration with the Nanoworld Laboratories. This work clearly demonstrates the simultaneous improvement of the electrical and thermal conductivities of the CNT yarns, showing that high-temperature annealing could be a viable method to optimize the properties of CNT yarns.

Chapter 2 provides an introduction to the electrical and thermal properties of materials, and Chapter 3 discusses the structure and properties of CNTs and CNT

materials. Chapters 4 and 5 present the synthesis and physical properties of the CNT yarns studied in this work.

Chapter 6 presents the synthesis and thermal conductivities of two small diameter reactor-spun CNT fibres, provided by Professor Alan Windle's group at the University of Cambridge. The thermal conductivities of these fibres are the highest values of any CNT fibre reported to date.

Chapter 6 also presents BNNT sheets, buckypapers, and composites. These materials were produced at the National Research Council Canada (NRC), Emerging Technologies Division, in collaboration with Dr. Mike Jakubinek. The induction thermal plasma method developed at NRC produces small-diameter, highly crystalline BNNTs at record-setting rates of 20 grams per hour. These measurements are the first direct thermal conductivity measurements made on bulk BNNT materials to date.

# Chapter 2

# Electrical and Thermal Properties of Materials

## 2.1 Electrical Conductivity

Electrical conductivity, $\sigma$, describes a material's ability to conduct electrical current, and is measured by passing one-dimensional current along one direction of a sample with flux, $J_x$, such that:

$$J_x = \sigma_x E_x. \tag{2.1}$$

Experimentally, $\sigma$ is calculated by measuring the electrical resistance, $R$, and external dimension of a sample. The resistance of an object is given by Ohm's law,

$$R = \frac{V}{I}, \tag{2.2}$$

where $V$ is the voltage across the sample and $I$ is the current through the sample.

The material's conductivity, $\sigma$ (and resistivity, $\rho$) are then defined by:

$$\sigma = \rho^{-1} = \frac{1}{R}\frac{L}{A}, \tag{2.3}$$

where $L$ is the sample length and $A$ is the cross-sectional area of the sample along the direction of current flow. Electrical conductivity is an intrinsic property of the material and is independent of the sample dimensions for homogeneous materials, although conductivity is temperature dependent. Therefore, the electrical conductivity at a given temperature of a material with known dimensions can be calculated by measuring the electrical resistance, $R$.

The values of $\sigma$ range several orders of magnitude, from $> 10^4$ S·m$^{-1}$ for metals, to $10^{-3}$ to $10^3$ S·m$^{-1}$ for semiconductors, and $10^{-3}$ S·m$^{-1}$ to $10^{-18}$ S·m$^{-1}$ for insulators [7]. Superconductors are another class of materials in which electrical resistance drops to zero ($\sigma \to \infty$), as the temperature is dropped below a transition temperature [8].

### 2.1.1 Free-Electron Theory

In metals, conduction electrons are delocalized and can therefore move easily through the lattice, resulting in a high $\sigma$ [8]. Because the electrons in metals are so delocalized, they can be modelled as a "gas" of electrons, free to move throughout the metal. The free-electron gas theory can be used to describe the electrical conductivity, thermal conductivity, and heat capacity of metals.

The possible energy levels of the free-electrons ($E_k$) are given by the Schrödinger equation [8]:

$$H\psi_k = -\frac{\hbar^2}{2m_e}\nabla^2\psi_k(\mathbf{r}) = E_k\psi_k, \tag{2.4}$$

where $\psi_k$ is the wave function of an electron of wave vector $k$, $m_e$ is the electron mass, and $\hbar = h/2\pi$ is the Dirac constant. The solutions to Equation 2.4 for the wavefunction and energy of a particle in a 3D box of length $L$ are:

$$\psi_k(\mathbf{r}) = \frac{1}{\sqrt{L^3}}e^{ik\cdot\mathbf{r}} \tag{2.5}$$

and

$$E_n = \frac{\hbar^2}{2m_e}k^2 = \frac{\hbar^2}{2m_e}\left(k_x^2 + k_y^2 + k_z^2\right). \tag{2.6}$$

The wave vectors are quantized according to $k = 2n\pi/L$, where $n$ is the principle quantum number. Due to the Pauli exclusion principle, each energy state can accommodate two electrons, one of each spin state [8].

The Fermi energy, $E_F$, is defined as the energy of the highest filled energy level in the ground state (absolute zero). For a 3D system of $N$ electrons, the Fermi energy is given by

$$E_F = \frac{\hbar^2}{2m_e}\left(\frac{3\pi^2 N}{V}\right)^{2/3}, \tag{2.7}$$

where $V$ is the system volume.

As the temperature of the system is increased, the kinetic energy of the free electrons increases, and the higher energy states begin to be occupied. The probability that an energy level is occupied in an electron gas in thermal equilibrium at temperature $T$, $f(E)$, is given by the Fermi-Dirac distribution:

$$f(E) = \frac{1}{\exp\left[\left(E-\mu\right)/k_BT\right]+1}, \tag{2.8}$$

where $\mu$ is the chemical potential. At absolute zero, $\mu = E_F$, and at all temperatures $f(\mu) = 1/2$.

### 2.1.2 Band Theory

The electronic properties of non-metals are well described by band-theory, which modifies the free electron gas model to include interactions between the electron waves and ion cores of the crystal lattice [8]. This interaction leads to bands of available electron energy states, instead of the discrete energies of free electrons. The energy bands are separated by regions of energy for which no wave-like electron orbital exists, and the magnitude of this gap is known as the band gap energy, $E_g$.

The ion cores of a crystal can be viewed as a periodic potential [8]. The solutions to the time-independent Schrödinger equation for a periodic potential are plane waves which are modulated by a periodic function with the same period as the lattice, known as Bloch functions, $U_{\mathbf{k}}(\mathbf{r})$ [8]:

$$U_{\mathbf{k}}(\mathbf{r}) = \sum_{\mathbf{G}} C_{\mathbf{k}-\mathbf{G}} e^{-i\mathbf{G}\cdot\mathbf{r}}, \tag{2.9}$$

where $\mathbf{G}$ is the reciprocal lattice vector, $C_{\mathbf{k}-\mathbf{G}}$ are periodic reciprocal space coefficients, and $r$ is the position vector. The resulting modulated plane wave, known as the Bloch wave, is:

$$\psi(\mathbf{r}) = U_{\mathbf{k}}(\mathbf{r}) e^{-\mathbf{k}\cdot\mathbf{r}}. \tag{2.10}$$

The energy bands are now periodic functions with the periodicity of the lattice: $E(\mathbf{k}) = E(\mathbf{G} + \mathbf{k})$. The conduction electrons act as plane waves in the first Brilluoin zone, and are reflected at the zone boundaries [8]. The reflected waves form standing waves which are the superposition of two states, $\psi_+$ and $\psi_-$, where the $\psi_+$ state has maximal charge density at the ion cores (lower energy), and the $\psi_-$ state has maximal charge between the ion cores (higher energy). The difference in energy between these two states relative to a free electron manifests as an energy gap, $E_g$.

The nature of the band structure of a material determines its resulting electrical properties [7]. The band structure of a metal, semiconductor, and insulator are shown schematically in Figure 2.1.

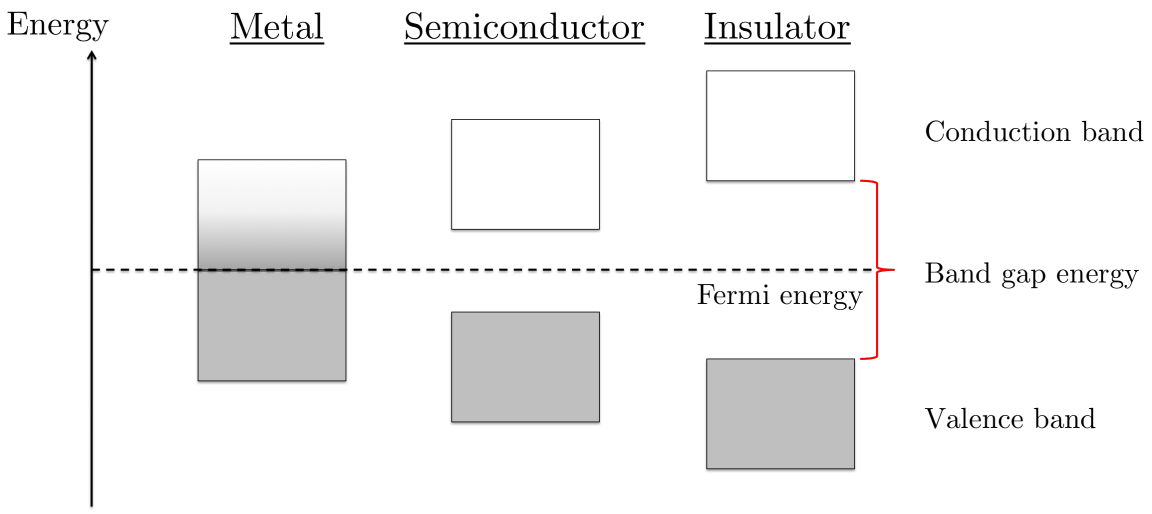


Figure 2.1: Schematic electronic band structures of different materials. Adapted from Ref. [7].

In metals there is no energy gap between the valence and conduction bands, even at absolute zero [7]. At absolute zero, insulators and semiconductors have a fully occupied band, the valence band, and an unoccupied band, the conduction band, which are separated by an energy gap. The energy gap is typically <2 eV for semiconductors and >2 eV for insulators [7]. Semi-metals, such as graphene, have a near zero band gap for certain values of electron wave vector [9].

### 2.1.3 Temperature Dependence of Electrical Conductivity

The electrical resistiviities of metallic and semiconducting materials show significantly different temperature dependences. Figure 2.2 shows the qualitative differences in $\rho(T)$ between two typical metals (Cu and Al) and a typical semiconductor (Ge) [7].

In metals, phonons (quantized lattice vibrations) can cause backscattering of electrons. Phonons will be discussed further is Section 2.3. Therefore, electrical conductivity decreases with the number of thermally activated phonons according to [8]:

$$\sigma(T) = \rho(T)^{-1} = \sigma_0 \exp\left(\frac{\hbar\omega_p}{k_B T}\right) = \sigma_0 \exp\left(\frac{T_p}{T}\right), \tag{2.11}$$

where $\hbar\omega_p$ is the energy of the backscattering phonon, and $T_p = \hbar\omega_p/k_B$.

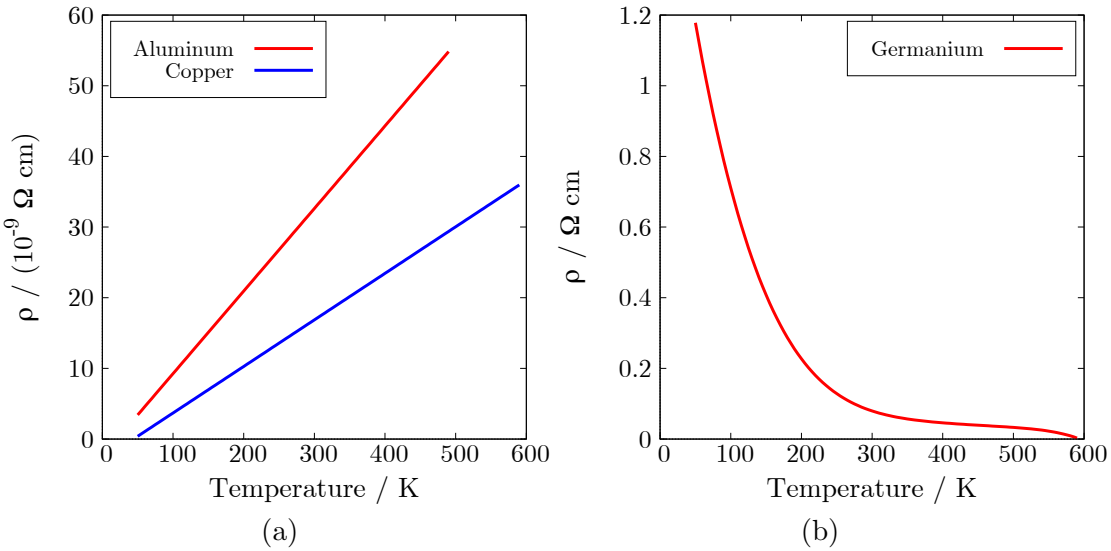


Figure 2.2: Electrical conductivity as a function of temperature for (a) typical metals, copper and aluminum and (b) a typical semiconductor, germanium. Adapted from Ref. [7].

In semiconductors, as temperature increases, the number of thermally excited electrons increases, and more electrons have sufficient energy to jump across the band gap from the valence band to the conduction band. Electron-phonon scattering is still the dominant scattering process. The temperature dependent conductivity of an intrinsic semiconductor is given by [8]:

$$\sigma(T) = \sigma_0 \exp\left(-\frac{E_g}{2k_B T}\right), \tag{2.12}$$

where $E_g$ is the band gap energy, $T$ is temperature, and $\sigma_0$ is the high temperature conductivity. At low temperatures $\sigma \to 0$ ($\rho \to \infty$) for a semiconductor.

For electrically conductive polymers and carbon nanotube materials, the temperature dependence of $\sigma$ can be described by VRH and fluctuation assisted tunneling [10]. VRH involves the tunneling of electrons between localized states assisted by the absorption of phonons. As $k_B T$ increases there are more nearby states with accessible energy levels, and thus the amount of hopping conduction increases. The VRH model predicts an exponential temperature dependence [10]:

$$\sigma(T) = \sigma_0 \exp\left[\left(-\frac{T_0}{T}\right)^{\frac{1}{1+d}}\right], \tag{2.13}$$

where $\sigma_0$ is the high-temperature limit of DC conductivity, $T_0$ is associated with thermally activated hopping between localized sites, and $d$ is the dimensionality of the conduction process ($d = 1, 2,$ or 3). Equation 2.13 shows that the dimensionality of the conduction process can be found by seeing which value of $d$ gives the best linear relationship in a plot of $\ln(\sigma(T))$ vs. $T^{-1/(1+d)}$, for $d = 1, 2,$ or 3.

In some amorphous materials there can be metallic regions separated by non-conducting regions, which can be viewed as barriers to electron conduction [10]. Fluctuations in voltage across the barrier can result in electrons tunneling across the barrier between the metallic regions. The voltage fluctuations increase with temperature, and therefore the tunneling current will also increased with temperature. If the metallic regions are large enough, it is also possible to have tunneling at low temperatures ($\sigma(0\text{ K}) \neq 0$) provided the wave functions of electrons in the metallic regions overlap. A simplified version of the fluctuation assisted tunneling model is [10]:

$$\sigma(T) = \sigma_0 \exp\left[\left(-\frac{T_b}{T_s + T}\right)\right], \tag{2.14}$$

where $T_b$ is related to the energy at which thermal voltage fluctuations become sufficient to raise the electron energy above the barrier, and $T_b/T_s$ gives the amount of tunneling in the absence of thermal fluctuations, and therefore the conductance remaining in the low temperature limit [10].

The full temperature dependence of conductive polymers and CNT materials can then be described by combining metallic conduction (Equation 2.11), variable range hopping (Equation 2.13), and fluctuation assisted tunneling (Equation 2.14) [10]:

$$\sigma(T) = \left(\underbrace{A \exp\left(\frac{T_b}{T_s + T}\right)}_{\text{tunneling}} + \underbrace{B \exp\left(\frac{T_p}{T}\right)}_{\text{phonon scattering}}\right)^{-1} + \underbrace{C \exp\left(-\left(\frac{T_0}{T}\right)^{\frac{1}{1+d}}\right)}_{\text{variable range hopping}}, \tag{2.15}$$

where $A$, $B$, and $C$ are positive constants.

A third conduction model is the weak localization model. In disordered metallic materials, the wave functions of elastically scattered electrons can interfere constructively, which decreases $\sigma$ [10]. This is especially prevalent at low temperatures. As temperature increases, inelastic scattering by phonons destroys the coherence of

the backscattered electrons, which causes non-metallic temperature dependence in $\sigma$. Weak localization is generally a small contribution to total electrical conductivity for most samples.

## 2.2 Magnetoresistance

Magnetoresistance is a measure of how a material's resistivity, $\rho$, changes (by $\Delta\rho$) in an external magnetic field, $H$. Magnetoresistance is defined as:

$$\frac{\Delta\rho}{\rho(0\,\mathrm{T})} = \frac{\rho(H) - \rho(H=0)}{\rho(H=0)} \tag{2.16}$$

where $\rho(0\,\mathrm{T})$ is the resistivity in the absence of an external field.

Several carbon allotropes, including CNTs, display negative magnetoresistance that increases in magnitude as temperature is lowered [9]. CNTs are normally diamagnetic, and, due to their small dimensions, show quantum mechanical transport effects that cannot be explained using classical magnetoresistance models, such as ordinary magnetoresistance [9]. However, magnetic fields can greatly influence the electronic band structures of CNTs. Three main phenomena influence the negative magnetoresistance observed for CNTs: Aharonov-Bohm oscillations [11]; the formation of Landau levels [12]; and weak localization [13].

The Aharonov-Bohm effect occurs when a magnetic flux passes through cylindrical conductors perpendicular to the cylinder axis, altering the relative phase of counter-propagating electron waves [11]. The phase difference alters the interference between the waves, and results in periodic oscillations in electrical resistance with changing magnetic flux. Since CNTs are hollow cylindrical conductors, they display Aharonov-Bohm oscillations for magnetic fields parallel to the tube axis, with the period of the oscillation dependent on the tube diameter. Aharonov-Bohm oscillations are typically only observed in isolated CNTs at low temperatures (<100 K) and high magnetic fields (>8 T).

When a magnetic field is applied perpendicular to the tube axis the net flux through the tube is zero. As the field intensity is increased, discrete Landau-like levels form at the Fermi energy [14]. Landau levels are quantized energy levels which occur for charged particles moving in magnetic fields as a result of the quantization of the cyclotron orbits [9]. In large magnetic fields the electron wave functions become

circumferentially localized at the top and bottom of the CNT. Since the zero-field boundary conditions were based on the quantization of the circumferentially wave functions, clearly the band structure in a magnetic field will be significantly different. As a result, CNTs that were metallic or semiconducting in zero field will become identical. These Landau levels cause an increase in the DOS at the Fermi energy with increasing applied magnetic field, and thus negative magnetoresistance. Landau levels are expected to dominate magnetoresistance at fields of 6.6 T and 26 T, 6.6 T, and 1.6 T for 10 nm, 20 nm, and 40 nm tubes, respectively [14].

The weak localization model of magnetoresistance assumes that the applied magnetic field alters the relative phases of backscattered electrons [13]. The model assumes that scattering is split into two paths, one in which electrons and holes travel in the same direction, and one in which the electrons and holes travel in opposite directions. In the latter case, the interaction between electrons and holes increases resistivity. The phase shift caused by the magnetic field can reduce the interactions between electrons and holes, thus causing negative magnetoresistance. As temperature increases, electron-phonon scattering can destroy the coherence between backscattered electrons, thus reducing the magnitude of negative magnetoresistance [10]. Scattering by chemical and magnetic impurities also decreases coherence [10]. The weak localization model predicts the temperature dependence of magnetoresistance to be proportional to $T$ and $\ln(T)$ for 1D and 2D systems, respectively, and temperature independent for 3D systems [13].

## 2.3 Thermal Conductivity

When a system is exposed to a temperature gradient, heat transport occurs to restore thermal equilibrium. In a solid, heat is transported either by lattice waves, electrons, or both [15]. Thermal conductivity, $\kappa$, describes a material's ability to conduct heat. For an isotropic material, thermal conductivity is defined by Fourier's law:

$$\mathbf{Q} = -\kappa \nabla T \tag{2.17}$$

where $\mathbf{Q}$ is the heat flux through the sample, $T$ is the sample temperature, and $\kappa$ is the scalar thermal conductivity. For anisotropic materials, thermal conductivity is

dependent on the direction of the heat flux, and is therefore a tensor quantity. Typical values of $\kappa$ at room temperature for bulk materials range from 0.2 $\mathrm{W{\cdot}m^{-1}{\cdot}K^{-1}}$ for polymers and aerogels to 2300 $\mathrm{W{\cdot}m^{-1}{\cdot}K^{-1}}$ for diamond [7].

The basic description of thermal conductivity is based on that of an ideal gas. From the kinetic theory of gases, the thermal conductivity of the gas is:

$$\kappa = \frac{1}{3} C v \lambda, \tag{2.18}$$

where $C$ is the heat capacity per unit volume, $v$ is the mean molecular speed, and $\lambda$ is the molecular mean free path between collisions [15].

Experimentally, many methods do not directly measure $\kappa$, but instead measure the thermal conductance, $K$, of the material. For a homogeneous bulk sample, $\kappa$ is defined using the thermal conductance of the sample, $K$, as well as its length, $L$, and cross-sectional area, $A$ [7]:

$$\kappa = K \frac{L}{A}. \tag{2.19}$$

For insulating solids the majority of heat is carried by quantized lattice vibrations, called phonons. The phonon contribution to $\kappa$ can be defined using Equation 2.18, with the $C$, $v$, and $\lambda$ being the *phonon* heat capacity, mean speed, and mean free path. For most insulating solids, $v$ is essentially temperature independent, whereas $C$ and $\lambda$ are generally strongly temperature dependent.

A simple crystalline material can be modelled as masses at lattice sites connected by imaginary springs. Heat causes the atoms to vibrate about their equilibrium positions. Since the atoms are connected by springs, their vibrations are coupled, which causes neighbouring atoms to form collective lattice waves. Under a temperature gradient, the atoms with more energy will have a higher vibrational amplitude, and therefore the lattice waves will propagate heat toward the less energetic atoms.

Consider a simple linear chain with two atoms per unit cell, shown in Figure 2.3, where $\beta$ is the force constant of the springs, $a$ is the length of the unit cell, and $u_s$ and $v_s$ are the displacements of the $s^{\mathrm{th}}$ atoms [8].

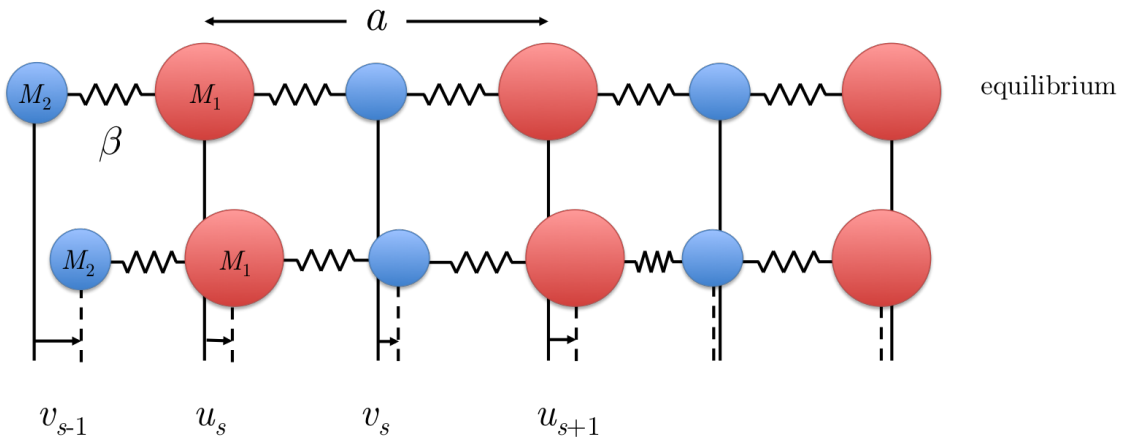


Figure 2.3: A diatomic linear chain with atoms of $M_1$ and $M_2$ with lattice spacing $a$ and force constant $\beta$, showing the equilibrium positions (top) and displaced positions (bottom). Adapted from Ref. [8].

The solutions to the atomic displacements at time $t$ are waves with angular frequency $\omega$ and wave vector $k$ [8]:

$$u_s = ue^{i(ska-\omega t)} \tag{2.20}$$

$$v_s = ve^{i(ska-\omega t)}. \tag{2.21}$$

The solution of $\omega(k)$ is called the dispersion relation, and for this simple case is given by:

$$\omega^2(k) = \beta\left(\frac{1}{M_1}+\frac{1}{M_2}\right) \pm \beta\sqrt{\left(\frac{1}{M_1}+\frac{1}{M_2}\right)^2 - \frac{4}{M_1M_2}\sin^2\left(\frac{ka}{2}\right)}. \tag{2.22}$$

The phonon dispersion relation for a simple diatomic chain is shown in Figure 2.4. The two phonon branches correspond to the optical phonons and acoustic phonons. The acoustic branch corresponds to the the coherent movement of adjacent atoms, as an acoustic wave. The frequency of acoustic phonons approaches 0 as $k \to 0$. Optical phonons involve the out-of-phase movement of neighbouring atoms in the crystal. Optical phonons remain non-zero for all values of $k$ in the first Brillouin zone. Phonon thermal energy travels at the group velocity, $v_g = d\omega/dk$. Therefore optical phonons do not contribute effectively to heat transport because they have near zero speeds ($d\omega/dk \simeq 0$) [8].

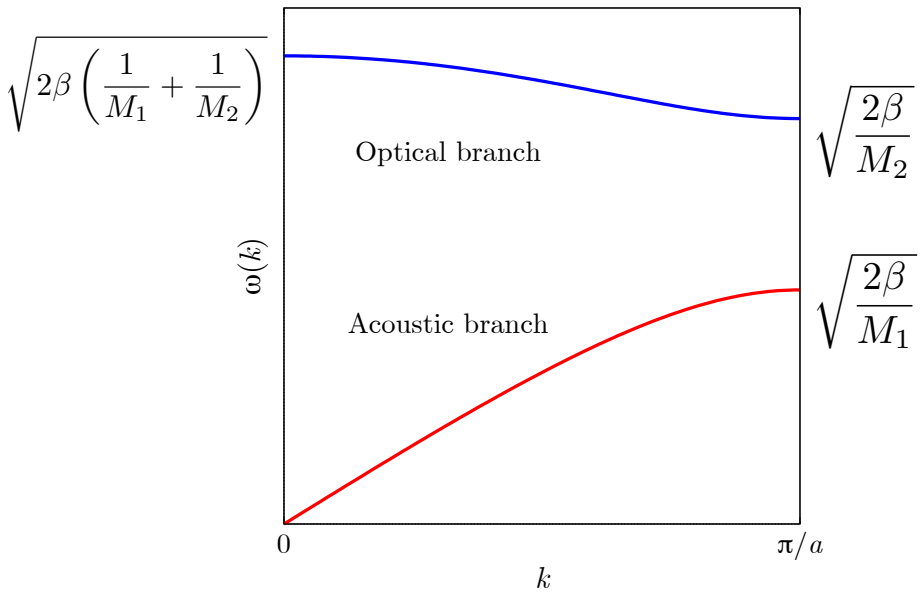


Figure 2.4: Phonon dispersion curves in the $k > 0$ half of the first Brillouin zone for a diatomic linear chain. The two branches are the optical (blue) and acoustic (red) branches [8].

The phonon mean free path of an insulating solid decreases with increasing temperature. This is because lattice vibrations in real materials are not perfectly harmonic, and phonons can be scattered by crystal boundaries, impurities, or by other phonons. Two types of phonon-phonon interactions are possible, shown in Figure 2.5. Two phonons with wave vectors $\mathbf{k_1}$ and $\mathbf{k_2}$ can interact to form a phonon with wave vector $\mathbf{k_3}$. If $\mathbf{k_3}$ is still within the first Brillouin zone, the scattering is known as the Normal process. Normal process scattering occurs at low temperature and does not affect thermal conductivity because phonon momentum is conserved [8].

The second process, known as the Umklapp process, involves the interaction of phonons at higher temperatures, in which $k_3'$ is outside of the first Brillouin zone. The $\mathbf{k_3}'$ vector is brought back into the first Brillouin zone by subtraction of the reciprocal lattice vector, $\mathbf{G}$, resulting in a vector $\mathbf{k_3}''$, as shown in Figure 2.5. The final phonon wave vector, $\mathbf{k_3}''$, is in the opposite direction of the original $\mathbf{k_1}$ and $\mathbf{k_2}$ vectors, leading to a reversal of phonon direction, and thus a reduction in thermal conductivity.

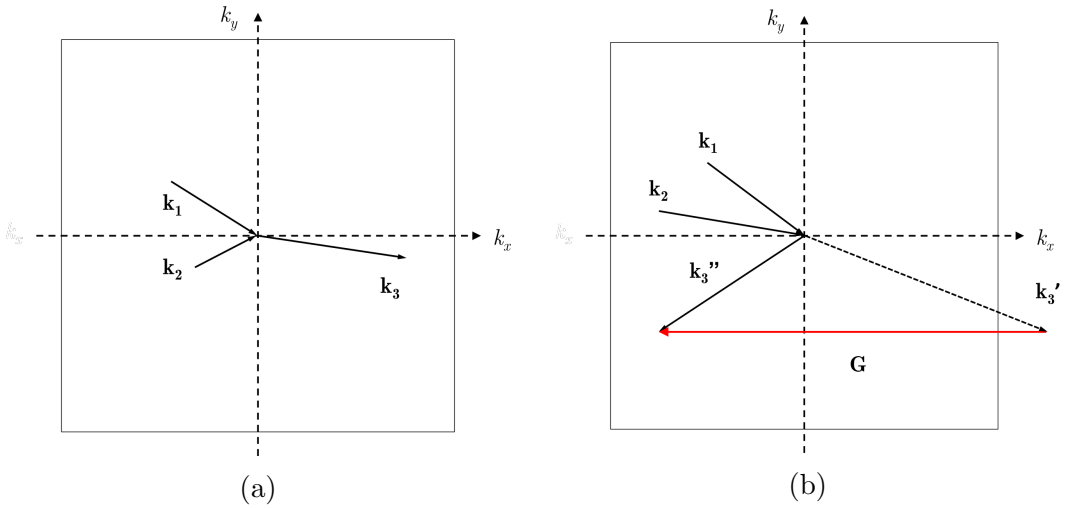


Figure 2.5: Phonon scattering diagrams demonstrating the (a) Normal and (b) Umklapp scattering processes in the first Brillouin zone. In the Normal process the resultant phonon, $\mathbf{k_3}$, travels in the same direction as the net direction of the incident phonons ($\mathbf{k_3} = \mathbf{k_1} + \mathbf{k_2}$). In the Umklapp process the resultant phonon, $\mathbf{k_3}''$, travels in a direction other than that of the incident phonons ($\mathbf{k_3}'' = \mathbf{k_1} + \mathbf{k_2} - \mathbf{G}$). Adapted from Ref. [8].

For metals, $\kappa$ is usually dominated at all temperatures by free electrons instead of phonons [7]. The electrical contribution to thermal conductivity takes a similar form to that given by the kinetic theory of gases (Equation 2.18), except with $C_e$ replacing $C$, where $C_e$ is the electronic heat capacity per unit volume, and correspondingly, $v_e$ is the electron mean thermal speed, and $\lambda_e$ is the electron mean free path [7].

In metals, electrons dominate both thermal and electrical transport, and thermal conductivity, $\kappa$, and electrical conductivity, $\sigma$, are related by the Wiedemann-Franz law:

$$\frac{\kappa}{\sigma T} = \frac{\pi^2}{3}\left(\frac{k_B}{e}\right)^2 = L_0 \tag{2.23}$$

where $L_0$ is the Lorenz number, $2.44\times10^{-8}$ W $\Omega$ K$^{-2}$ [8]. By comparing experimentally measured values of the effective Lorenz number, $L_{\text{eff}} = \kappa/\sigma T$, with the the theoretical value of $L_0$, the relative contribution of electrons versus phonons to the total heat conduction of the material. If $L_{\text{eff}} >> L_0$, thermal conductivity is dominated by phonons, not charge carriers.

# Chapter 3

# Carbon Nanotubes and Carbon Nanotube Materials

Carbon is capable of forming more allotropes than any other element because of the diversity of its possible bonding architectures. The allotropes of carbon include 0D fullerenes, 1D nanotubes, 2D graphene, and 3D diamond and graphite [9]. The physical properties of carbon allotropes are incredibly diverse, which makes carbon-based materials suitable for a wide range of applications. For example, diamond is hard, transparent, and electrically insulating, whereas graphite is soft, opaque, and electrically conductive. This chapter presents the structure and properties of the 1D carbon allotrope, carbon nanotubes, and well as the synthesis, structure, and properties of carbon nanotube yarns.

## 3.1 Carbon Nanotubes

CNTs were first characterized in 1991 by Iijima using transmission electron microscopy [16]. However CNTs were produced as far back as the seventeenth century in Damascus steel swords [17]. Since their initial identification, many amazing aspects of CNTs have been discovered, including their high tensile strength, high electrical and thermal conductivities, and many novel 1D quantum effects that are unique to CNTs [9]. These properties have made CNTs the most studied nano-material over the past several decades.

### 3.1.1 Carbon Nanotube Structure

The CNT structure is based on graphene, a monolayer of hexagonally bonded carbon atoms. A SWCNT can be viewed as a single sheet of graphene rolled to form a hollow cylinder, and capped with half fullerenes [9]. SWCNTs typically have diameters of $\sim$2 nm, and lengths up to mm, meaning the aspect ratio can be as high as $10^6$, making them quasi-1D nanostructures. Multiple concentric nanotubes, known as MWCNTs can also be formed, with typical diameters of 10 to 20 nm [9].

The physical properties of SWCNTs depend largely on the tube diameter and the angle at which the graphene sheet is rolled, known as the chirality. The tube can be rolled in any arbitrary direction, with the only distortion to the hexagonal lattice coming from the curvature of the CNT. The chirality is described by the chiral vector, $\mathbf{C}_h$, shown in Figure 3.1, which runs perpendicular to the tube axis [9]:

$$\mathbf{C}_h = m\vec{a}_1 + n\vec{a}_2 \tag{3.1}$$

where $\vec{a}_1$ and $\vec{a}_2$ are the unit vectors of the single layer graphene hexagonal lattice ($|\vec{a}| \approx 2.46$ Å), and $n$ and $m$ are integers, known as the chiral indices. The three possible CNT cross sections are "armchair" ($n = m$), "zig-zag" ($m = 0$), and chiral (all other $n$ and $m$), as shown in Figure 3.1.

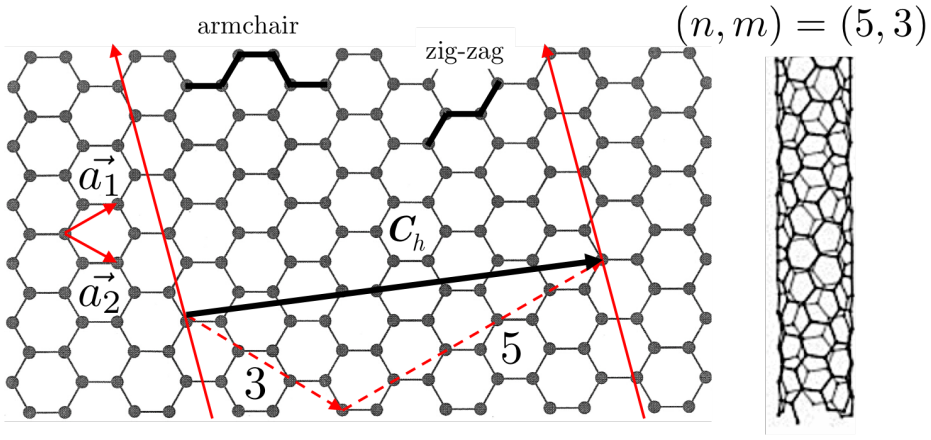


Figure 3.1: The hexagonal graphene structure including the chiral vector (bold black arrow) of a $(n, m) = (5,3)$ SWCNT, and the resulting tube structure. Adapted from Ref. [18].

The diameter of the CNT can easily be found from the chiral vector, $|C_h|$, which is equal to the tube circumference:

$$d = \frac{|\mathbf{C}_h|}{\pi} = \frac{a}{\pi}\sqrt{n^2 + m^2 + nm}. \tag{3.2}$$

### 3.1.2 Properties of Carbon Nanotubes

#### 3.1.2.1 Electrical Properties

The electronic properties of CNTs can be estimated using the electric structure of graphene. The 2s, $2p_x$, and $2p_y$ orbitals of each carbon atom in the graphene lattice

hybridize to form three $sp^2$ orbitals (covalent $\sigma$ bonds) in the plane of the graphene sheet [9]. The remaining $p_z$ orbital is perpendicular to the graphene plane and forms $\pi$ bonds. The energy levels of the $\pi$ orbitals are near the Fermi energy, and therefore the $\pi$ orbitals form delocalized states which allow for electrical transport.

Figure 3.2 (a) shows the energy dispersion diagram of graphene near the Fermi energy in the first Brillouin zone [19]. Graphene is a semimetal in which the valence and conduction bands touch at six Dirac points (K and K') within the Brillouin zone.

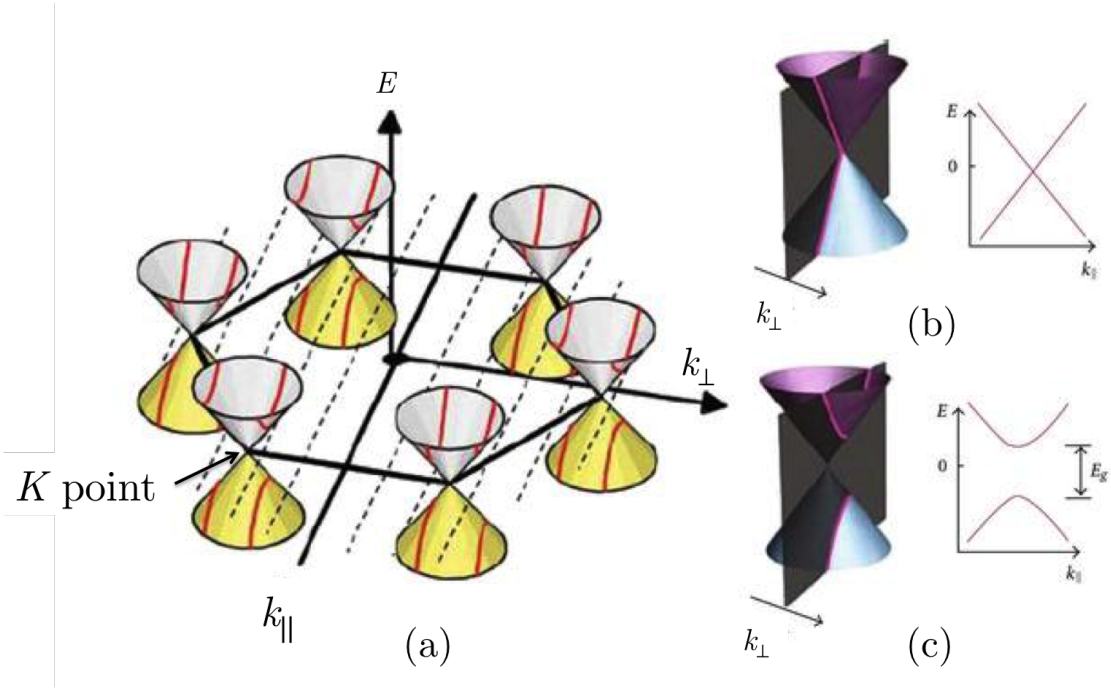


Figure 3.2: (a) 3D schematic of the electron energy dispersion relations of graphene near the Fermi energy, shown in the first Brillouin zone. The dashed lines indicate the allowed values of $k_\perp$ for a CNT, and the red lines indicate the corresponding 1D dispersion relations. (b) Metallic band structure of a CNT. (c) Semiconducting band structure of a CNT. Reprinted with permission from Ref. [19].

The band structures of CNTs can be calculated from that of graphene by imposing a periodic boundary condition for the wave function of electrons moving along the tube axis (the zone-folding scheme) [9]. By rolling graphene into a tube, the wave vectors perpendicular to the tube axis, $k_\perp$, become quantized according to $k_\perp \cdot C_h = 2\pi m$, where $C_h$ is the chiral vector and $m$ is an integer. By quantizing $k_\perp$, the 1D band structure of a SWCNT is generated by taking a cross-sectional slice of the 2D graphene band structure, as shown in Figure 3.2. The $(n, m)$ values from Equation

3.1 determine where the 1D CNT sub-band passes through first Brillouin zone of graphene, and therefore the electrical properties of SWCNTs are strongly dependent on chirality and tube diameter. If the allowed $k_\perp$ states pass through the K or K' points (Figure 3.2 (b)), the CNT will be a zero band gap metal. However, if the $k_\perp$ states do not pass through any of the K or K' points (Figure 3.2 (c)) the CNT will be semiconducting, with the band gap energy depending on the value of $(n, m)$. On average, 1/3 of nanotubes are metallic and 2/3 are semiconducting [9].

In MWCNT, there is also the possibility to have inter-tube conductance, perpendicular to the tube axis. In graphite, interlayer conductance is quite small, but does exist because of the overlap of $\pi$ bands between layers. In MWCNTs, the curvature reduces the amount of overlap, and thus it is expected that MWCNTs should have very small electrical conductance between tubes.

Negative magnetoresistance is observed in individual CNTs and CNT materials. Negative magnetoresistance on the order of -15% at 2 K and 9 T has been reported previously for CNT sheets [5] and yarns [6]. The negative magnetoresistance of CNT materials is typically explained using the Bright model and weak localization model.

#### 3.1.2.2 Thermal Properties

The thermal conductivity of SWCNTs has been reported to be one of the highest measured values of any known material: individual nanotubes have been measured to have thermal conductivities greater than that of diamond, with room temperature conductivities of 3500 $\mathrm{W{\cdot}m^{-1}{\cdot}K^{-1}}$ [2], and molecular dynamics simulations have predicted $\kappa$ values of up to 6600 $\mathrm{W{\cdot}m^{-1}{\cdot}K^{-1}}$ [20]. Individual CNTs have extremely high thermal conductivities because of their high purity and stiffness, leading to long phonon mean free paths [20].

The thermal conductivity and heat capacity of CNTs are dominated by phononic modes, even in metallic CNTs and at low temperatures [21]. The phonon dispersion relation for a SWCNT consists of four acoustic modes (one longitudinal, two transverse, and one "twist" mode), and many optical modes [22]. The twist mode is caused by torsion of the tube about its long axis.

At low temperatures, the thermal conductivity of CNTs is ballistic ($\lambda_{ph}$ longer than the CNT length) and thermal conductivity increases linearly with temperature

($\kappa \sim T$). The ballistic regime becomes less dominant with increasing temperature as phonon-phonon, phonon-boundary, and phonon-defect scattering become more prevalent. For example, ballistic transport is predicted to exist up to 100 K for a 10 $\mu$m long (10,10) SWCNT [23].

In the diffusive regime, the different forms of phonon scattering all contribute to the overall thermal conductivity in CNTs [24]. The room temperature $\lambda_{ph}$ is estimated to range from 50 nm to 1.5 $\mu$m in pristine SWCNTs, and as low as 4 nm is defective CNTs. As temperature increases, more phonon modes become active, and both heat capacity, $C$, and $\kappa$ increase ($\kappa \sim C \sim T^{\alpha}, \alpha \sim 2$). Thermal conductivity then peaks near $T = 300$ K as the excitation of high frequency phonon modes is offset by the increased phonon scattering rate. Above 300 K, phonon-phonon scattering begins to dominate, and $\kappa$ decreases continuously as $\kappa \sim T^{-1}$ [2].

In MWCNTs, inter-shell forces mean that $\kappa$ is no longer purely one-dimensional. MWCNTs are likely better for heat conduction applications because their larger diameter allows for more phonon modes [25]. Also, the affect of intrinsic defects on the thermal conductivity of MWCNTs is decreased relative to SWCNTs because adjacent walls give alternate pathways for phonons to bypass defects and vacancies.

Defects in CNTs, including flaws in the tube wall or impurities, can significantly reduce $\kappa$ even at low defect concentration. Defects strongly suppress high-frequency phonon modes, and have been shown in simulations to reduce $\kappa$ in SWCNTs up to three fold at defect concentrations of only 0.25% [26]. In MWCNTs it is also likely the wall defects increase inter-wall phonon scattering, further reducing $\kappa$ [27]. Therefore, reduction of defects and impurities during production, or by post-treatment techniques, is vital to optimize the thermal conductivity of CNTs.

### 3.1.3 Synthesis

Historically the most significant road-block in the research and development of CNTs has been their low production rate and high cost. Increased industrialization of CNT production in the past decade has dropped the price of MWCNTs from ∼$1000/g in the early 2000s to ∼$100/kg presently [28]. However, the high price of quality CNTs with well characterized properties, such as SWCNTs sorted by chirality ($1500/g) or MWCNT arrays ($1500/cm$^2$) (wwww.sigmaaldrich.com), limits the practicality of CNTs for many potential applications.

The fundamental requirements for the synthesis of CNTs are heat, a carbon precursor, and a catalyst. The two main categories of CNT synthesis are substrate-based, such as CVD, or substrate-free methods, including arc discharge, and laser ablation [28]. CNTs produced by these various methods have different structures, properties, bulk morphologies, and yields. Substrate-free synthesis methods produce the largest quantity of CNTs. However their low quality often means they are only suitable as composite additives, not for thermal or electrical applications [29]. Also, production rates for arc-discharge and laser ablation are on the order of 10s of g/day, whereas CVD methods can produce 10s of kg/day [30]. Chemical vapour deposition is the most relevant technique for this work, and will be discussed in more detail below.

#### 3.1.3.1 Chemical Vapour Deposition (CVD)

Chemical vapour deposition involves the thermal decomposition of a carbon-containing precursor gas (*e.g.* hydrocarbons, $CO_2$, or alcohols) on a catalyst substrate. The catalyst is most commonly a Si wafer with a $SiO_2$ layer (100s of nm), sputtered with transition metal NPs, such as Fe, Mo, Co, Cu, and Cr [28]. Synthesis takes place in a tube furnace at temperatures between 700 °C and 1100 °C.

At these temperatures the NPs are liquid, allowing for the precursor gas to be decomposed and dissolved into the NP. When the carbon in the NP reaches saturation, it will begin to precipitate out, forming a self-assembled CNT. The number of walls and the diameters of CVD grown CNTs can be controlled by adjusting the NP size and reaction temperature [31].

CVD-grown CNT arrays have heights of 100s of $\mu$m up to several cm, and this is the only method currently capable of growing such long CNTs [31]. The mass density of these arrays is on the order of $\sim$ 0.06 g cm$^{-3}$ [4], with CNT growth densities of $\sim 10^{10}$ cm$^{-2}$ [31].

CNTs cluster into groups of 100s of CNTs because of the van der Waals forces between adjacent tubes. Defects in CVD grown CNTs are generally amorphous carbon resulting from the relatively low synthesis temperature, or metallic impurities from the catalyst [29]. However, post-growth annealing of CVD grown CNTs can be used to improve crystallinity and remove impurities and amorphous carbon. The physical properties of CVD-grown CNT arrays are discussed in Section 3.2.1.

## 3.2 Carbon Nanotube Materials

The objective of creating bulk assemblies of CNTs is to exploit the properties of CNTs on a useable macroscopic scale. The downside is that the strength and conductivities of these bulk materials are often several orders of magnitude lower than individual CNTs because of weak CNT contacts, inter-tube thermal/electrical resistances, low density, bulk defects, and impurities [28]. The structure and properties of CNT arrays and yarns are discussed below.

### 3.2.1 Arrays

CNT arrays are the base for dry-spun CNT sheets and yarns, and also directly show promise for specific applications, such as thermal interface materials for heat management in high density electronics [28]. Thermal conductivities of CVD grown CNT arrays with heights up to 6 mm were measured by Jakubinek *et al.* [6]. Room temperature thermal and electrical conductivities in the growth direction were $\sim$ 1 W$\cdot$m$^{-1}\cdot$K$^{-1}$ and $\sim$10 S$\cdot$cm$^{-1}$, respectively. These low conductivities were because of the low density of the arrays (0.06 g/cm$^3$).

CNT arrays also serve as the basis for other CNT material architectures, including CNT sheets and yarns. This is because continuous, low-density, horizontally aligned CNT webs can be pulled from vertically aligned CNT arrays, a phenomenon first discovered by Jiang *et al.* [32]. The ability of an array to form a continuous web is known as its "drawability", and depends strongly on the morphology of the CNTs

in the array. The drawability of CNT arrays is key to forming other CNT materials, such as sheets and yarns.

During CVD growth of CNT arrays, parameters such as temperature, gas partial pressures, and growth time, can all be controlled. However, only a subset of the resulting arrays will actually be "drawable". All known drawable MWCNT arrays have been produced using thermal CVD, with heights of 300 to 1000 $\mu$m and CNT diameters of 10 to 20 nm [31]. Several array properties are believed to significantly affect drawability including: CNT height; catalyst size distribution; CNT surface structure; and, likely most importantly, the formation of CNT bundles and entanglement within the array [33].

Vertically aligned CNTs form bundles of up to 100s to CNTs because of the strong van der Waals forces between adjacent tubes. Entanglement within the array then occurs when individual CNTs migrate from one bundle to another, as shown in Figure 3.3. Kuznetsov *et al.* developed a model for how CNTs are drawn from arrays based on the density of these CNT cross-linkage throughout the array [34].

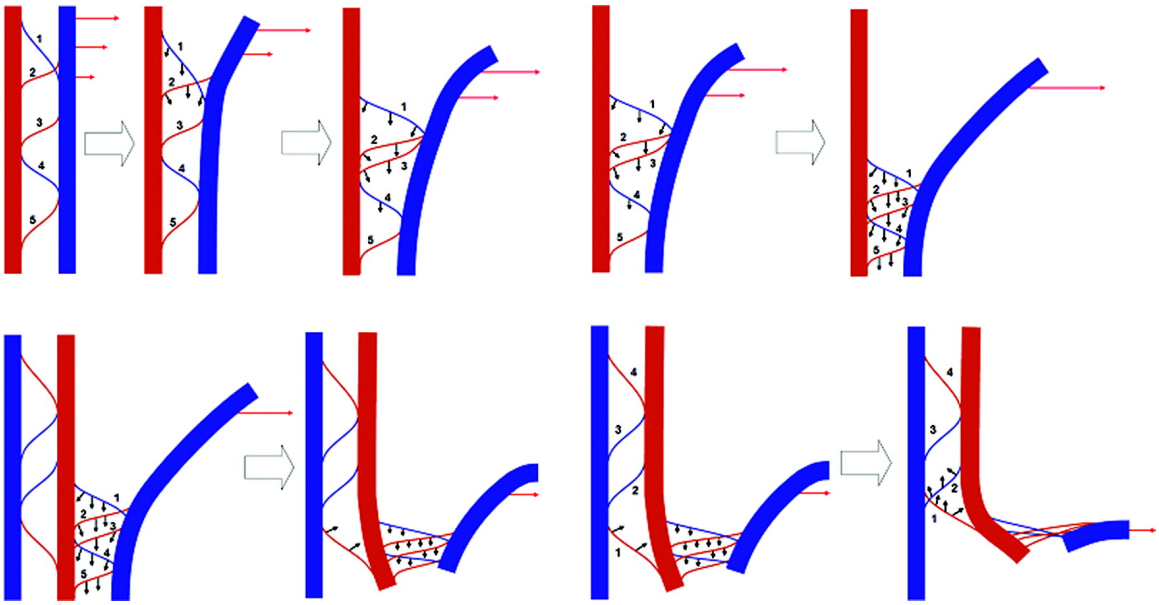

Figure 3.3: Schematic view of how bundles of CNTs are drawn from a vertically aligned array. The bundles are held together by van der Waals forces and CNT entanglements between bundles. As bundles are pulled from the array, entanglements become concentrated at the top and bottom of the array, allowing successive bundles to be drawn from the array. Reprinted from Ref. [34]. Used with permission from the American Chemical Society.

In the Kuznetsov *et al.* model, CNT bundles are pulled from the array because of the "unzipping" of the interconnections between bundles [35]. Figure 3.3 shows neighbouring CNT bundles (thick lines) and individual CNT interconnects (thin lines). In the first frame, two CNT bundles with several interconnects are shown. The blue bundle is pulled from the top to the right. As the pulling continues, the interconnects "unzip", concentrating the interconnects at the bottom of the two bundles. When the density of interconnects reaches a critical value, the pulling force will be sufficient to begin removing the second (red) bundle. As pulling continues, the process of unzipping interconnects repeats between the red bundle and second blue bundle, this time from bottom to top.

### 3.2.2 Yarns

It is possible to create small diameter (<100 $\mu$m) yarns made from CNTs. The yarn structure is extremely useful for many applications, because the quasi-1D structure allows for the linear transmission of tensile load, heat, and electricity, and also because they can be woven and shaped into more complex structures. The most significant advantage of CNT yarns over other bulk CNT materials, such as composites and buckypapers, is the combination of higher density and alignment, which greatly improves transport properties [28].

#### 3.2.2.1 CNT Yarn Production

There are two main methods for CNT yarn production: liquid-state spinning and solid-state spinning. In liquid-state spinning, introduced in 2000 by Vigolo *et al.* [36], CNTs are dispersed into a fluid and extruded or coagulation spun into continuous fibres, much like Kevlar® and other industrial fibres [37, 38]. In wet spinning the CNT synthesis and yarn processing are decoupled, which allows each property to be optimized individually. However, liquid-spun yarns are usually heavily doped with the dispersant, and require post-treatment to improve physical properties.

In solid-state spinning the yarns are produced without any chemical dispersants or additives. The first type of solid-state spinning involves pulling CNTs directly from the furnace chamber, known as reactor spinning, and is often done with floating catalyst CVD [39, 40]. Reactor spinning is efficient but produces short CNTs with

high impurity content from the catalyst particles, often resulting in poor transport properties of the as-produced yarns [28].

Current dry-spinning methods, including the one used in this work, use motors to simultaneously pull and spin the CNT web from the array, forming a continuous yarn and allowing semi-automated yarn production and collection [6, 41]. Recent advances to CNT yarn spinning have allowed spinning rates of 16 m/s [42]. A detailed explanation of the yarn spinning process used in this work is given in Section 4.1.2.

A major drawback of dry spinning from arrays is the difficulty in scaling up to an industrial level, since arrays are currently limited to ∼20 cm diameters. Also, dry spinning combines multiple steps into one, which makes it difficult to isolate and optimize properties. Dry-spun yarns are generally low density, with many structural and chemical impurities. However, dry-spun yarns have had promising physical properties to date because of the length of the CNTs (up to 1 mm), which decreases the number of CNT junctions and increases strength and conductivities [28].

#### 3.2.2.2 CNT Yarn Structure

An untwisted bundle of CNTs has a fraction of the strength of the constituent individual CNTs, because the CNTs in the bundle interact very weakly. Twisting the bundle causes radial compression, which increases the interaction between CNTs. Twisting causes the CNTs to migrate repeatedly between the interior and exterior of the yarn structure. This migration causes the ends of the CNT bundles to be trapped within the yarn structure, greatly improving the tensile strength, and preventing the yarn from unwinding. Individual CNTs in yarns can have several hundreds of contacts with other CNTs over their length [43].

The degree to which a yarn is twisted has a large affect on the mechanical and transport properties of the resulting yarn. The degree of twisting is often reported as the residual twist, $\tau$, which is the twist remaining after the yarn structure is allowed to relax to a stable configuration after spinning, defined using the yarn surface twist angle, $\theta$, and diameter, $d$ [44]:

$$\tau = \frac{\tan(\theta)}{\pi d}, \tag{3.3}$$

given in units of $\mathrm{m}^{-1}$ ($\equiv$ turns$\cdot\mathrm{m}^{-1}$). The surface twist angle is shown in Figure 3.4.

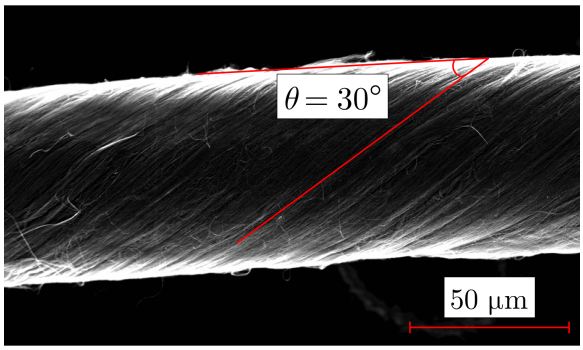


Figure 3.4: SEM micrograph of a pristine 60 $\mu$m diameter CNT yarn showing a surface twist angle of 30°.

Sears *et al.* used FIB milling and SEM to study CNT yarn structure as a function of twist angle, as shown in Figure 3.5 [44].

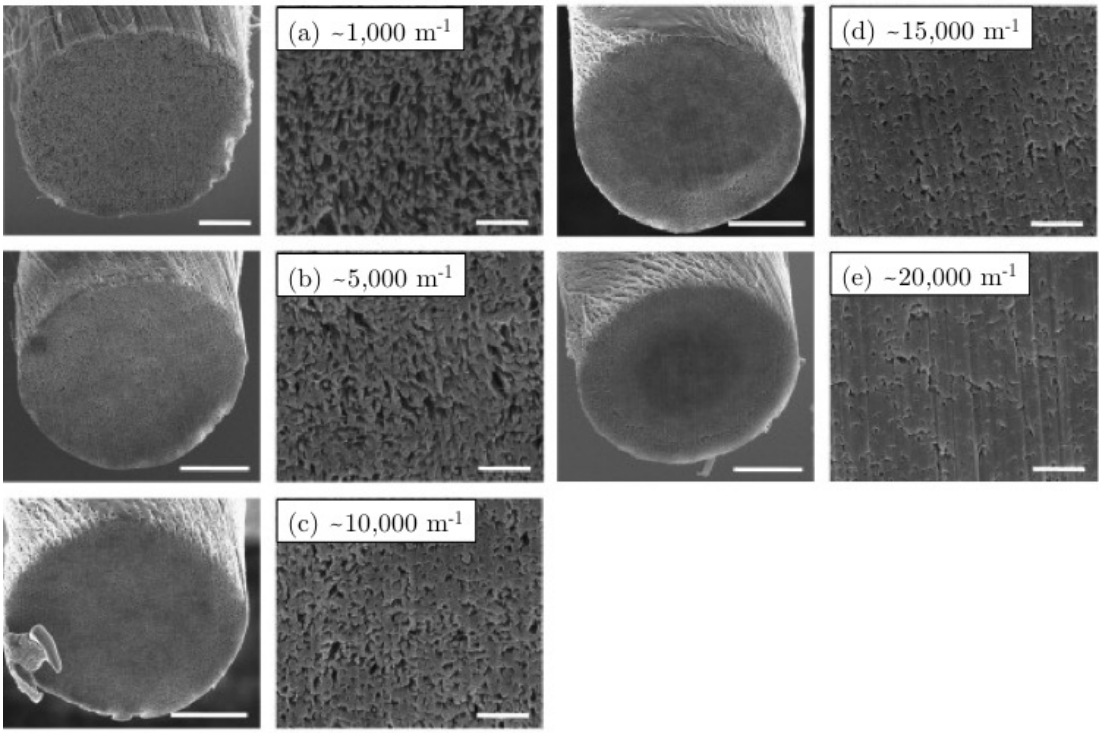


Figure 3.5: SEM micrographs showing the cross sections of CNT yarns as a function of residual twist, as indicated in units of turns·m$^{-1}$. The scale bars represent 5 $\mu$m. Reprinted with permission from Ref. [44].

It was found that yarns with residual twists below ~1000 m$^{-1}$ had an irregular cross section and highly porous structure. As twist was increased to ~ 6000 m$^{-1}$

the structure became more circular and homogeneous, and the packing density was observed to increase monotonically with twist density, as seen in Figure 3.5 (b) and (c). As the yarns were twisted above 16000 $m^{-1}$ (Figure 3.5 (d) and (e)) a "core-sheath" structure is formed, in which a high-density core is surrounded by a low-density sheath. This structure is likely formed because the higher pressure at the centre of the yarn increases the interaction between the CNT bundles, thus increasing density. When the yarn is torque stabilized after spinning, the loose outer bundles are able to relax more than those at the centre, and the"core-sheath" structure is formed.

### 3.2.3 Thermal Conductivity

The focus of most research on CNT yarns has generally been on mechanical and electrical properties, with few reports concerning thermal conductivity measurements. In comparison to other carbon materials, CNT yarns, as with other bulk CNT materials, have significantly lower room temperature thermal conductivities. Table 3.1 shows the room-temperature thermal conductivities of a variety of carbon allotropes, including CNT materials.

Table 3.1: Room-temperature thermal conductivities of carbon allotropes.

| CNT yarn Sample | $\kappa_{app}$ (300 K) / $W{\cdot}m^{-1}{\cdot}K^{-1}$ | Ref. |
|---|---|---|
| Graphene | 4840 | [7] |
| Diamond | 2310 | [7] |
| SWCNT | 3400 | [2] |
| MWCNT | 600 | [25] |
| MWCNT array | 0.5 - 1.2 | [4] |
| MWCNT sheet | 2.54 ± 0.48 | [5] |
| MWCNT yarn | 60 ± 20 | [6] |

The definition of $\kappa$ given by Equation 2.19 assumes the composition and external dimensions of the material are homogeneous [28]. For heterogenous materials, such as composites, $\kappa$ can clearly vary significantly within the cross section. Experimental measurements of composite materials therefore give a value of $\kappa$ that is the average over the components of the composite, called the apparent thermal conductivity, $\kappa_{app}$.

CNT yarns can be viewed as low density CNT/air composites (CNT/vacuum composites during measurements) [45]. By defining $A$ in Equation 2.19 for CNT yarns as the outer yarn diameter, the apparent conductivity of the CNT/vacuum composite is given: $\kappa_{app}$ can be viewed as the value of $\kappa$ for a homogeneous material with equivalent physical dimensions. Because the porosity of bulk CNT materials is high, the actual cross section through which heat can flow is significantly smaller than the physical cross-sectional area. Attempts can be made to correct for this low density, such as normalizing measured values to the theoretical density of an individual CNT. However, the apparent thermal conductivity is the value that is relevant to applications, and is therefore how the results of this thesis are presented.

In addition to low density, the thermal conductivity of CNT materials is reduced because when CNTs are bundled together the rotational and vibrational freedom of the individual CNTs becomes suppressed. Aliev *et al.* observed a four fold reduction in the thermal conductivity of a 120 SWCNT bundle relative to an individual SWCNT [25]. This considerable reduction was associated with the quenching of phonon modes and high thermal resistance at tube-tube junctions.

Tube-tube interactions between pristine CNTs are dominated by van der Waals forces. This van der Waals force acts over short distances ($U \propto -1/r^{-6}$), essentially vanishing for CNTs separated by more than 4 Å [46]. Because of this weak interaction, heat flow between overlapping CNTs is very low. In addition, the cylindrical shape of CNTs results in a very small overlapping surface area. However, in CNT materials the length of CNT-CNT overlapping is significantly larger than the CNT diameter. Aliev *et al.* calculated that the ideal overlap length to minimize the thermal resistance between two parallel 10 nm CNTs is $\sim 30$ $\mu$m [25].

CNT yarns are likely the ideal structure for a highly thermally conductive bulk CNT material. Twisting means that their density is higher than spun CNT sheets, and they also greatly reduce the surface area, which reduces radiative loses, which can be very large at room temperature for MWCNT sheets [25]. The high alignment of CNTs in the yarn structure also improves $\kappa$ relative to unaligned samples. Hone *et al.* used vacuum filtration in a 25 T magnetic field to create magnetically aligned SWCNT films [47], and measured a $\sim$7.5 times increase in $\kappa$ for the aligned film relative to an unaligned film [21].

### 3.2.4 Electrical Conductivity

As with thermal conductivity, the electrical conductivity of CNT yarns is significantly lower than that of individual CNTs [6]. However, CNT yarns have sufficient electrical conductivity and tolerance to high-current density, along with low density, to make them promising for some applications, such as microelectrodes for mechanical implants, strong wires for microelectronics, or cables for aerospace applications [28]. This is increasingly promising as the supply and price of copper continues to rise. The potential application with the most impact would be using CNT thread for electrical wiring [48]. Conventional metal cables have many downsides, including: weight; poor mechanical strength (sagging power-lines); the skin effect (limiting use in telecommunications); and increasing price (and decreasing supply) or metals such as copper. All-carbon CNT wiring could reduce costs while improving performance.

The electrical conductivity of CNT yarns is several orders of magnitude below that of individual CNTs because of the presence of impurities and defects, which cause electron scattering and contact resistance. CNT yarns typically have room temperature electrical conductivities on the order of $10^2$ S·cm$^{-1}$, and show semiconducting temperature dependence.

#### 3.2.4.1 Influence of Adsorbed Oxygen and Water Vapour

Adsorbed atmospheric species have been shown to influence the electrical conductivity of CNTs and CNT materials [49, 50]. Electrical conduction in MWCNTs in mostly through the outer wall, and on the outer wall every atom is a surface atom. Therefore any adsorbed species will have a large influence on the electrical properties. Changes in humidity have also been shown to cause a 50 to 60% increase in CNT yarn weight, which is an important consideration for potential applications [51].

Several mechanisms have been suggested to explain the influence of oxygen and water vapour on the electrical properties of CNTs. It is generally accepted that adsorbed oxygen molecules cause p-doping and an increase in electrical conductivity however, the influence of water vapour is less clear. Simulations have given conflicting results, but generally suggest that water molecules alone have a small affect on the electrical conductivity of CNTs.

Lekawa-Raus *et al.* studied the affect of atmosphere exposure on the electrical properties of CNT fibres [52]. CNT yarns and films were produced by CVD, and the electrical resistance was measured for up to 85 days of exposure to ambient conditions. Exposure to these conditions resulted in a decrease in electrical resistance between 9 and 21 %. This change in resistance would be substantial in an application such as a high-power cable, and therefore the adsorbed gas dependence of CNT materials must be well understood.

When the CNT fibres were heated from 300 K to 800 K in vacuum ($< 10^{-6}$ Torr), three distinct local minima in resistance were observed, as shown in Figure 3.6 [52]. The first two valleys, at 300 K and 440 K, were attributed to the removal of adsorbed oxygen and $H_2O$. At the second valley $R$ increased by $\sim 50\%$ relative to the initial value. The third valley, near 630 K, was taken to be the removal of absorbed hydrocarbons and possibly other impurities. All of these valleys were absent after cooling to 300 K. The total increase in resistance was 100% [52].

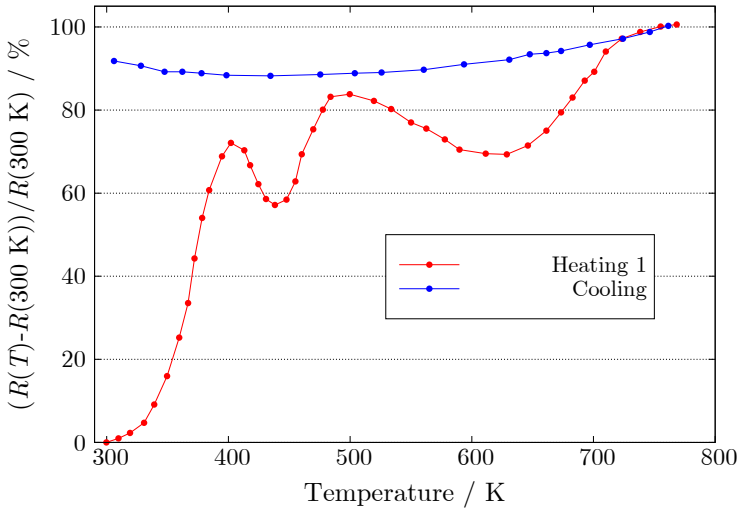


Figure 3.6: Hysteresis in $R(T)$ for a CNT fibre after degassing in vacuum ($10^{-6}$ Torr) to $T = 750$ K. Data from Ref. [52].

Upon subsequent exposure to atmosphere for 4 months, and reentry into vacuum, the resistance remained nearly 30% higher than the pristine yarn [52]. Also, the 300 K and 440 K valleys associated with water were still observed, but their influence was less pronounced. The 640 K valley, however, was not present, suggesting that the effect of high-temperature on the yarn was permanent [52].

To distinguish between the influence of oxygen and $H_2O$, the yarns were exposed to either dry air or 80% relative-humidity air using a vacuum gas cell. Resistance was measured during exposure to the different gases, and is shown in Figure 3.7. The results indicate that exposure to dry $O_2$ (at $t = 4$ hours in Figure 3.7 (a)) had little influence on the yarn's resistance. However, exposure to wet air (at $t = 7$ hours) in Figure 3.7 (b) caused a significant decrease in resistance[52].

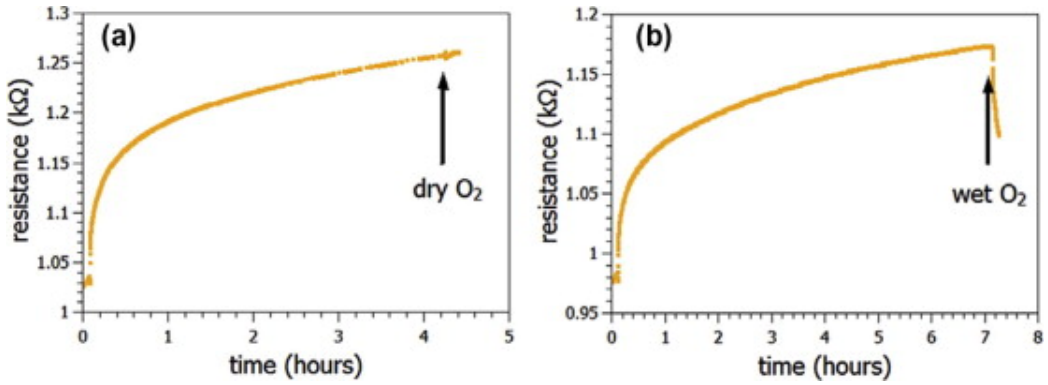


Figure 3.7: Electrical conductivity of a CNT yarn showing the influence of exposure to (a) dry oxygen and (b) oxygen and water vapour. Reprinted from Ref. [52] with permission from Elsevier.

Raman spectroscopy was carried out to study the possible mechanism for the decreased resistance in the presence of water. Upon p-doping the fibres with acid, a 10 $cm^{-1}$ blue shift in the G-peak resulted [52]. Yarns that were exposed to $H_2O$ showed no change in G-peak position, indicating that p-doping is not the dominant influence. This suggests that there is little charge transfer between the water and CNTs, as has been demonstrated in simulation [52]. The most likely explanation is that the water causes a decrease in the junction resistance between CNT, which has been shown with acid doping [53].

The influence of vacuum on electrical conductivity of the CNT yarns studied in this work is discussed in Section 5.3.

## 3.3 Raman Spectroscopy of CNT Materials

When a photon interacts with matter, there is a small probability that the photon with be scattered by the electron cloud of an atom, causing a short-lived perturbation of the electron cloud caused by the oscillating electric field of the incident photon.

Atomic vibrations (phonons) can also perturb the electron clouds of the atoms in a material. It is therefore possible for photons and phonons to interact, leading to inelastic scattering, known as the Raman effect [54].

Raman spectroscopy is a technique used to measure the inelastic scattering of monochromatic laser light by excitations in a material, usually phonons [54]. The light interacts with the material through the polarizability of the valence electrons, and can cause either emission (Stokes process) or absorption (anti-Stokes process) of phonons with energy $h\nu$, where $\nu$ is the phonon frequency. By measuring the change in energy of the scattered light relative to the incident light, the frequency of the corresponding phonon can be calculated. A typical Raman spectrum consists of scattered phonon intensity plotted versus Raman shift, $\Delta\tilde{\nu} = \lambda_0^{-1} - \lambda_1^{-1}$, in units of wavenumber. Each peak corresponds to a phonon mode, and therefore Raman spectroscopy can be used to classify the vibrations in a material.

Raman spectroscopy is commonly used to assess the quality of $sp^2$ carbon materials, including CNTs [22, 55]. Raman spectroscopy is convenient because of its ease of use and because of the presence of several distinct vibrational modes for $sp^2$ carbon. Figure 3.8 shows example Raman spectra of graphene, carbon nanotubes, and other $sp^2$ carbon materials [55]. The most significant vibrational modes for $sp^2$ carbon materials are the D-band ($\sim 1350$ cm$^{-1}$) and G-band ($\sim 1582$ cm$^{-1}$) [55].

In highly crystalline single-layer graphene, shown in red in Figure 3.8, the only observed peaks are the first-order (one phonon) G-band ("graphitic"-band) and the second-order (two phonon) G'-band. The G-band corresponds to a vibrational mode caused by the in-plane breathing of the carbon atoms in the hexagonal rings. In pristine $sp^2$ carbon materials, only the G- and G'-bands would be active [55].

The presence of symmetry-breaking disorder in $sp^2$ carbon materials activates several vibrational modes, including the D-band, D'-band, and combination D+G mode, as shown in Figure 3.8 for damaged graphene. The D-band a double-resonance band caused by the breathing of carbon hexagons that become Raman active at the borders of crystalline areas due to the loss of translational symmetry. Therefore the D-band is often associated with defective carbon materials, since it would not be present in a perfectly crystalline material. Much like the D mode, the D' mode at $\sim 1620$ cm$^{-1}$ is a double-resonance mode associated with disorder and defects [55].

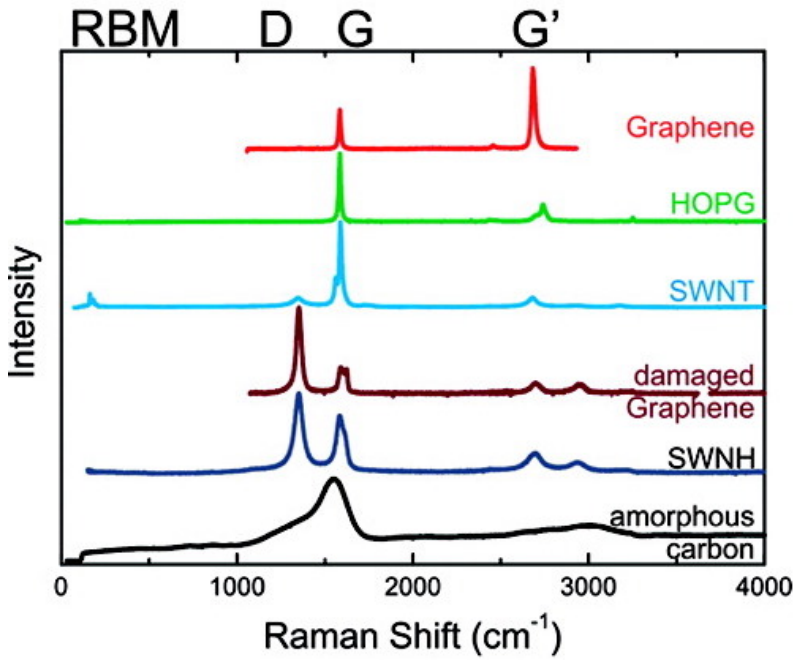


Figure 3.8: Raman spectra (Stokes process only) for several $sp^2$ carbon materials: highly crystalline mono-layer graphene; highly ordered pyrolytic graphite (HOPG); SWCNT; damaged graphene; single walled nanohorns (SWNH); and amorphous carbon. Reprinted with permission from M.S. Dresselhaus *et al.*, Nano Letters 10, pp. 953-973, 2010 [55]. Copyright (2010) by American Chemical Society.

The ratio of the intensities of the D-band and G-band peaks is therefore an qualitative measure of the the graphitic quality (crystallinity) of a CNT based material. Raman spectroscopy can therefore be used to track the changes in crystallinity after post-treatment, including annealing. It is important to note that the intensity ratio, $I_G/I_D$, is dependent on the laser wavelength and power used, and in general cannot be compared directly for data taken from different Raman spectrometers [5, 56].

In SWCNTs, there is another mode, the RBM ($\sim 200$ cm$^{-1}$), in which the carbon atoms move simultaneously in the radial direction. This mode is unique to CNTs and is thus one of the most frequently used methods for confirming the presence of CNTs in a sample. Also, the Raman shift of the RBM strongly depends on the CNT diameter, and can therefore be used to assess of diameter of the CNTs. In MWCNTs the RBM is usual suppressed by adjacent tubes.

## 3.4 Post-Processing of CNT Materials

The outstanding physical properties of CNTs, including high electrical and thermal conductivities, do not directly translate to as-prepared bulk CNT materials because of weak tube-tube contacts, low density, and defects in the CNTs or bulk structure. This is especially true for CVD grown CNT materials because of the low reaction temperature [57]. Therefore efforts must be made to optimize the properties of the bulk material using post-processing techniques. The most commonly used post-processing techniques are: mechanical or solvent densification [58, 59]; doping [60]; and high-temperature annealing [61]. Chemical treatments, such as acid treatment, remove catalytic particles, but can cause severe damage to the tube walls [57]. The influence of high-temperature annealing on CNT materials is discussed in more detail below.

### 3.4.1 Annealing

High-temperature annealing in inert atmosphere is a non-chemical method to remove metal catalyst particles from the nanotubes, crystallize amorphous carbon, and also improve the crystallinity of the CNT walls. Since the degree of CNT wall crystallinity and defect density are closely related to the transport properties of CNT materials, high-temperature annealing is a suitable method for optimizing the transport properties of CNT materials.

High-temperature annealing improves the crystallinity of carbon materials in a stepwise manner. For example, the two most important temperature regimes for crystallization of amorphous carbon to graphite are the carbonization temperature ($\sim$650 °C to 750 °C) and the graphitization temperature ($\sim$ 2300 °C) [9]. Between the carbonization and graphitization temperatures (at ambient pressure) carbon can break and reconnect $sp^2$ covalent bonds to form the graphite planar structure (ABAB stacking) from amorphous carbon [9]. C-H, C-O, and C-N bonds are broken to form $H_2O$, CO, $CO_2$, and $CH_x$ during carbonization [9]. At slightly higher temperatures C-C bonds are formed from the resulting dangling carbon bonds. Above the graphitization temperature the individual graphite planes become more linear and uniformly spaced [55].

Figure 3.9 shows a summary of the improvement of CNT crystallinity with annealing temperature. As discussed in Section 3.3, Raman is the most common method to compare the crystallinity of CNTs. There is no significant improvement to the Raman $I_G/I_D$ ratio below annealing temperatures of 1500 °C, and then a rapid increase in $I_G/I_D$ above 2000 °C [14, 62, 63, 64, 65].

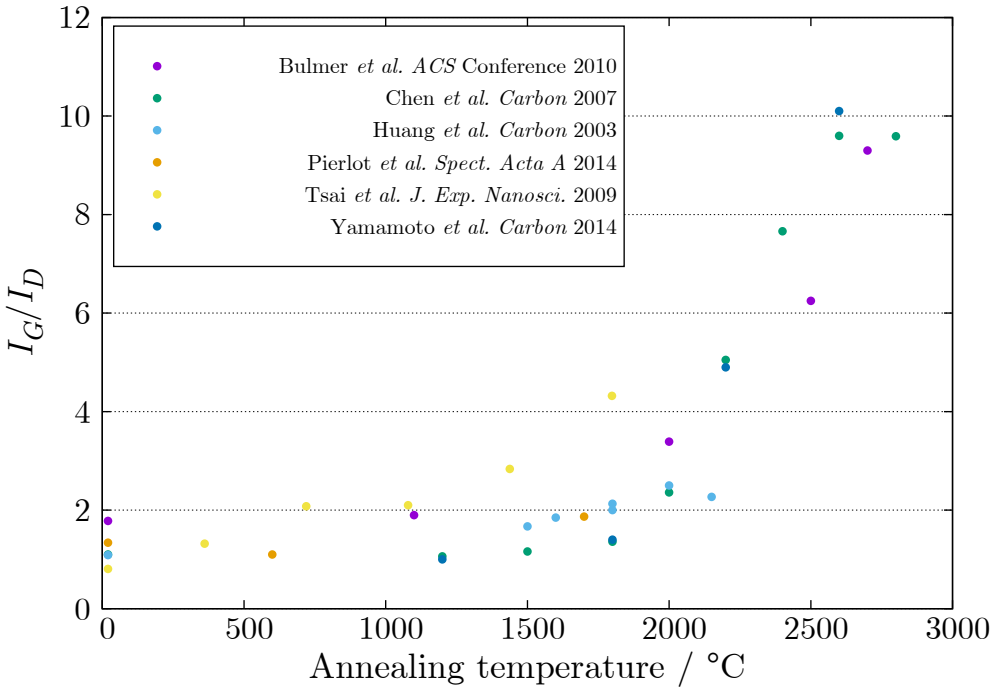


Figure 3.9: Improvement to the Raman $I_G/I_D$ with annealing temperature for various CNT materials, with data from Refs. [14, 62, 63, 64, 65].

The suggested mechanism for the improvement in crystallinity is based on transmission electron microscope (TEM) images, such as Figure 3.10, of CNTs after annealing at different temperatures. The graphitization is observed to occur in a step-wise manner, as with the crystallization of graphite [9]. The pristine CNT consists of few-layer thick turbostratic graphene (Figure 3.10 (a)), which remains after annealing to 1200 °C. After annealing to 1800 °C and 2200 °C (Figure 3.11 (b) and (c)) the domains become joined and form a continuous wavy wall structure. As temperature is increased to 2600 °C, the stacking faults in the CNT walls are fixed, and the resulting tube walls (Figure 3.10, (d)) are aligned and uniformly spaced, although some larger defects remain.

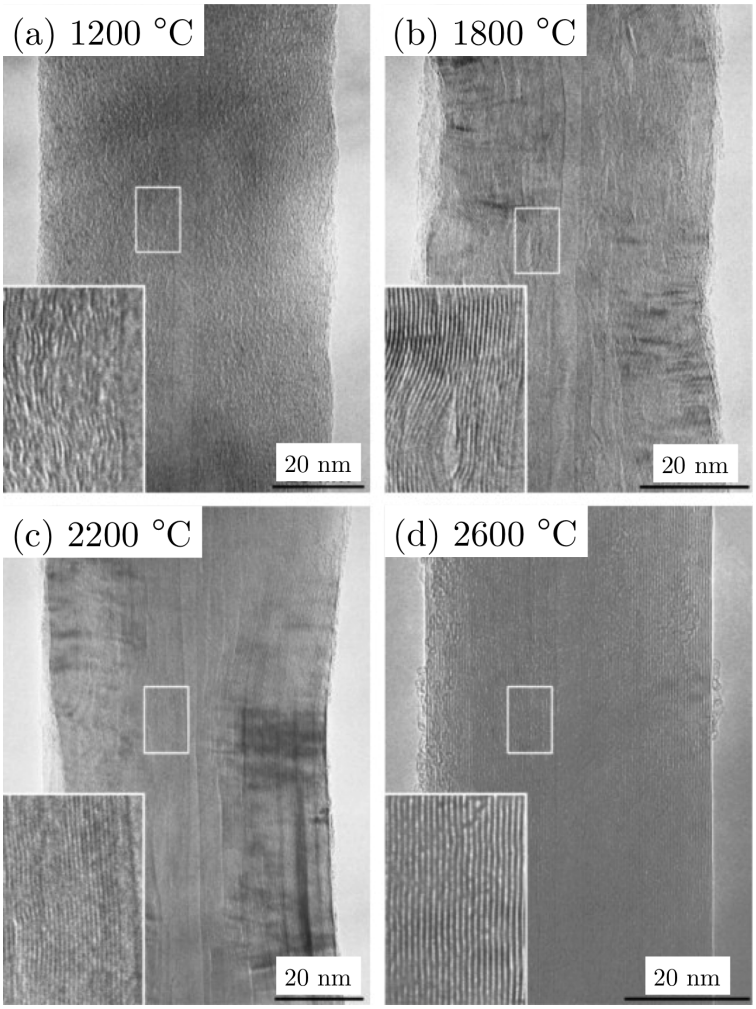


Figure 3.10: TEM images showing improvements in MWCNT wall crystallinity after annealing at: (a) 1200 °C (b) 1800 °C (c) 2200 °C (d) 2600 °C. Adapted from [65]. Used with permission from Elsevier.

CNT materials grown by CVD typically use transition metal catalysts, and metal impurities are often found at the CNT tips and between adjacent walls in MWCNTs. The low temperatures used in CVD are insufficient to vaporize the metal catalyst impurities in CVD grown CNT materials [66]. Annealing has also been shown to completely remove metal particles, even those that are within CNTs. [14, 67]. Figure 3.11 shows the residual Fe and S content, measured using X-ray fluorescence analysis, in CVD grown CNTs after annealing in Ar atmosphere between 1250 °C and 2800 °C [14]. There is an abrupt removal of the catalyst particles above ∼2000 °C.

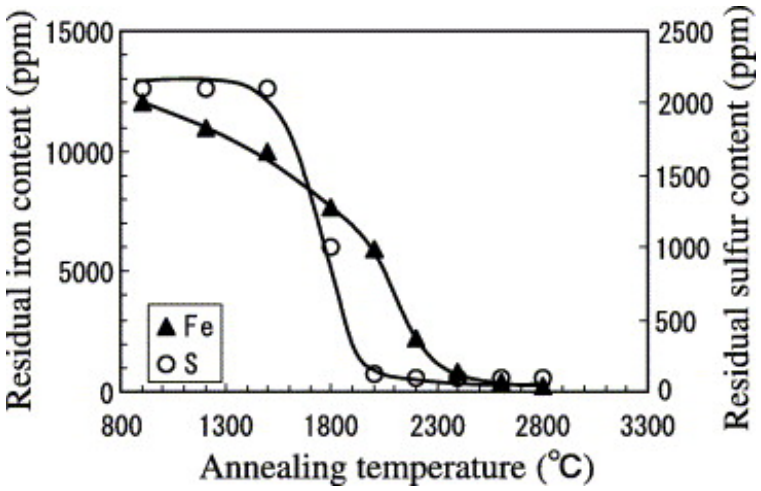


Figure 3.11: Change in Fe and S content in MWCNTs after high-temperature annealing measured by X-ray fluorescence analysis. Reprinted from Ref. [14] with permission from Elsevier.

The process of the catalytic particles defusing through the CNT walls likely causes internal stress on the walls of the nanotubes because of the change in density of the catalyst as it is vapourized [14]. This stress is likely relieved after annealing at temperatures above ∼2000 °C. Also, many reports have suggested that removing metal catalyst particles greatly reduces the toxicity of CNTs [68].

High-temperature annealing of CVD grown CNT materials in Ar atmosphere has generally been shown to increase electrical conductivity [57, 61, 69]. For example, Mattia *et al.* measured a monotonic increase in $\sigma$ with annealing temperature for CNT films, with a ∼20 fold increase after annealing at 2000 °C [69]. Annealing has also been observed to increase the semiconducting temperature dependence of electrical conductivity of CNT bundles [61].

The influence of high-temperature annealing of CNT material on thermal conductivity has not been studied in detail previously. For example, annealing a wet-spun CNT yarn at 600 °C doubled $\kappa$ because of the removal of acid impurities [60]. Mayhew *et al.* found annealing to 2800 °C for 20 hours improved the thermal conductivity of carbon nanofibers from 4.5 $\mathrm{W{\cdot}m^{-1}{\cdot}K^{-1}}$ to 160 $\mathrm{W{\cdot}m^{-1}{\cdot}K^{-1}}$ [70]. Jin *et al.* measured a 9 times increase in $\kappa$(300 K) for bundles of MWCNTs [61]. However, the precise influence of high-temperature annealing on the thermal conductivity of CNT materials is still unclear because of the lack of truly systematic investigations.

# Chapter 4

# Experimental Techniques

## 4.1 CNT Yarn Production

The carbon nanotube arrays and dry-spun CNT yarns used in this work were produced by the author at the Nanoworld Laboratories at the University Cincinnati in August 2013. These yarns were produced to study how high-temperature annealing affects the yarn's thermal and electrical properties. The Nanoworld Laboratories group is known for producing high quality, drawable, CNT arrays, and also for developing the first semi-automated dry-spinning CNT yarn production methods [41]. These spinnable arrays have been used previously to create CNT sheets [5] and yarns [6].

### 4.1.1 CNT Array Growth

The catalyst substrate for CVD was prepared by physical vapour deposition (PVD) using a Kurt J. Lesker PVD 75 (base pressure of $1.9 \times 10^{-3}$ Torr). The catalytic thin film of Fe and Co, totalling $\sim$1.2 nm, was deposited onto a Si wafer substrate (10 cm diameter) with a 5 nm $Al_2O_3$ buffer layer. During PVD, the wafer was spun at $\sim$17 rpm during sputtering to ensure even coverage of the substrate.

The circular wafer was scribed into 3 cm long sections with widths of 10 mm (Array 1), 15 mm (Array 2), and 20 mm (Array 3). The width of the array substrate is used to approximately control the resulting diameter of the CNT yarn, given a constant twist angle [42]. The scrap pieces of substrate (the rounded sides) were loaded into the CVD chamber to test the growth conditions. Since the width of the rounded corner pieces changes, they were not suitable for spinning, and could thus be sacrificed.

CVD growth of CNT arrays was done using a First Nano EasyTube® 3000 chamber. The chamber has a 12.7 cm quartz reactor, four mass flow controlled gas lines, and a maximum temperature of 1100 °C [71]. The chamber also has a load lock,

which reduced contamination and increased the repeatability of the CNT growth. The CVD growth process was completely computer controlled, which allowed for the repeatable production of drawable CNT arrays.

The CVD growth was done using ethylene as the carbon-containing precursor gas. Growth took place at 750 °C at 740 Torr chamber pressure. When the reactor reached 750 °C, 300 standard cubic centimeters per minute (sccm) of $C_2H_4$ and 1000 sccm of argon were added to the chamber for 20 minutes. When growth was completed, the arrays were cooled rapidly using 30 sccm of $H_2O$ and 2000 sccm of Ar to promote detachment from the substrate, which greatly assists the ease of yarn spinning. Detaching the array from the substrate could also allow the substrate to be reused for subsequent CVD growth, which could assist with the scale-up of CVD growth methods [42]. The entire CVD process took place in approximately two hours, and the resulting arrays were $\sim$ 300 $\mu$m in height. An example of a small section of an array is shown in Figure 4.1.

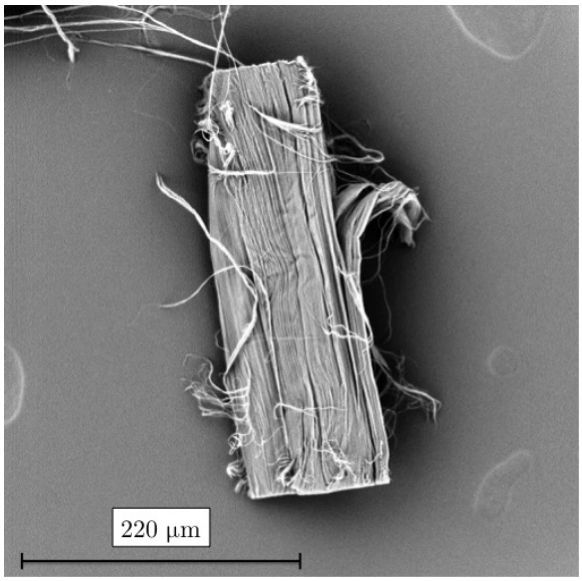


Figure 4.1: SEM micrograph of a section of CVD grown CNT array with a height of 300 $\mu$m. Several bundles of CNTs can be seen, which are vital to the drawability of the array. The CVD growth direction is from bottom to top in the image shown.

When the drawability of the arrays was confirmed, the scribed substrate sections were loaded into the reactor, and the growth process was repeated. Due to the small chamber size, only two arrays were grown at a time to avoid uneven gas distribution

in the chamber. However, because the growth conditions are automatically controlled by the chamber, multiple growths produce extremely similar arrays.

The CNTs produced by this technique typically have diameters of 10 to 15 nm, spacing of 70 to 100 nm, and areal densities of $\sim 10^{10}$ CNT·cm$^{-2}$ [31]. The bundling of CNTs within the array often means that the density of the array is slightly inhomogeneous. This can affect the diameter uniformity of the resulting yarns.

### 4.1.2 CNT Yarn Spinning

As mentioned in section 3.2.2.1, when CNTs are pulled from a "drawable" array, they can form a continuous web perpendicular to the CNT growth direction. This web can then be spun as it is pulled to produce a continuous CNT yarn, which can be collected on a thread bobbin.

Figure 4.2 shows a top view schematic of the CNT yarn spinning assembly used to create the CNT yarns for this project. The array was held on an adjustable stand so that the pulling direction was kept near horizontal. The main components of the setup are two motors, the "spinning" and "pulling" motors, which were attached to the collection bobbin. Both motors were controlled by small power supplies, which allowed for the independent adjustment of the twisting and pulling rates. The pulling motor drew the CNT web toward to collection bobbin, while the spinning motor rotated the entire pulling motor/bobbin section about the pulling direction.

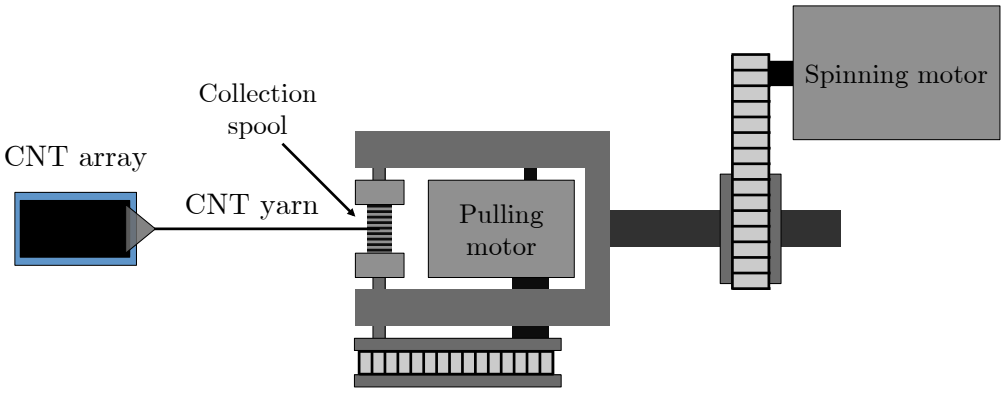


Figure 4.2: Top view schematic of the CNT thread spinning method used to produce continuous CNT yarns from CNT arrays.

At the beginning of the spinning process, a CNT web was formed by pulling at the edge of the CNT array using tweezers. This web was hand spun to form the initial thread structure. The thread was then wrapped around the bobbin, and the motors were turned on at a slow speed. As the thread began to be collected from the array, the motors were ramped up to full speed, and then left at a constant value. For each yarn the spinning rate was 900 rpm and the pulling rate was on the order of $mm \cdot s^{-1}$. On average, each mm of array produces 1 m of yarn, meaning that each array produced roughly 30 m of yarn.

As the spinning process continued, the thread was collected on the bobbin. Care was taken to ensure that the yarn was evenly spread over the bobbin, and did not accumulate in one location. Figure 4.3 shows an image of a CNT array as it was being spun into a thread.

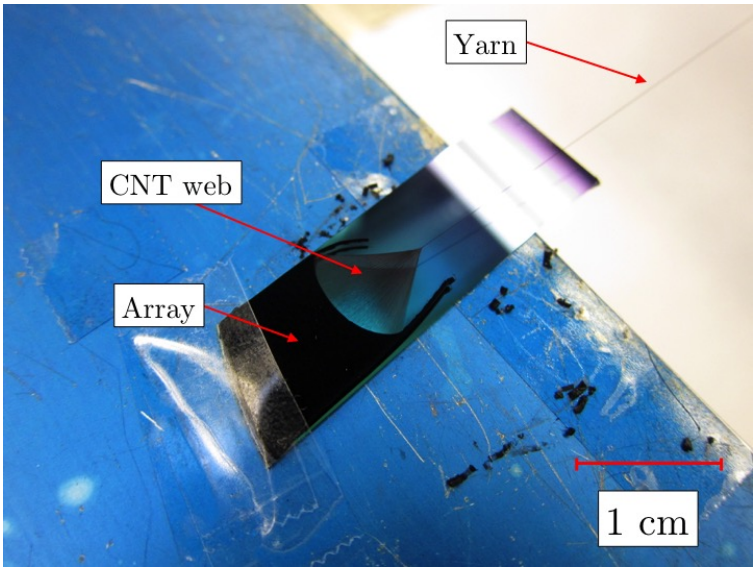


Figure 4.3: A CNT array being dry-spun, with the pulling direction to the upper right corner. The array, web, and yarn are labelled.

A small amount of the array (<1 mm) on each side was not removed during the spinning process. These sections were periodically removed by hand when they came close to interfering with the spinning process. Spinning was done until the array was completely consumed, and took approximately two hours per array.

## 4.2 Annealing

High-temperature thermal annealing of the CNT yarns was performed by the author at the Nanoworld Laboratories using a Materials Research Furnaces Inc. furnace with an Allen Bradley 1000P gas system. The furnace used a graphite heating element, graphite insulation, and was water cooled. Before annealing, the furnace was flushed by cycling between Ar atmosphere (760 Torr) and vacuum (0.1 Torr) to remove as much oxygen as possible. However, there were likely trace contaminants, including oxygen, from the gas lines.

The yarns were wound around a 2 cm diameter graphite rod, which was placed inside of the furnace. Because of their porous structure, CNT yarns are extremely sensitive to any sort of compressive force, so excessive handling was avoided, and tweezers were used only on the ends of the yarns. Several meter long sections of each yarn were annealed at two different temperatures, 2300 °C and 2700 °C, for 2.5 hours. As a result, each of the three arrays have three differently prepared yarns: pristine, 2300 °C annealed; and 2700 °C annealed. This allows for the affect of annealing on the thermal and electrical properties of the yarns to be isolated, since each of the yarns were processed using the same CVD and spinning conditions.

The samples were exposed to atmosphere after annealing and stored in sealed plastic containers. Oxygen and water vapour can be adsorbed onto the surface of CNT materials, and can affect the electrical properties [49, 72]. The affect of adsorbed species on the electrical properties of these CNT yarns is discussed in Section 5.3.1.

## 4.3 Characterization

Each differently prepared yarn was characterized using scanning electron microscopy (SEM) and Raman spectroscopy. SEM micrographs were taken to assess the structure and quality of the yarns before and after annealing, and also to measure the diameters and twist angles of the yarns for conductivity calculations.

Two SEMs were used in this work: a Hitachi S4700 cold field SEM for high quality images, and a Phenom G2 Pro desktop SEM for rapid diameter measurements. The yarns were sufficiently electrical conductive so that no gold sputtering was required to remove static charge. The CNT yarns were mounted on double-sided carbon tape

on a pin stub, and for both SEMs a 5 kV acceleration voltage was used. Example SEM micrographs for the differently prepared yarns are shown in Chapter 5.

Raman spectroscopy was used to assess the relative quality of the CNT yarns before and after annealing, as discussed in Section 3.3. The Raman spectra were collected at the Nanoworld Laboratories by the author using a Renishaw inVia Raman microscope equipped with a 514 nm Ar ion laser. The small spot size of this Raman microscope makes it possible to record spectra for these thin yarns. Spectra were collected from 100 $cm^{-1}$ to 3200 $cm^{-1}$.

A 2 cm long section of each yarn was mounted in the Raman microscope on a glass microscope slide. The laser was first aligned in the middle of the yarn using a 50× magnification optical microscope. Multiple spectra were collected at different points along the length of each yarn to get average values of $I_G/I_D$, since the small spot size makes the spectra very sensitive to any local defects.

## 4.4 Physical Properties Measurement System

The Physical Properties Measurement System (PPMS) by Quantum Design (San Diego, CA), is a versatile system used to measure the thermal and electrical properties of materials, including heat capacity, thermal conductivity, and electrical conductivity. The PPMS can measure physical properties from 2 to 400 K under vacuum ($< 10^{-4}$ Torr) and magnetic fields up to 9 T. A cross section of the PPMS chamber is shown in Figure 4.4.

The PPMS consists of a 2.5 cm diameter sample probe within a cryogenic vacuum chamber. The sample is placed at the bottom of the sample chamber, on top of heaters and a thermometers, which control and monitor the sample temperature. The chamber is cooled by liquid helium, and surrounded by a vacuum jacket and thermal insulation. The vacuum within the sample chamber can be adjusted from 3 Torr to $10^{-4}$ Torr. The outer layer of the PPMS is a 9 T superconducting magnet cooled by liquid helium.

The PPMS makes use of various sample platforms, known as "pucks", for different measurement types. The pucks use 12-pin electrical contacts which allow to easy sample insertion and removal. The two pucks used in this work to measure thermal and electrical conductivity are discussed in detail below.

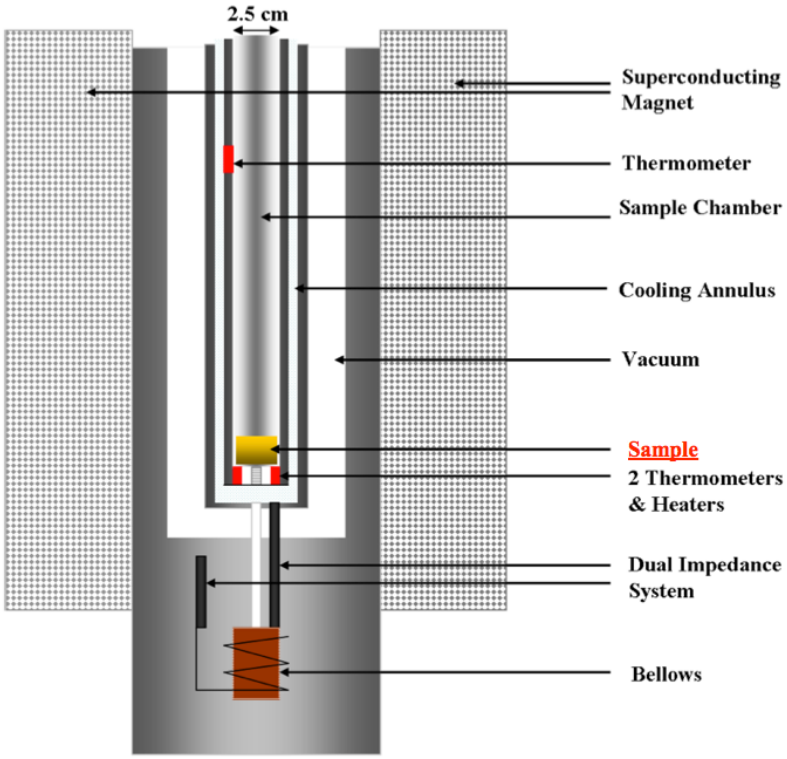


Figure 4.4: Cross section of Physical Properties Measurement System chamber. From Ref. [73], used with permission from the author.

### 4.4.1 Parallel Thermal Conductance Method

Traditional steady-state thermal conductivity methods are based on Equation 2.17. Heat is applied to one end of the sample, and the resulting 1D temperature gradient, $\mathrm{d}T/\mathrm{d}x$, is measured using thermocouples that are attached to the sample. These methods require rigid samples that can support the heater and thermocouples. Many materials, including most bulk CNT materials, are either too thin or too flexible to use the traditional steady-state method, and other techniques must be used.

The parallel thermal conductance (PTC) method can be used for fragile samples based on its success in measuring the thermal conductivity of thin film samples [74]. This method has been used previously to measure the thermal conductivity of CNTs yarn [6] and CNT sheets [5]. The accuracy of the PTC method is often better than 10% [15].

The PTC method is a modified steady-state measurement in which the sample is supported between two brass posts, and the background and radiation thermal

conductances are accurately measured and subtracted. The PTC sample stage used in this work is shown schematically in Figure 4.5(a). One post has a 120 Ω strain gauge heater attached to it, and is connected to the base using cellulose acetate to minimize heat conduction. The second post is heat-sinked to the base using a brass strip in order to maximize heat conduction. The temperature difference between the two posts, $\Delta T$, was measured using a differential thermocouple. The samples were attached to each stand using silver paint (DuPont 4929 N). For CNT yarns, up to 15 pieces were attached to maximize the thermal conductance. Measurements were performed under high vacuum ($< 10^{-4}$ Torr), and a copper radiation shield was used to reduce heat exchange with the surroundings.

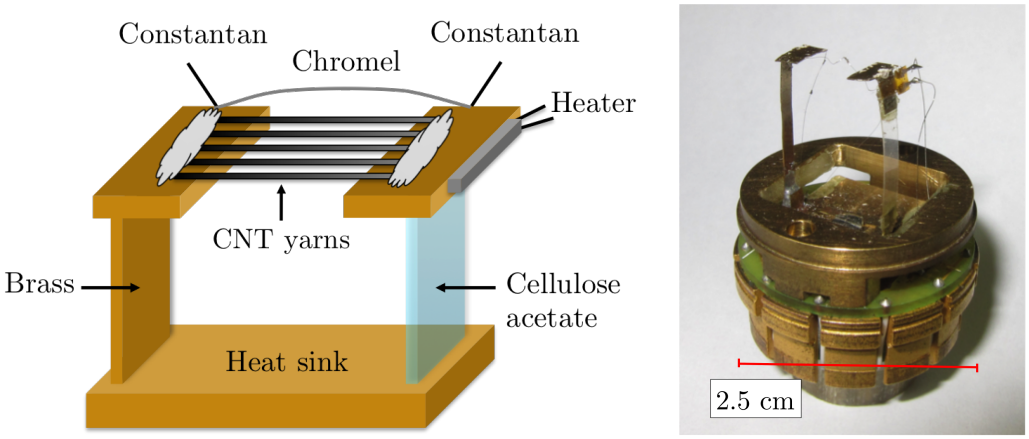


Figure 4.5: (a) Schematic and (b) image of the parallel thermal conductance method sample platform.

The thermal conductance of the system, $K$, can be measured by applying power, $P$, to the heater, and measuring the corresponding $\Delta T$. At each sample temperature four values of $\Delta T$ were measured. The initial steady-state $\Delta T$ was measured with $P = 0$. The power was then adjusted to give steady-state $\Delta T$ values of 1, 2, and 3% of the cryostat temperature. The value of $K$ was then given by $P = K\Delta T$. The thermal stability condition was defined as fluctuations less than 0.01 K. Data were typically collected for 10 minutes at each value of $\Delta T$ once stability was reached. A plot of $P$ and $T$ versus time at 300 K for the typical background measurement is shown in

Figure 4.6. At 300 K, each run took approximately 1 hour (after thermal equilibrium was reached), whereas runs typically took two hours at 50 K.

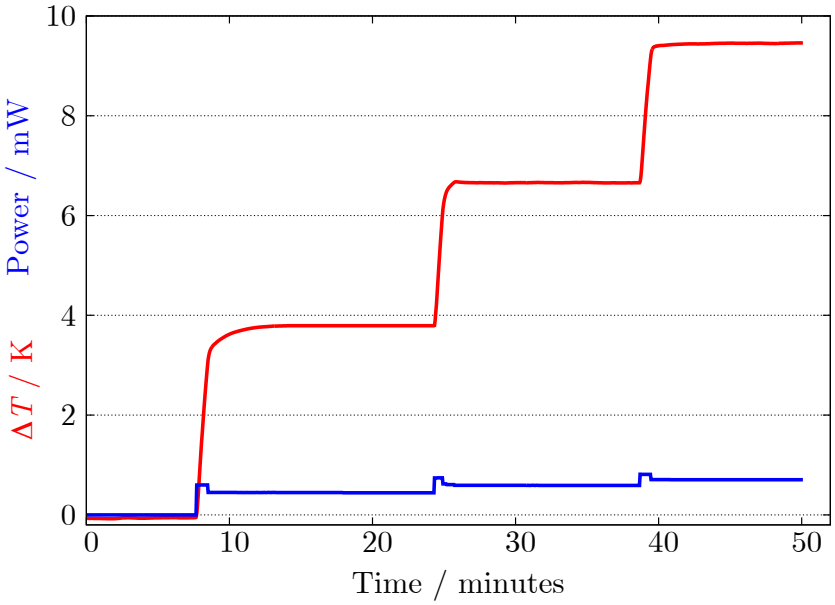


Figure 4.6: Typical temperature and heater power versus time for a parallel thermal conductance run at 300 K. $\Delta T$ was increase to 1, 2, and 3% of the system temperature.

Three measurements were required to accurately calculate thermal conductivity: a total measurement, with the sample connected to both platforms; a radiation measurement, with the sample only connected to the hot stage; and a background measurement, with the sample completely detached. The sample thermal conductance is then given by:

$$\underbrace{K_s}_{\text{sample}} = \underbrace{K_{tot}}_{\text{total}} - \underbrace{K_b}_{\text{background}} - \underbrace{\frac{1}{2}\left(K_r - K_b\right)}_{\text{radiation}}. \tag{4.1}$$

The factor of 1/2 on the radiation contribution has been estimated by considering the differences in the thermal gradient across the sample when it is both connected and disconnected from the cold stage [74]. The radiation from the entire sample is $R_H \propto L\,(T_H^4 - T^4)$, whereas that of the sample under a linear temperature gradient (sample detached from cold stage) is $R_{LG} \propto \int_0^L \left[T(l)^4 - T^4\right] dl$, where $L$ is the sample length, $T_H$ is the heater temperature, and $T(l)$ is the temperature of the sample at point $l$. When these two equations are compared, a factor near 0.5 is obtained.

The PTC method has the advantage of measuring a large effective length of yarn, typically  8 cm. In comparison, many other thermal conductivity measurement techniques measure much less sample: 1 mm to 1 cm for $3\omega$ [60, 75]; $<$ 1 cm for T-type probe [76]; $<$ 5 cm for comparative approaches [77]). Measuring small lengths of sample makes localized bulk defects a possible source of significant uncertainty.

The downside of the PTC technique is the amount of time required for the system to reach thermal equilibrium, especially below 200 K. A set of data (sample, radiation, and background measurements) from 300 to 50 K often took several days to collect.

### 4.4.2 Electrical Resistance

As discussed in Section 2.1, electrical resistance must be measured to calculate a material's electrical conductivity. Much like $\kappa$ measurements, $\sigma$ measurements are designed to create 1D transport of charge carriers through a material. In-line electrical resistance can be measured using either a 2-wire or 4-wire configuration. In the 2-wire method the end contacts are used to both apply current, $I$, and measure the corresponding voltage, $V$, whereas in the 4-wire method, shown in Figure 4.7(a), separate contacts are used to apply $I$ and measure $V$. In the 2-wire setup, the resistances of the leads and contacts can make a non-negligible contribution to the measured voltage, $V_{2-wire}$

$$V_{2-wire} = IR_{sample} + 2IR_{lead} + 2IR_{contact}. \tag{4.2}$$

In a 4-wire measurement, the current through the voltmeter, $I_V$, is low ($I_V << I$), and the measured voltage (and therefore resistance) is essentially independent of both the lead and contact resistances, as shown by:

$$V_{meas,4-wire} = (I - I_V)\, R_{sample} - 2I_V R_{lead} - 2I_V R_{contact} \approx IR_{sample} + 2IR_{lead}. \tag{4.3}$$

The electrical conductivity can then be calculated from $\sigma = RA/L$, where $L$ is the length between the inner voltage leads and $A$ is the cross-sectional area of the material.

The electrical resistance of the CNT yarns was measured as a function of temperature from 390 K to 2 K using a custom-built 4-wire resistance puck for the PPMS, shown in Figure 4.7(b). This puck performs 4-wire resistance measurements for two yarn samples. Samples were attached to the leads using conductivity silver paint (Dupont 4929N) to minimize contact resistance. Care was taken to prevent silver paint from wicking along the sample between the platform leads

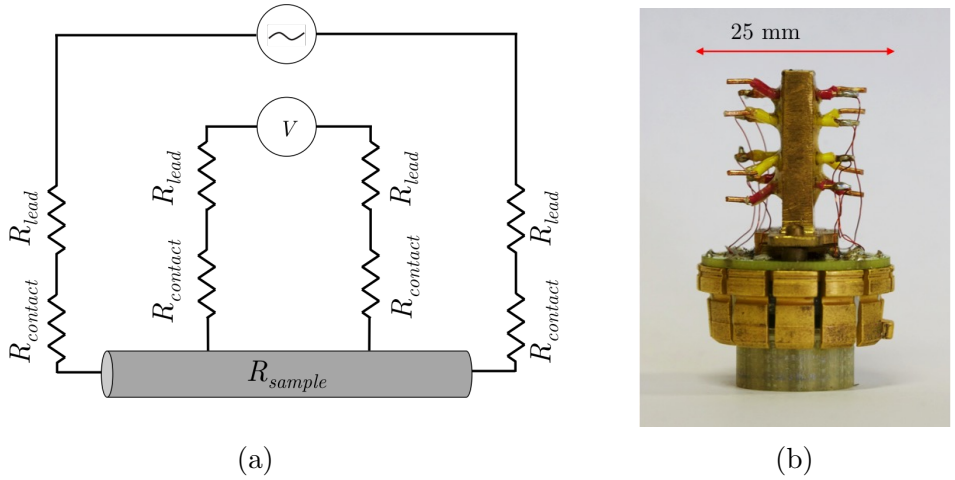


Figure 4.7: (a) Circuit diagram of a 4-wire resistance measurement. Adapted from [73]. (b) The PPMS resistivity sample platform used to measure the resistance of CNT yarns. Samples were attached to the four posts using silver paste.

Electrical resistance measurements were made using the PPMS as a cryogenic chamber, with AC current (93 Hz) with $I = 0.1$ mA for 0.5 s under vacuum ($\sim$3 Torr). AC current was used to minimize electromagnetic line interference, and small currents were used to minimize Joule heating. Values of $R$ for the CNT yarns were typically on the order of 100 to 300 $\Omega$.

Magnetoresistance was measured parallel to the yarn axis up to 9 T at various temperatures between 390 K to 2 K. $IV$-curves were measured from -1 to +1 mA at 60 Hz at the same temperatures as magnetoresistance.

### 4.4.3 High-Current Failure

The thermal failure in atmosphere of the CNT yarns at high current was studied. This is an important consideration for CNT yarns, especially if they are to replace metal wire for high-current carrying applications. Individual CNTs have excellent maximum current densities. However, in CNT yarns bulk defects and impurities limit the maximum current carrying capacity. Joule heating of the yarn at high currents causes thermal breakdown and failure of the yarn [78].

High-current failure was studied using a Keithley 220 constant current source in a 2-wire configuration. Sections of yarn ($\sim$1 cm) were attached directly to banana plugs using silver paste, which were attached to the current source. A DMM was used to measure the corresponding voltage across the yarn. LabVIEW was used to control the current and measure voltage. The current was increased by 1 mA every 2 s until the yarn failed. The results are discussed in Chapter 5.

# Chapter 5

# Results

## 5.1 Scanning Electron Microscopy

Scanning electron microscopy was performed to study the qualitative affects of annealing on the CNT yarn structure, and also to measure the yarn diameter. Figure 5.1 shows SEM micrographs of yarns after three different annealing conditions. The pristine yarn, Figure 5.1(a), shows a uniform diameter, with a $\sim 35^{\circ}$ twist angle and few dangling CNT bundles. However, the pristine yarn surface appears to be loosely wound, suggesting the packing density of the yarn cross section is low.

The annealed yarns, shown in Figures 5.1(b) and 5.1(c), appear to have a high density structure. It should be noted that the decrease in diameter after annealing shown in Figure 5.1 is likely not entirely due to the annealing process, but also from variations in diameter between the sections of the same yarn that were annealed and those that were not. After annealing, the yarn surface structure appears more dense and uniform. There are, however, more dangling CNT bundles on the surface, which could be detrimental to transport properties. These dangling bundles were likely caused by the handling that the annealed yarns experienced while being wrapped around the graphite rod before annealing.

The different sections of the annealed yarn typically showed diameter fluctuations on the order of $\pm 3$ $\mu$m from the average. However, different regions of the pristine yarns showed significant variation, up to a 15 $\mu$m variation in diameter over $\sim$50 cm in length for the yarns produced by Array 2 (45 $\mu$m to 60 $\mu$m). There was no clear trend in how the yarn diameter changed after annealing, however, the diameters of

each yarn appeared to only change by $\pm 3$ $\mu$m after annealing, which is within the range of diameter fluctuations typically observed for dry-spun CNT yarns.

The surface twist angle, $\theta$, was also measured for each yarn and was used to calculate the residual twist from Equation 3.3. Figure 5.2(a) demonstrates that the yarn diameter increased linearly with surface twist angle. Figure 5.2(b) shows the residual twist density of each yarn, $\tau$, calculated using Equation 5.2(a).

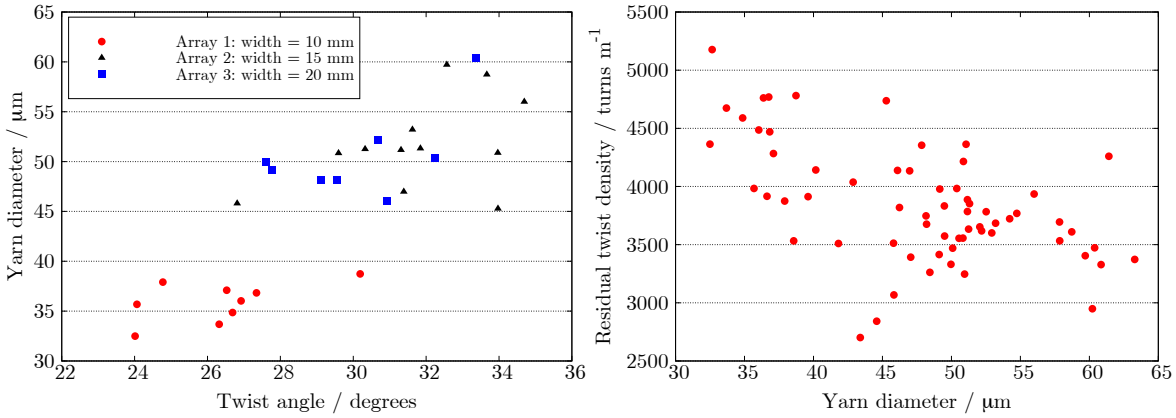


Figure 5.2: Structural characteristics of dry-spun CNT yarns, as measured using scanning electron microscopy: (a) CNT yarn diameter versus residual surface twist angle and (b) residual twist density versus CNT yarn diameter.

Figure 5.2(a) shows that the array produced from the narrowest substrate (10 mm), Array 1, had the smallest diameter and smallest residual twist angle. For Arrays 2 and 3 the twist angle and diameter increased with array width. Figure 5.2(b) show that the value of residual twist density varies nearly linearly between $\sim 3000$ m$^{-1}$ and 5000 m$^{-1}$ with decreasing yarn diameter.

As discussed in Section 3.2.2.2, the residual twist density is one of the most important properties governing the CNT yarn structure and physical properties. The increase in residual twist density with decreasing yarn diameter suggests that the porosity of the yarn cross section likely increases with yarn diameter, meaning that the large diameter yarns will be less dense. The impact of yarn diameter on electrical and thermal conductivity will be discussed in Sections 5.3.2 and 5.5, respectively.

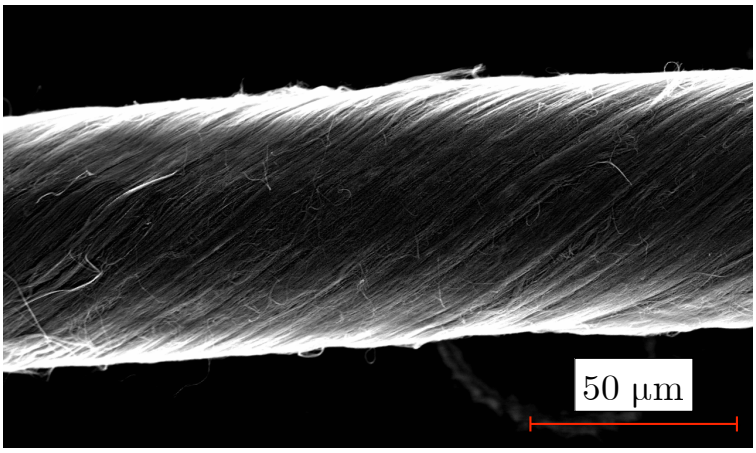


(a) pristine

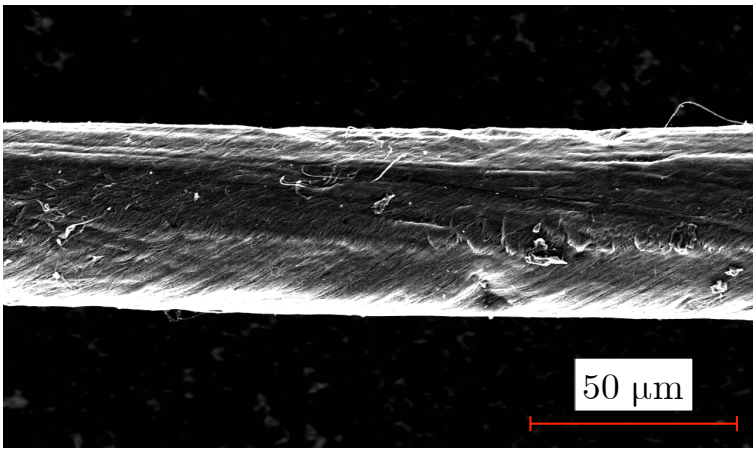


(b) 2300 °C

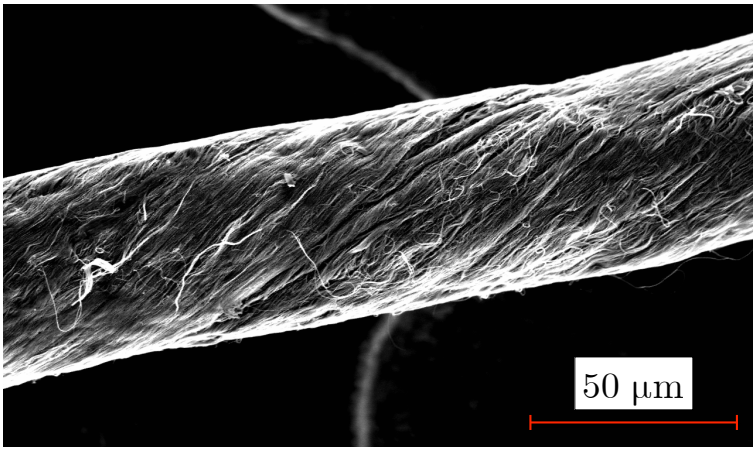


(c) 2700 °C

Figure 5.1: SEM micrographs of CNT yarns after different annealing conditions: (a) pristine (b) 2300 °C (c) 2700 °C.

## 5.2 Raman Spectroscopy

The normalized Raman spectrum for the pristine and annealed 35 $\mu$m CNT yarns are shown in Figure 5.3, including all peak designations. The most significant peaks are the D-peak at 1350 cm$^{-1}$, the G-peak at 1580 cm$^{-1}$, and the G' overtone peak at 2700 cm$^{-1}$ [55]. As discussed in Section 3.3, the relative intensities of the G-peak and D-peak, $I_G/I_D$, can be used as a qualitative measure of the crystallinity of a CNT material. For this pristine sample, the value of $I_G/I_D$ is ~2, which is high for pristine CNT materials. This confirms that the CVD method used in this work produces high quality CNTs, even without any post-processing.

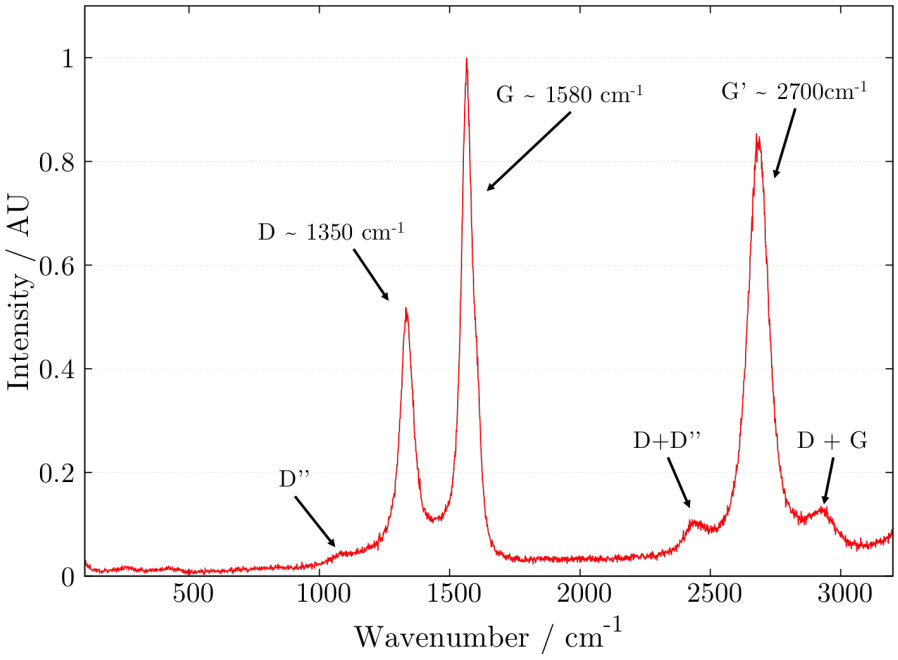


Figure 5.3: Raman spectrum of a 35 $\mu$m pristine CNT yarn with intensity normalized to the G-mode peak at 1580 cm$^{-1}$.

The Raman spectra of each yarn was measured before and after high temperature annealing to quantify the increase in CNT crystallinity. Figure 5.4(a) to 5.4(c) show the Raman spectra for the differently annealed yarns from each of the three arrays. It

should be noted that the slight frequency shifts observed in Figure 5.4 cannot be confirmed as frequency standards were not present during data collection.For each yarn, the value of $I_G/I_D$ increased continuously with annealing temperature, confirming that high-temperature annealing improved the relative crystallinity of the CNTs.

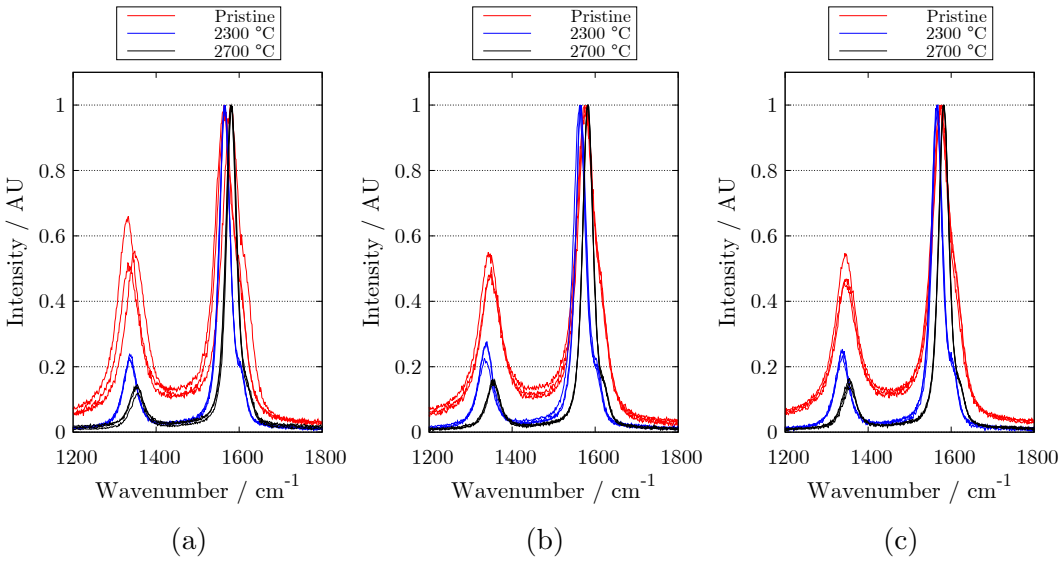


Figure 5.4: Raman D- and G-peaks of (a) 35 $\mu$m (b) $\sim$ 45 $\mu$m (c) $\sim$ 50 $\mu$m CNT yarns. Each sample shows a decrease in the relative intensity of the D-band to the G-band after high-temperature annealing. Raman spectra were collected from three points along each yarn.

The spectrum of each pristine sample featured high-intensity backgrounds between the D-peaks and G- peaks (1400 cm$^{-1}$ to 1500 cm$^{-1}$). This background corresponds to tetrahedral (sp$^3$) amorphous carbon, which has a broad Raman peak centred near 1550 cm$^{-1}$, as shown in Figure 3.8 [55]. After annealing, each sample shows a significant decrease in this background, which confirmed the amorphous carbon was either removed completely or hybridized to sp$^2$ carbon [79]. The backgrounds remain unchanged between the 2300 °C and 2700 °C annealed samples, which suggests that there was insignificant change to the amorphous carbon content after annealing above 2300 °C. The full-width at half maximum (FWHM) of the Raman peaks is related to the uniformity of the crystalline structure [22]. The FWHM of each band

decreased after annealing to 2300 °C, but remained essentially unchanged after annealing at 2700 °C. Also, the intensity of the second-order peaks and their overtones (G', D"+D, D+G) increased after annealing, implying that there was more structural ordering in the CNTs [56].

Figure 5.5 shows a summary of $I_G/I_D$ values for various CNTs and CNT materials as a function of annealing temperature in Ar atmosphere, including results from this work (large circles). Each CNT material shows a very similar evolution of increasing $I_G/I_D$ with annealing temperature.

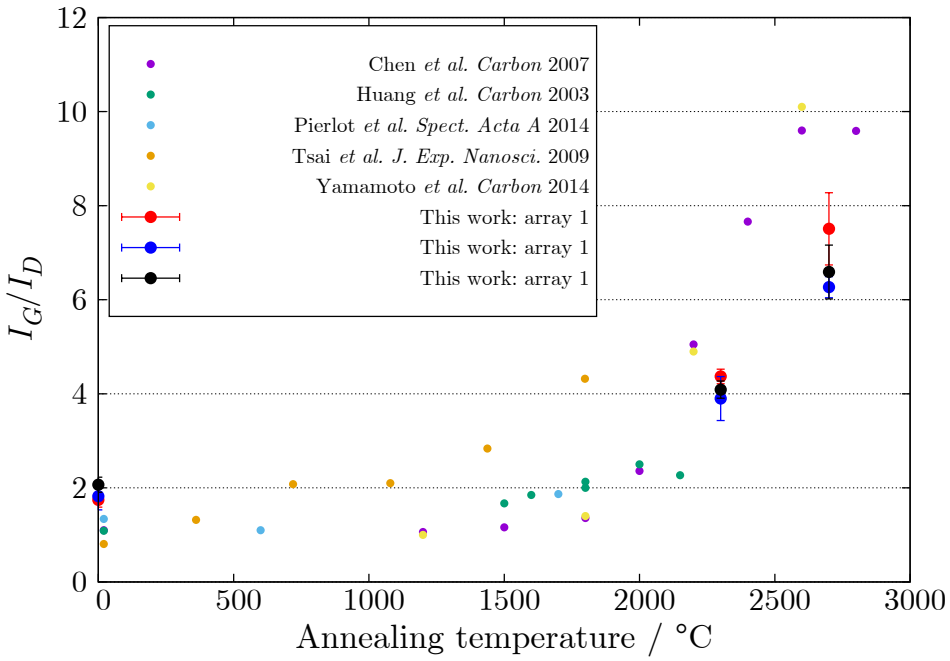


Figure 5.5: Summary of the Raman spectroscopy $I_G/I_D$ ratios as a function of annealing temperature for various CNT materials, including the CNT yarns studied in this work, and data from Refs. [14, 62, 63, 64, 65]. Pristine samples are shown at the left axis.

## 5.3 Electrical Properties

### 5.3.1 Influence of Adsorbed Gases

It has recently been demonstrated that adsorbed species can have a large effect on the electrical properties of CNT yarns, as discussed in Section 3.2.4.1 [52]. This influence is not often discussed in the literature, which can lead to confusion when comparing results between different groups. In an attempt to further understand this behaviour, the influence of atmospheric oxygen and water on the electrical properties of CNT yarns was studied by measuring resistance at various levels of vacuum at 300 K in the PPMS. Figure 5.6 shows the percent change in electrical resistance as a function of PPMS chamber pressure for two 60 $\mu$m pristine CNT yarns. Measurements were made using the 4-wire method discussed in Section 4.4.2. The high pressure value at 760 Torr corresponds to the atmosphere (outside the PPMS chamber), whereas the other measurements were made in the PPMS chamber (3, 0.9, and $\sim 10^{-4}$ Torr).

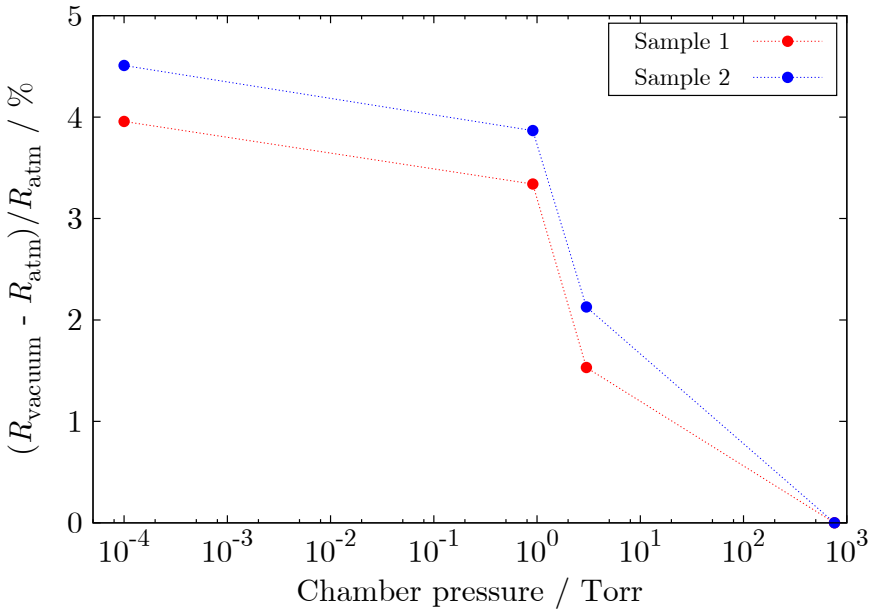


Figure 5.6: Percent change in resistance ($(R_{vacuum} - R_{atmosphere})/R_{atmosphere}$) at various vacuum pressures relative to atmosphere at $T = 300$ K for two 60 $\mu$m pristine CNT yarns. Similar pressure dependence was observed for annealed yarns. Lines are included as a guide to the eye.

Each yarn studied had a qualitatively similar pressure dependence to that shown in Figure 5.6. The total change in resistance ranged from $4-8$ % at $10^{-4}$ Torr. There was no clear dependence on annealing temperature or yarn diameter. This increase in resistance is associated with the removal of some adsorbed oxygen species on the surface of the CNT yarns. At 300 K the vacuum used during PPMS resistivity measurements is likely insufficient to remove adsorbed oxygen and water, and therefore complete degassing should be done at higher temperatures [49].

The hysteresis in $R(T)$ on heating and cooling in vacuum was also studied for pristine and annealed yarn. Yarns were loaded in the PPMS and then the chamber was evacuated (0.9 Torr). Resistance was then measured as temperature was cycled between 2 K and 390 K at a rate of 2 K·min$^{-1}$. When 390 K was achieved at this temperature scanning rate, resistance reached a steady state, and changed less than 0.1 Ω (0.05 %) after 20 minutes.

Figure 5.7 shows resistance as a function of temperature before and after degassing for a 50 $\mu$m pristine CNT yarn.

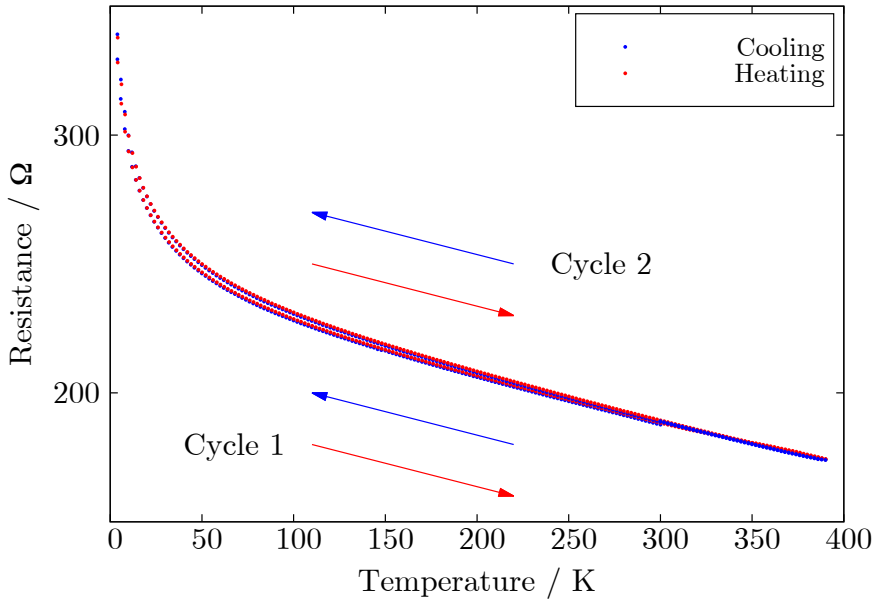


Figure 5.7: Hysteresis in $R(T)$ for a 50 $\mu$m pristine CNT yarn in vacuum (0.9 Torr) between 390 K and 2 K. Resistance changed by 1 to 5 Ω ($\sim$ 0.5 to 2 %) after degassing, significantly less than observed for the annealed yarns (Figure 5.8).

This pristine yarns showed only a small transition ($< 10\%$ increase in $R$) after degassing at 390 K. This is likely because the adsorbed gases were more strongly bound to the CNT pristine yarn structure, and were not completely removed, even in vacuum at 390 K. Degassing would likely need to take place at up to 800 K [52], but this temperature is not attainable in the PPMS.

Figure 5.8 shows the hysteresis in $R(T)$ for a 50 $\mu$m 2700 °C annealed yarn. The first first heating and cooling cycle, from 300 K to 2 K and back to 300 K, shows negligible changes in the resistance at 300 K (<1 Ω, 0.25 %). This result implies that low temperatures have no permanent effect on the electrical properties of the yarns.

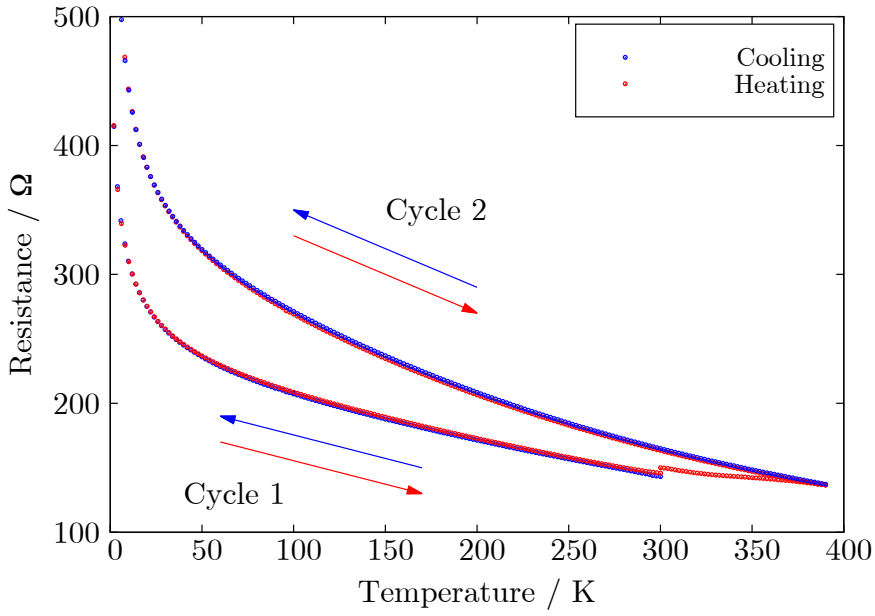


Figure 5.8: Hysteresis in $R(T)$ for a 50 $\mu$m 2700 °C annealed CNT yarn in vacuum (0.9 Torr) between 390 K and 2 K. No hysteresis was observed upon cooling from 300 K to 2 K, but a 27 % increase in $R$(300 K) occured after heating to 390 K. This increase in $R$ remained down to 2 K, with no hysteresis observed after heating back to 390 K.

However, considerable hysteresis, between 20 % and 50 %, was observed after heating from 300 K to 390 K and back. This is because of the removal of adsorbed oxygen and, likely more importantly, as discussed in Section 3.2.4.1, $H_2O$ molecules [52]. The resistance of the degassed sample remained higher than that of the saturated

sample on the subsequent cooling cycle to 2 K. As before, there was no significant hysteresis in $R(T)$ from 2 K to 300 K after the yarn had been degassed.

Figure 5.9 shows the high-temperature hysteresis in $R(T)$ following 24 hours exposure to atmosphere (21 °C, >90 % relative humidity) after the initial degassing. Upon reentry in vacuum, the 300 K resistance value decreased from 27% above the initial value down to 14%, showing that some oxygen and water were re-adsorbed onto the yarn. After the second degassing, the resistance returned to the same value as after the first degassing.

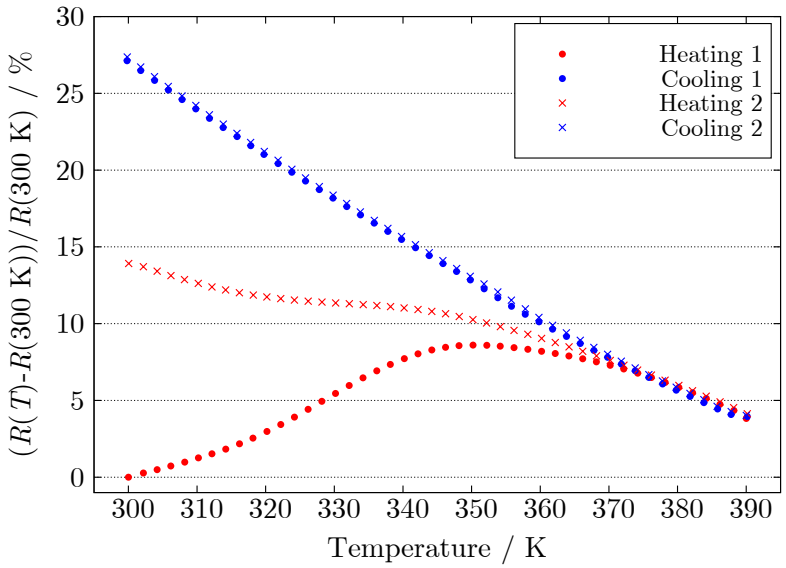


Figure 5.9: Percent change in $R(T)$ in vacuum (0.9 Torr) from 300 K to 390 K relative to $R(300\ \mathrm{K})$ after first exposure to vacuum. Solid circles are from the first degassing, and crosses are from the second degassing after 24 hours in atmosphere.

In conclusion, the electrical properties of CNT yarns clearly depend on their exposure to atmosphere, with changes in resistance of ∼20 % observed after degassing. This behaviour must be considered when creating CNT yarns for electrical applications, since changes to resistance will after the performance and lifetime of the yarn.

### 5.3.2 Electrical conductivity

Each measurement of electrical resistance for the different yarns was made under vacuum (0.9 Torr) from 390 K to 2 K to ensure degassing. As shown in Figure 5.7, the electrical resistance these CNT yarns decreased monotonically with temperature, implying semiconducting behaviour [10]. The electrical conductivity, $\sigma(T)$, was calculated using resistance and yarn diameter as measured using SEM. The largest contribution to the uncertainty in $\sigma$ is the yarn diameter, which typically had standard deviations of 1 $\mu$m to 2 $\mu$m over each section of yarn, as measured by SEM.

Figures 5.10 (a) and (b) show the electrical resistance and electrical conductivity of $\sim$50 $\mu$m CNT yarns after annealing at different temperatures.

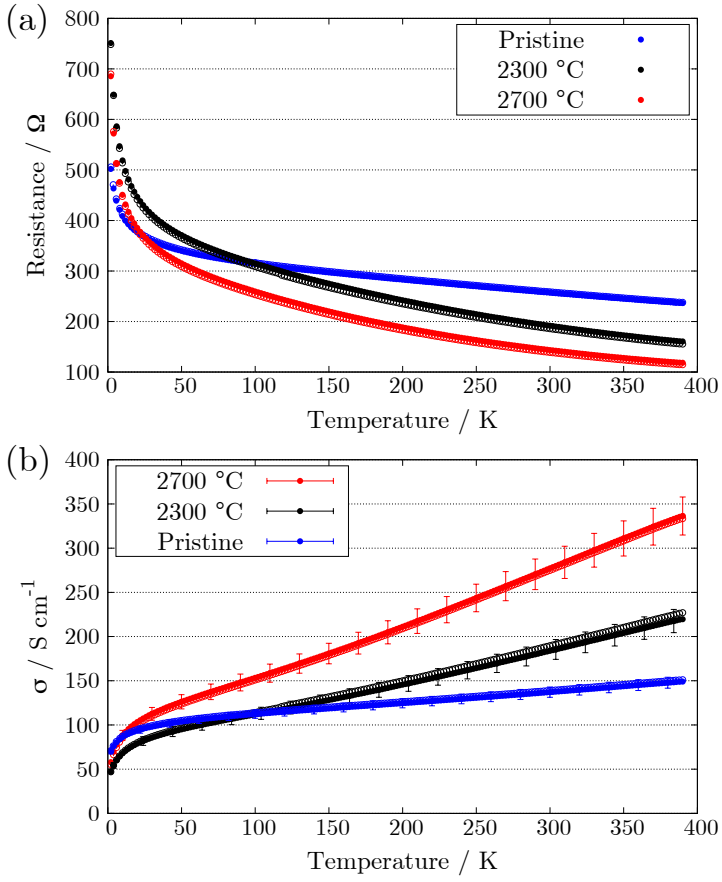


Figure 5.10: (a) Electrical resistance and (b) electrical conductivity of $\sim$50 $\mu$m CNT yarns after high-temperature annealing. All samples were heated to 390 K in vacuum (0.9 Torr) before measurement in an attempt to remove absorbed oxygen and water.

Figure 5.10 shows that high-temperature annealing improved $\sigma$ relative to the pristine samples. Results are shown for two pieces of each yarn, which demonstrates how consistent the measurement processes is for $\sigma(T)$ at all temperatures. The electrical conductivity of the 35 $\mu$m yarns show qualitatively similar temperature and annealing dependence as that observed for the 50 $\mu$m yarns.

The most obvious change in $\sigma(T)$ after annealing was the increased slope, which has been observed in other annealed CNT materials [80, 81]. The temperature dependence of electrical conductivity will be discussed further in Section 5.3.2.1.

Figure 5.11 shows a summary of the $T = 300$ K electrical conductivities for each differently prepared CNT yarn. The conductivities included in Figure 5.11 are all for degassed yarns. It is important to note that when comparing these values to non-degassed samples, about 20 % should be added to the conductivities of the annealed samples. Annealed to 2300 °C and 2700 °C increased $\sigma$(300 K) by ~40 % and ~200 % for both the 35 $\mu$m and 50 $\mu$m yarns.

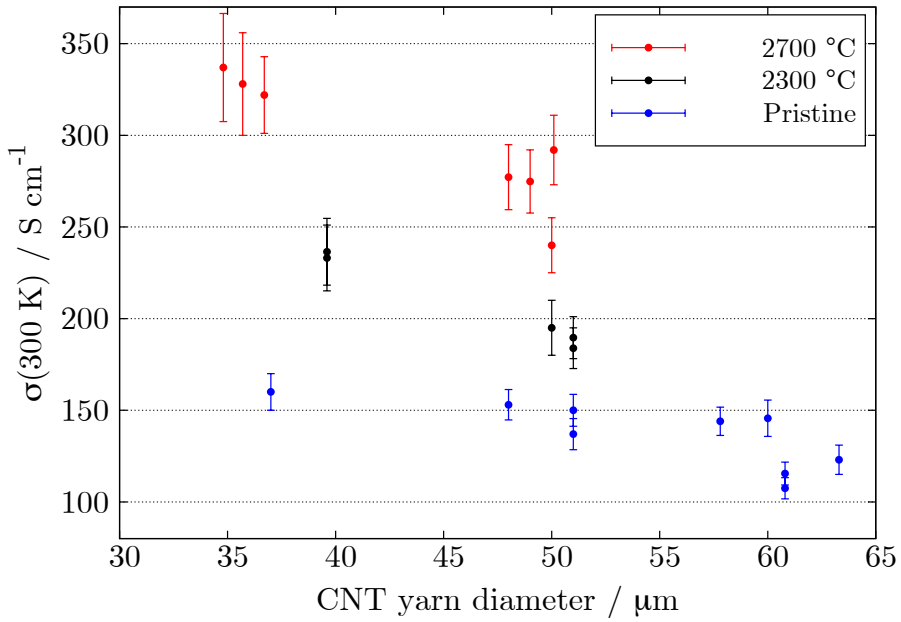


Figure 5.11: $\sigma$(300 K) versus diameter for various CNT yarns before and after high-temperature annealing. All samples were degassed at 390 K and $10^{-4}$ Torr. The uncertainty in diameter is typically 1.5 $\mu$m.

Figure 5.11 also shows that increasing yarn diameter clearly causes a decrease in electrical conductivity, regardless of annealing temperature, which suggests the CNT yarns are not homogeneous. Jakubinek *et al.* previously studied the effect of yarn diameter on $\sigma$ for dry-spun yarns produced in a very similar method to those used in this work [6]. Figure 5.12 shows electrical conductivity of pristine CNT yarns as a function of yarn diameter, using data from the present work and from Ref. [6].

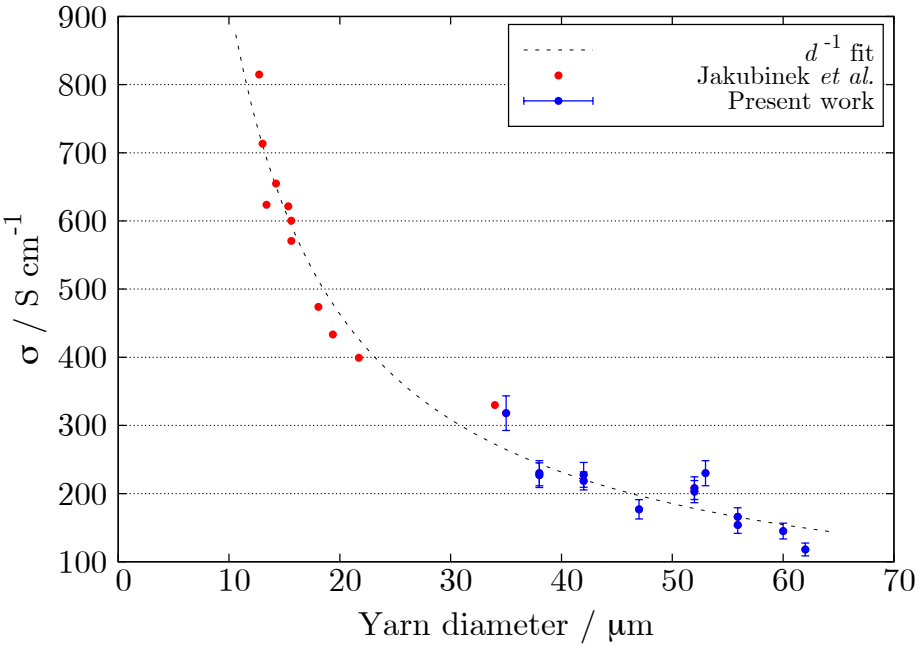


Figure 5.12: CNT yarn $T = 300$ K electrical conductivity versus diameter, $d$, with data from Ref. [6], including a fit to $d^{-1}$.

Figure 5.12 shows that $\sigma$ decreases roughly as $d^{-1}$. As discussed in Section 3.2.2.2, the dependence of $\sigma$ on yarn diameter is most likely because the density of small diameter yarns is greater than that of large diameter yarns. As a result, the calculated values of $\sigma$ are lower for larger diameter yarns. If density is roughly inversely proportional to diameter ($\rho \sim 1/d$), and conductivity is also inversely proportional to diameter ($\sigma \sim 1/d$), then the specific conductivity, $\sigma/\rho$ would be constant, as observed previously [43].

It has been suggested that the Raman $I_G/I_D$ ratio could be used as a predictor of the relative electrical conductivities of CNT materials [57]. This is confirmed in the present work, with Figure 5.13 showing $\sigma$(300 K) versus Raman $I_G/I_D$. The nearly linear increase in $\sigma$ with $I_G/I_D$ suggest that Raman spectroscopy can be used as a quality control method to quickly assess the relative electrical conductivity of CNT yarns immediately after manufacturing.

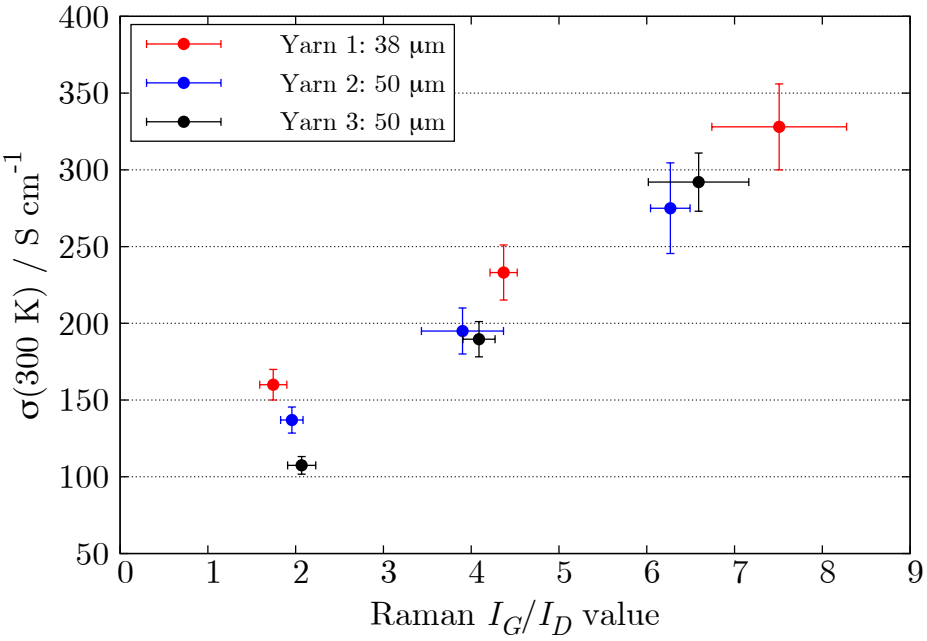


Figure 5.13: $T$ = 300 K electrical conductivities after degassing at $T$ = 390 K as a function of Raman $I_G/I_D$ ratio of three different CNT yarn samples. A nearly linear increase in $\sigma$ was observed with increasing annealing temperature.

#### 5.3.2.1 Temperature Dependence of Electrical Conductivity

Several models have been proposed to explain the temperature dependence of electrical conductivity for CNT yarns, but there is still no consensus, and no global explanation that works over a wide temperature range [48]. One of the simplest and versatile models of $\sigma(T)$ for CNTs and CNT materials, Equation 2.15, combines metallic conduction, tunneling barriers, phonon backscattering, and variable range hopping [10, 82].

For bulk CNT materials such as the CNT yarns studied in this work, the metallic term is often insignificant in comparison with the other terms, and can therefore be ignored. Equation 2.15 now simplifies to:

$$\sigma(T) = D \exp\left(-\frac{T_b}{T_s + T}\right) + C \exp\left(-\left(\frac{T_0}{T}\right)^{\frac{1}{1+d}}\right) \tag{5.1}$$

where $D = A^{-1}$. The hopping dimensionality, $d$, was taken to be 3 for simplicity.

Figure 5.14 shows the fits to the normalized conductivity, $\sigma(T)/\sigma(300\text{ K})$ using Equation 2.15 for a pristine, 2300 °C, and 2700 °C annealed yarn, each with diameters of $\sim 50$ $\mu$m. The fits for each yarn show excellent agreement with the experimental results from 2 K to 300 K.

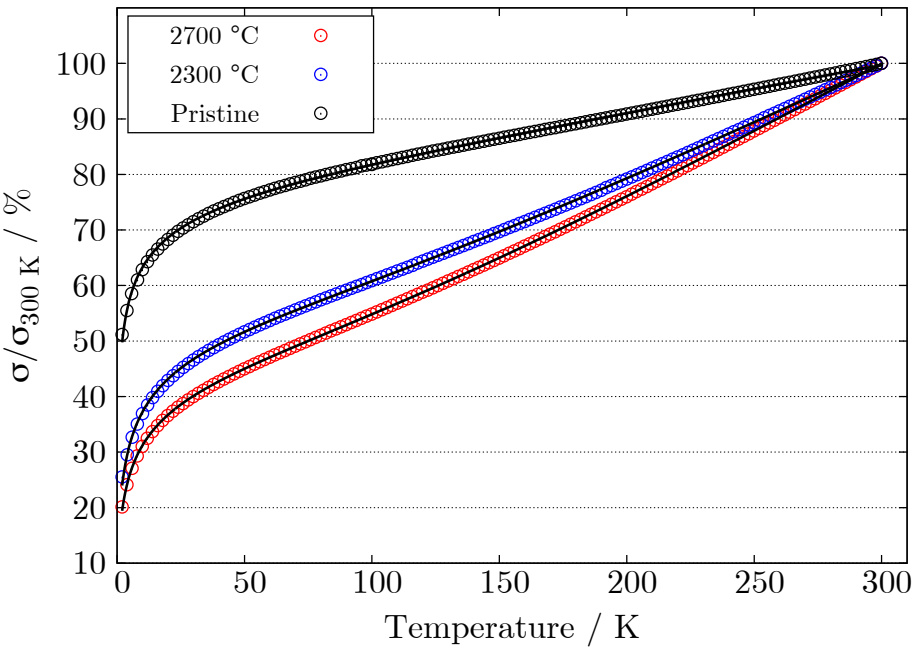


Figure 5.14: Experimental data (open circles) and fits (solid lines) to $\sigma(T)$ for differently annealed 50 $\mu$m CNT yarns calculated using Equation 5.1. The fits show good agreement with the data across the entire temperature range.

The fit parameters from Equation 5.1 for each CNT yarn shown in Figure 5.14 are summarized in Table 5.1. The values of $T_b$ and $T_s$ drop for the 2300 °C, but remain

constant to 2700 °C. This means the onset temperature for thermal voltage fluctuations is decreased by annealing. The value of $T_0$ increased after annealing from 0.6 K for the pristine sample to 8.9 K for the 2700 °C annealed sample, implying that the hopping distance of the electrons decreases. The decreased hopping distance means that there are more nearby states with accessible energies at a given temperature for the annealed samples, and therefore electrons do not have to hop as far [10]. Similar trends were observed for the 35 $\mu$m yarns.

Table 5.1: Summary of the fit parameters from Equation 5.1 for differently annealed CNT yarns.

| Annealing temperature | D / S·cm$^{-1}$ | C / S·cm$^{-1}$ | $T_b$ / K | $T_s$ / K | $T_0$ / K |
|---|---|---|---|---|---|
| Pristine | 213 | 138 | 1190 | 250 | 0.6 |
| 2300 °C | 631 | 164 | 979 | 148 | 6.4 |
| 2700 °C | 1110 | 219 | 972 | 152 | 8.9 |

Figure 5.15 shows a breakdown of the tunneling and hopping contributions to the fit of $\sigma(T)$, normalized by $\sigma(300\ \mathrm{K})$.

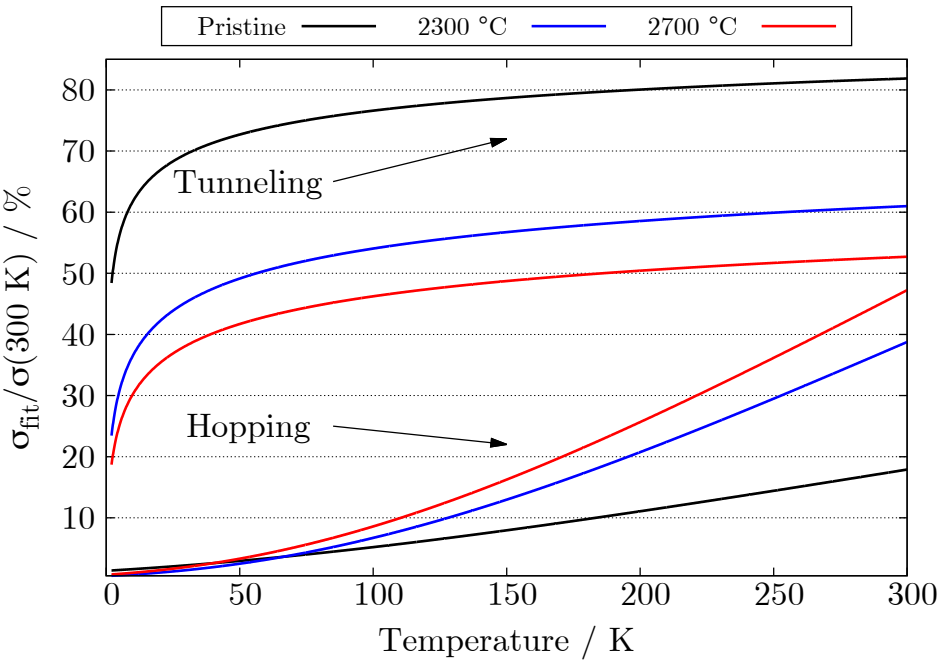


Figure 5.15: Hopping and tunneling contributions from Equation 5.1 to the fit of $\sigma(T)$ for three differently annealed 50 $\mu$m CNT yarns, normalized to $\sigma(300\ \mathrm{K})$.

After annealing, the relative contribution of tunneling drops and the relative hopping contribution increases. However, the value of tunneling conductance appears to plateaus above 300 K to $\sim$120 S·cm$^{-1}$ regardless of annealing temperature. The main difference between the differently annealing yarns comes from the increased tunneling conductance.

In the pristine samples, the values of $\sigma/\sigma(300\text{ K})$ remained significant at low temperatures, and appear to extrapolate to a non-zero conductivity as $T \rightarrow 0$ K. This was likely due to the presence of metal catalyst particles in the pristine samples (Figure 3.11), which increased the contribution of tunneling between metallic regions at low temperatures, as seen in Figure 5.15. The low resistance of the pristine sample relative to the annealed samples at low temperature is also seen in Figure 5.10 (a).

Although this model provides a qualitative fit to the electrical conductivities of the CNT yarns from 2 K to 300 K, it provides limited potential for interpretation of the physical characteristics of the CNT yarns. This model (Equation 5.1) was designed for conductive polymers and disordered metals, not nanotubes. Therefore, some of the details of CNT conduction are not included, such as: conduction through the inner tubes of MWCNTs at higher temperatures; possible temperature dependence of CNT-CNT contact resistance; and the influence of metal catalyst nanoparticles. Ideally, a model of $\sigma(T)$ would provide useful information about the properties of the individual CNTs, the macroscopic yarn morphology, and the influence of any dopants. Lekawa-Raus *et al.* recently developed a model to describe $\sigma(T)$ for reactor-spun CNT fibres [83]. Although this model provides some quantitative information about the CNT fibre properties, the differences in $\sigma(T)$ between reaction-spun CNT fibres and dry-spun MWCNT yarns makes it unsuitable for the yarns studied in this work.

### 5.3.3 *IV*-curves

The *IV*-curves of the differently annealed ∼50 $\mu$m CNT yarns from -1 mA to 1 mA are shown in Figure 5.16. Each *IV*-curve for the CNT yarns had linear behaviour, as expected by Ohm's law, at both 300 K and 100 K. The *IV*-curves of the other diameter yarns show similar behaviour, and will therefore not be shown. Below 50 K, however, the curves became slightly non-ohmic (non-linear), and by 20 K the non-linearity was very apparent. Non-linearity in *IV*-curves has been reported in many CNT materials, and is often attributed to quantum phenomena, such as Coulomb blockade [9]. However, the heat capacity of CNT materials is extremely low below 50 K, making Joule heating a possible source of the non-linearity of the *IV*-curves.

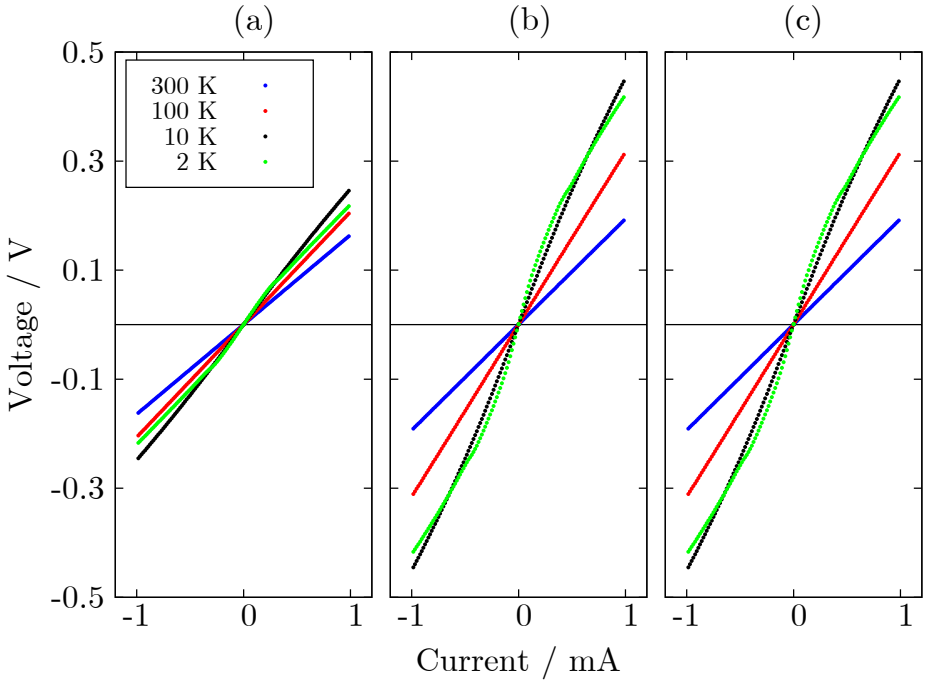


Figure 5.16: *IV*-curves of 45 $\mu$m CNT yarns: (a) pristine (b) 2300 °C (c) 2700 °C. Non-ohmic behaviour is observed for each sample below 50 K.

Accurately calculating the contribution from Joule heating to the non-ohmic behaviour of the *IV*-curves is difficult because the measurement conditions are far from adiabatic. However, given that the heat capacity of CNT materials is small at low

temperatures, Joule heating is likely not insignificant at low temperatures. For example, Pöhls *et al.* measured the heat capacity of compacted CNT sheets using relaxation calorimetry [5]. The sheets used in that work were prepared from CVD grown arrays that were essentially identical to the arrays used to produce the CNT yarns in this work, and should therefore provide a good estimate of the CNT yarn heat capacity. The heat capacity of the CNT sheets was $\sim$0.8 J·g$^{-1}$ at 300 K, and $< 0.005$ J·g$^{-1}$ for temperatures below 10 K.

Two methods were used to test for Joule heating in the 2 K $IV$-curves: changing the initial direction of cycling (0 mA to 1 mA or 1 mA to 0 mA), and changing the measurement dwell time from 0.5 s to 4 s (the limits of the PPMS). Altering the cycle direction had a more apparent effect on the $IV$-curves. Figure 5.17 shows the $IV$-curves at $T = 2$ K for various 50 $\mu$m CNT yarns with different initial current directions, 0 mA to 1 mA (shown in red), and 1 mA to 0 mA (shown in blue).

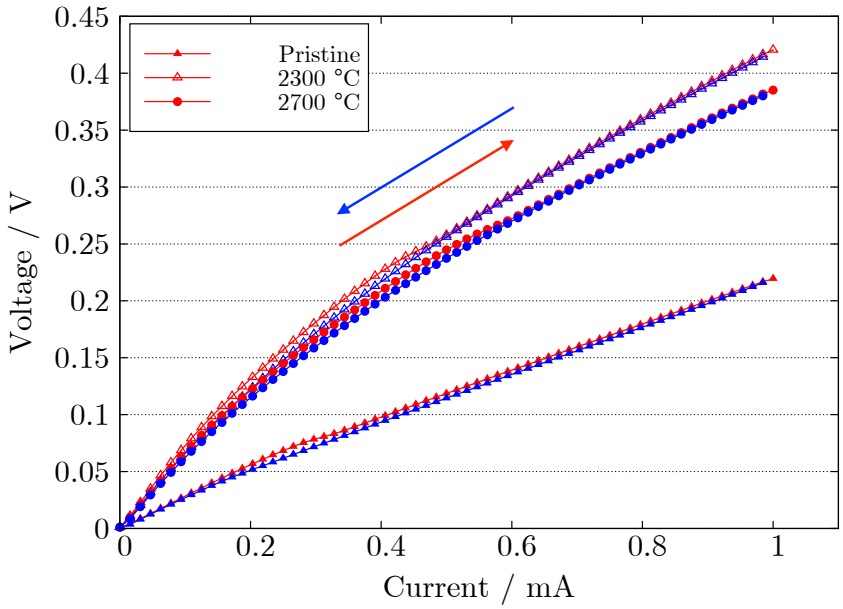


Figure 5.17: Hysteresis in $IV$-curves for a $\sim$50 $\mu$m CNT yarns upon different current cycle directions: 0 to 1 mA (red points) followed by 1 to 0 mA (blue points). The down cycle (blue) shows lower voltage (lower resistance) than the up cycle (red) curve below 0.6 mA, suggesting that Joule heating is significant in this range.

If Joule heating were significant, the slope of the $IV$-curve would decrease with increasing current, since, as shown in Figure 5.10, resistance decreased monotonically with increasing temperature for each yarn.

For the atmosphere-saturated yarns, increasing the dwell time from 0.5 s to 4 s did not cause a noticeable change in the $IV$-curve voltage ($< 0.1$ %) for all values of current. After degassing, the affect of increasing dwell time above 0.5 s was more apparent, with voltage increasing by $\sim$0.35 % and $\sim$0.55 % for dwell times of 2 s and 4s for annealed samples, but still $< 0.1$ % for the pristine samples. The increased degassing of the annealed yarns, as observed in Figure 5.8, is associated with the removal of adsorbed water and other gaseous species. Removing this water would decrease the heat capacity of the yarn, and thus increase the effect of Joule heating at low temperatures.

The Joule heating contribution to non-linearity is clearly significant, and therefore the quantum mechanical contribution to non-ohmic behaviour will not be discussed.

### 5.3.4 High-Current Failure

The current-voltage behaviour up to failure was measured in atmosphere for differently annealed 50 $\mu$m yarns. During measurements, as current was increased the CNT yarns began to glow. The intensity of the glow increased in a localized area ($\sim$1 mm) until the yarn suddenly snapped, producing a flash and vapourizing a small section ($<$1 mm) of the yarn. Shortly before failure the yarn began to glow, corresponding to the sharp up-turn in voltage observed in Figure 5.18. The glow was typically brightest near the midpoint between the two leads, but could be in a different location if a bulk defect was present in the yarn. Bulk defects are significant sources of resistance, and therefore cause the most Joule heating at high current.

Figure 5.18 shows the $IV$-curves up to failure for three sections of each different yarn. The different sections show very repeatable $IV$-curves and failure currents. For each yarn the high-current failure was very sudden, within ∼5 mA. Such sharp failure is unfavourable for high-current applications because it makes failure almost impossible to anticipate.

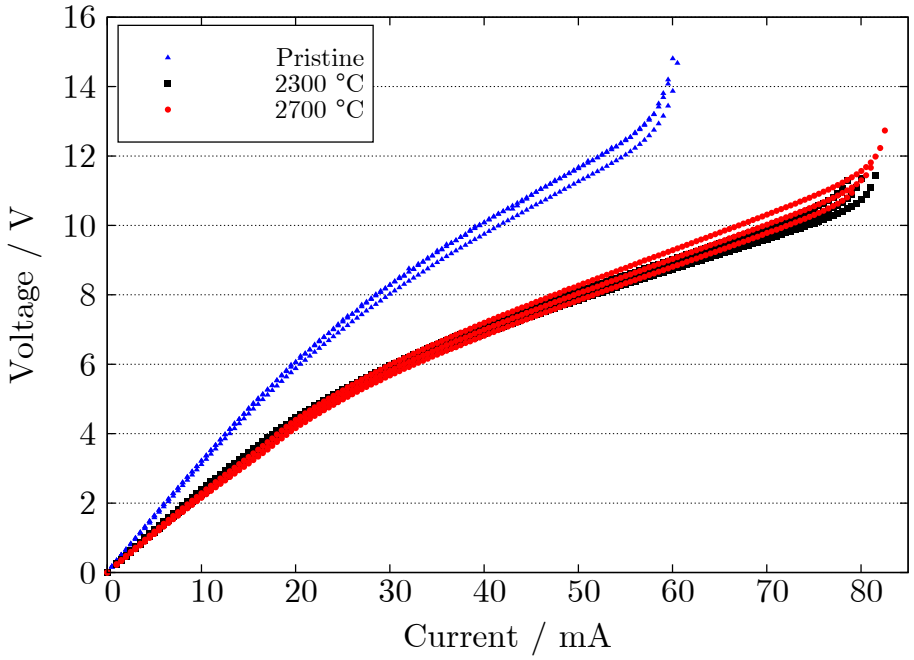


Figure 5.18: Current-voltage behaviour up to failure in atmosphere for several 50 $\mu$m CNT yarn samples.

The maximum current at failure for the pristine and annealed yarns were 60 mA and 80 mA, respectfully. High-temperature annealing has been shown previously to increase the maximum current density of individual CNTs [69]. Raman spectroscopy has shown that annealing decreased the defect density, which in turn reduced that number of oxygen-reactive sites. By decreasing the amount of oxygen on the CNTs, their oxidation temperature will be increased, as had been demonstrated previously in thermogravimetric analysis (TGA) measurements [84]

The structure of the yarn where failure occurred was studied using SEM. Figure 5.19 shows the vapourized end of a 60 $\mu$m pristine yarn. The yarn tip showed a very clean break, with an area only $\sim$150 $\mu$m from the break showing noticeable damage.

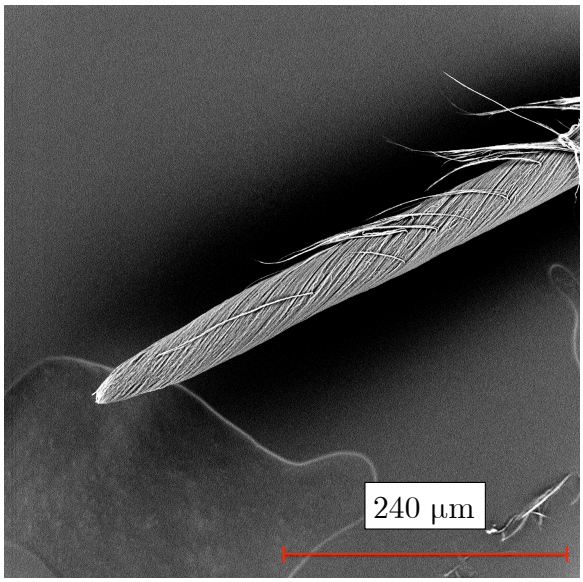


Figure 5.19: SEM micrograph of a 40 $\mu$m pristine CNT yarn after high-current thermal breakdown.

The maximum current densities measured under ambient conditions for the pristine and annealed yarns were 750 A·cm$^{-2}$ and 100 A·cm$^{-2}$, respectively, which compare well with values for other CNT yarns [48, 78]. Although these values are much lower than that for copper wires, they are sufficient for most applications. For example, the current density in domestic insulated copper wiring is typically 200 to 400 A·cm$^{-2}$ [52]. Therefore these CNT yarns could be useful in applications that do not require significant current.

## 5.4 Magnetoresistance

Magnetoresistance was measured as a function of temperature for each CNT yarn. Negative magnetoresistance was observed, as had been reported previously for CNT sheets [5] and yarns [6].

As with electrical conductivity, the magnetoresistance of the CNT yarns was measured before and after degassing at 390 K. Figure 5.20 shows magnetoresistance before and after degassing for a 50 $\mu$m pristine CNT yarn. The magnetoresistance transitioned from slightly positive before degassing to slightly negative after degassing, consistent with the slight positive magnetoresistance measured at 300 K for CNT sheets [5] and yarns [6]. At 2 K and 10 K, the change in magnetoresistance after degassing was only an extra -0.5 %. The change was most significant above 3 T. This behaviour was observed for for all pristine yarns.

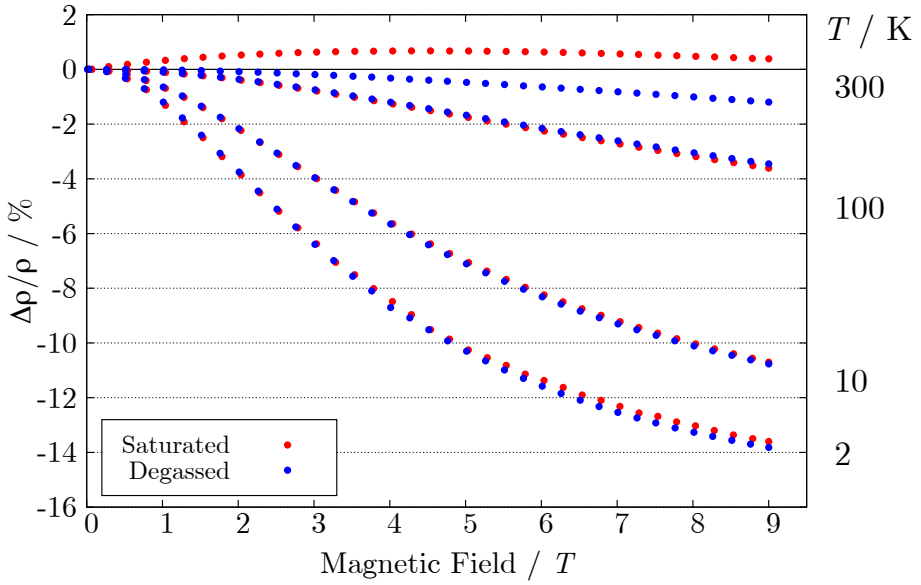


Figure 5.20: Magnetoresistance of a 50 $\mu$m pristine CNT yarn before and after degassing at $T = 390$ K in vacuum, with temperature indicated on the right.

Figure 5.21 shows the influence of degassing on 2700 °C annealed yarn. The magnitude of magnetoresistance increased with annealing temperature. This fits the trend that adsorbed gasses are more easily removed from the annealed samples.

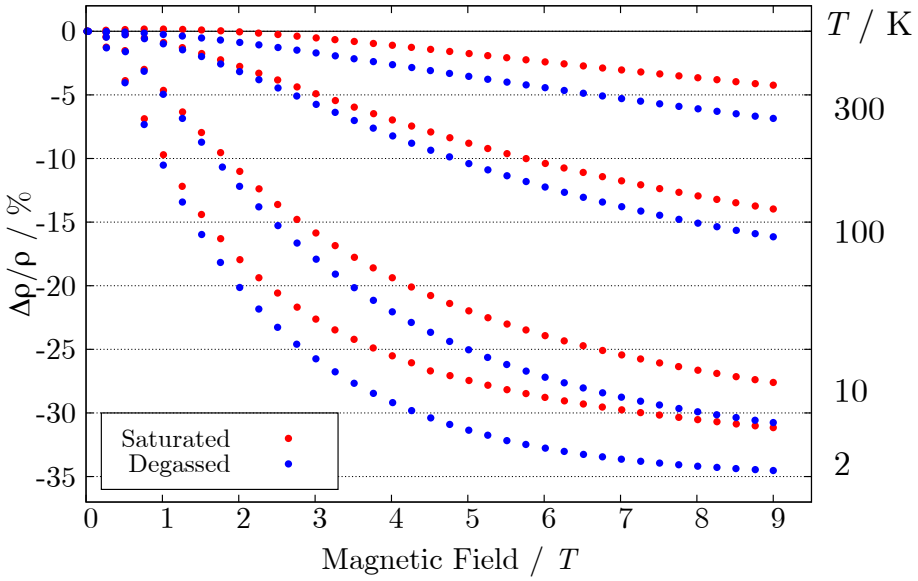


Figure 5.21: Magnetoresistance of a 50 $\mu$m annealed CNT yarn before and after degassing at $T = 390$ K in vacuum, with temperature indicated on the right.

Figure 5.22 shows magnetoresistance for three ~50 $\mu$m differently annealed yarns. At each temperature the annealed yarns had more negative magnetoresistance than the pristine yarn.

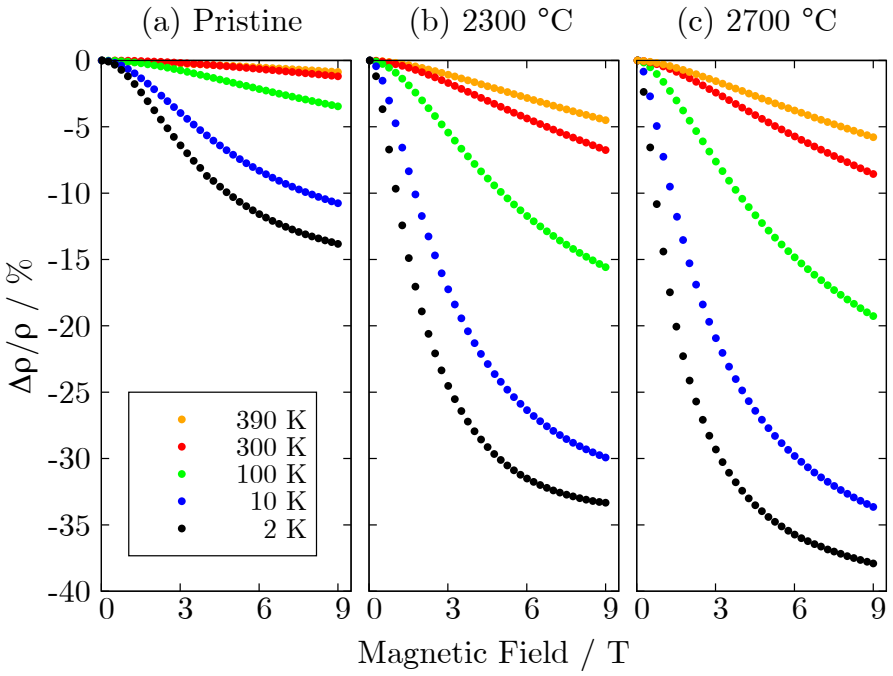


Figure 5.22: Magnetoresistance at from fields from 0 to 9 T and from $T = 2$ K to 390 K differently annealed ~50 $\mu$m CNT yarns, after degassing at 390 K.

The pristine yarn had a negative magnetoresistance of 13.8 % at 2 K, whereas the 2300 °C and 2700 °C annealed yarns had 2 K magnetoresistances of ∼33.3 % and ∼37.9 %, respectively. Each diameter yarn showed very similar temperature and field dependence, only varying by a few percent.

The increased negative resistance after annealing can be understood by considering the change in crystallinity of the CNTs after annealing. Kuznetsov *et al.* measured the magnetoresistance of annealed MWCNTs (∼20 nm diameter) and graphite, and showed that with increase annealing temperature the magnetoresistance of the CNTs approaches that of graphite [34]. Figure 5.23 shows the 300 K magnetoresistance of differently anneal 50 $\mu$m yarns, as well as the magnetoresistance of graphite measured by Kuznetsov *et al.* [84]. Figure 5.23 confirms that the magnetoresistance of the CNT yarns in this work approach that of graphite with increasing annealing temperature.

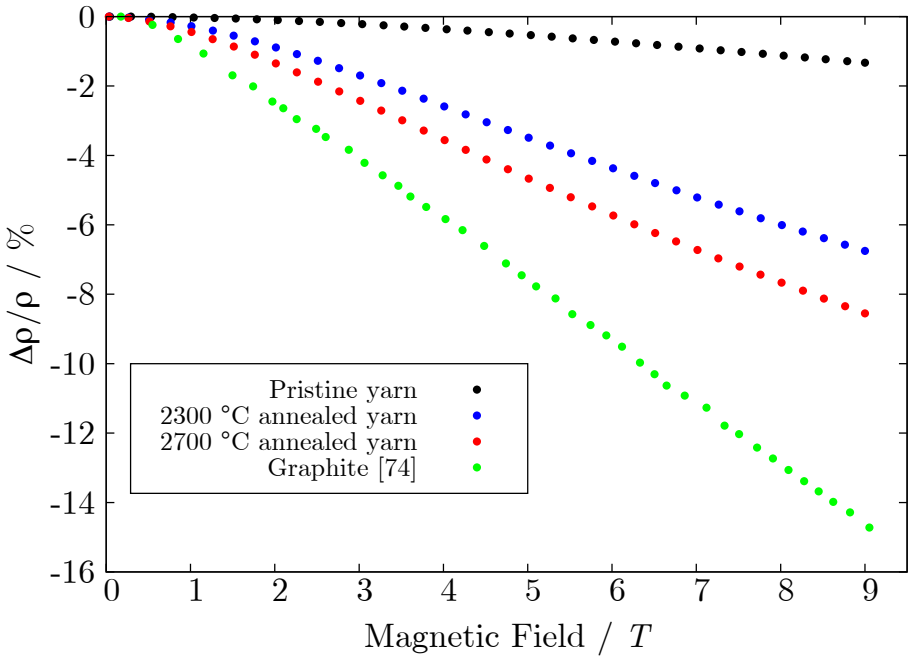


Figure 5.23: Magnetoresistance versus magnetic field at 300 K for differently annealed 50 $\mu$m CNT yarns and graphite. Graphite data taken from Ref. [84].

It is also likely that the removal of metallic nanoparticles after annealing reduced the amount of coherence-breaking electron scattering, as discussed in Section 2.2, thus

increasing the magnitude of negative magnetoresistance. However, the exact influence of the nanoparticles on magnetoresistance in CNT materials remains unclear.

Figure 5.24 shows the magnetoresistance versus temperature for the 45 $\mu$m annealed yarn after degassing at 390 K. Negative magnetoresistance was observed from 390 K to 2 K, decreasing monotonically to -35% at 2 K. This plot demonstrates the smoothness of the magnetoresistance with decreasing temperature for CNT yarns.

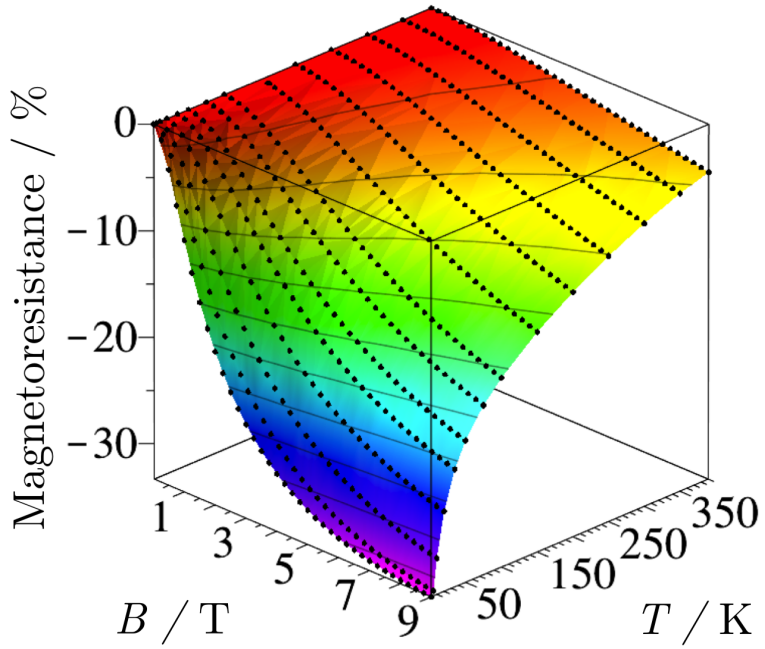


Figure 5.24: Magnetoresistance versus temperature for a 45 $\mu$m annealed CNT yarn degassed at $T = 390$ K. Negative magnetoresistance is observed for all $T$, increasing in magnitude as $T$ is decreased.

Several models have been suggested to explain the negative magnetoresistance observed in CNT materials, including a recent semi-empirical model used by Barzola-Quiquia *et al.* [85, 86]. Although the Barzola-Quiquia *et al.* model provides a qualitative fit to the magnetoresistance of the CNT yarns used in this work, the freedom of the four parameters makes useful explanation of the fit results difficult, as was noted by the authors [86]. Therefore, attempts to model the magnetoresistance of the CNT yarns will not be discussed.

## 5.5 Thermal Conductivity

The thermal conductance of each CNT yarn sample was measured from 50 to 300 K using the PTC method. An example of experimental thermal conductance values is shown in Figure 5.25. The measured conductances are on the order of 1 mW·K$^{-1}$ .

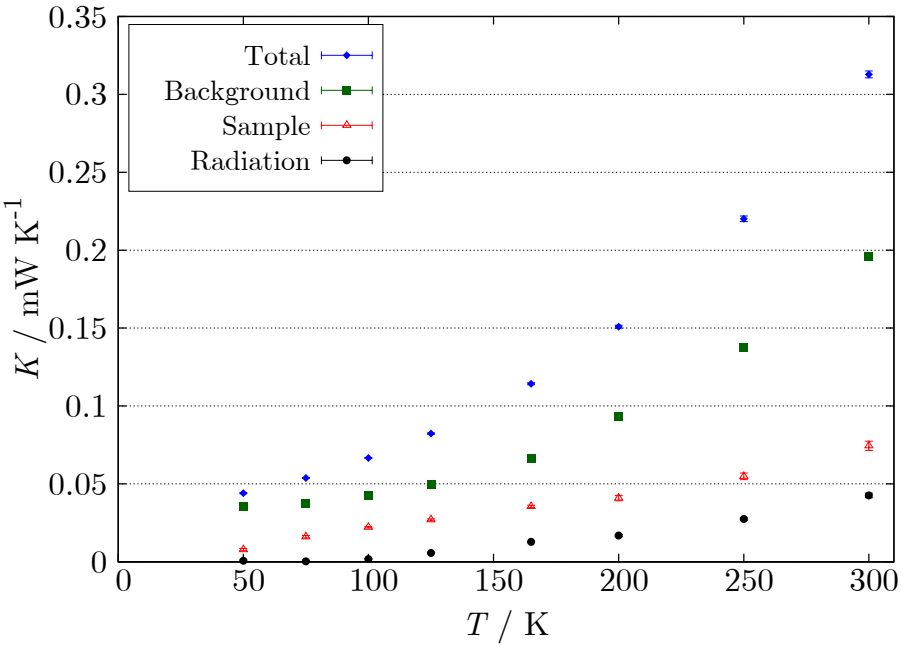


Figure 5.25: Thermal conductance breakdown for a 35 $\mu$m yarn, showing all of the conductance components shown in Equation 4.1. Many of the calculated error bars are too small to see.

The thermal conductivity, $\kappa$, of the sample can be calculated from the conductance using the length, $L$, and cross sectional area, $A$,

$$\kappa = \frac{1}{N}\left(K\frac{L}{A}\right). \tag{5.2}$$

where $N$ is the number of pieces of yarn being measured (∼15). The value of $L$ (∼7 mm) was taken to be the sum of the distances between the edges of the silver paste on either post for each section of yarn.

Below 50 K, the total thermal conductance began to converge with that background conductance (Figure 5.25), which lead to considerable uncertainty in the determination of sample conductance. The sample conductance was often less than 10% of the background conductance below 50 K, which is outside of the suggested limits of the PTC method [74]. Above 300 K, the $\kappa$ values often showed a large increase, likely because the radiation correction discussed in Section 4.4.1 becomes insufficient to compensate for radiative heat loss. These limitations mean that $\kappa(T)$ results are only presented for 50 K to 300 K.

Figure 5.26 shows thermal conductivity results for the CNT yarns as a function of temperature.

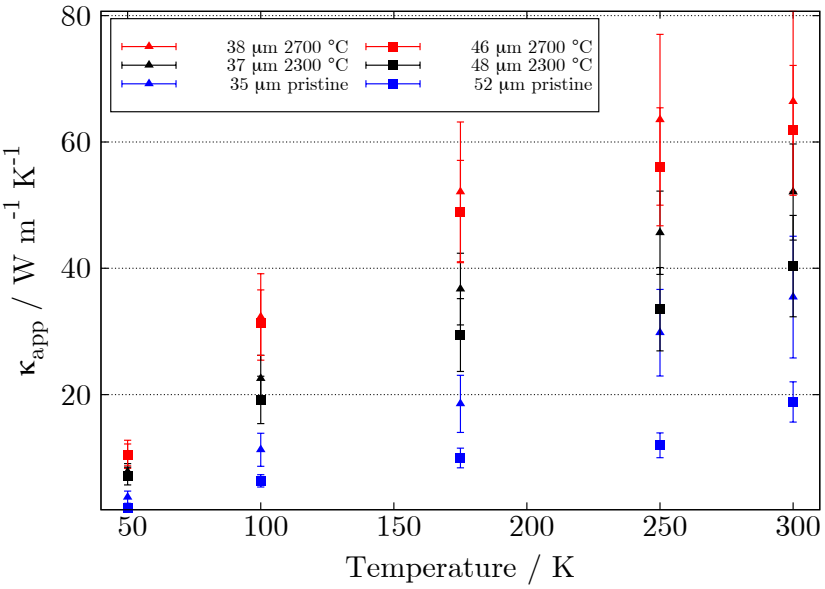


Figure 5.26: Thermal conductivity of ~35 $\mu$m and ~50 $\mu$m CNT yarn samples as a function of temperature. Thermal conductivity increased after high-temperature annealing.

As with electrical conductivity, the main source of uncertainty in the value of $\kappa$ is the yarn diameter. There is also uncertainty in the effective length of CNT being measured because of variation in the mounting method. Each piece of yarn was mounted separately, leading to slight variations in the distance between the silver

paste for each piece of yarn (typically less than 0.5 mm). Uncertainties in the measured values of $\Delta T$ and $P$ were negligible and therefore ignored. The uncertainty in $\kappa$ was calculated by propagating the uncertainty in the physical dimensions and the uncertainties in the linear fit of thermal conductance, and ranges from 10 to 25%.

The shape of $\kappa(T)$ for each material was similar to previously measured bulk CNT materials [5, 6] and individual MWCNTs [21]. As with electrical conductivity (5.12), the thermal conductivity of the CNT yarns was observed to decrease with increase yarn diameter because of the decrease in density.

The dominant phonon scattering mechanism in semiconducting MWCNTs is phonon-phonon scattering, as discussed in Section 2.3, and there the phonon mean free path has the largest affect on the temperature dependence of $\kappa$ [87]. Below 8 K, large $k$ phonons are not thermally excited, and no Umklapp scattering occurs. As temperature increases to 50 K, more inter-tube phonon modes (allowing conduction between adjacent concentric tubes of the MWCNTs) become active, and thermal conductivity becomes more three-dimensional, much like crystalline graphite [9]. From 50 K to 150 K, all of the interlayer phonon modes become active, and $\kappa(T) \propto T^2$. As temperature increases further, higher energy phonons become active, and Umpklapp scattering occurs. Above 300 K, $\kappa(T)$ likely would begin to peak, as observed previously in MWCNTs [21].

Each yarn shows increasing $\kappa$ with temperature, which means that the phonon transport is dominated by phonon boundary and defect scattering, not Umpklapp scattering [8]. Therefore, the improvement in $\kappa$ with annealing must be caused by reducing boundary, defect, impurity, and amorphous region scattering. Based on the Debye equation $\kappa = Cvl/3$ [8], increasing the phonon mean free path, $l$, would increase in $\kappa$. However, it is unclear to what extent the speed of sound, $v$, and heat capacity, $C$, of the CNT yarns are affected by high temperature annealing, and it is therefore not possible at present to quantitatively assess the increase in $l$.

The annealed yarns showed improved thermal conductivity relative to the pristine yarns of similar diameter. This result correlates with the Raman measurements, which showed that annealing graphitized amorphous carbon and improved the crystallinity of the CNT walls, thus increasing the phonon mean free path in the yarns.

Figure 5.27 shows the normalized thermal conductivities ($\kappa(T)/\kappa(300\ \mathrm{K})$) as a function of temperature for various CNT yarns. This figure shows that annealing increased the normalized conductivity between 250 K and 100 K relative to the pristine yarns. This result again suggests that the phonon mean free path was increased after high-temperature annealing.

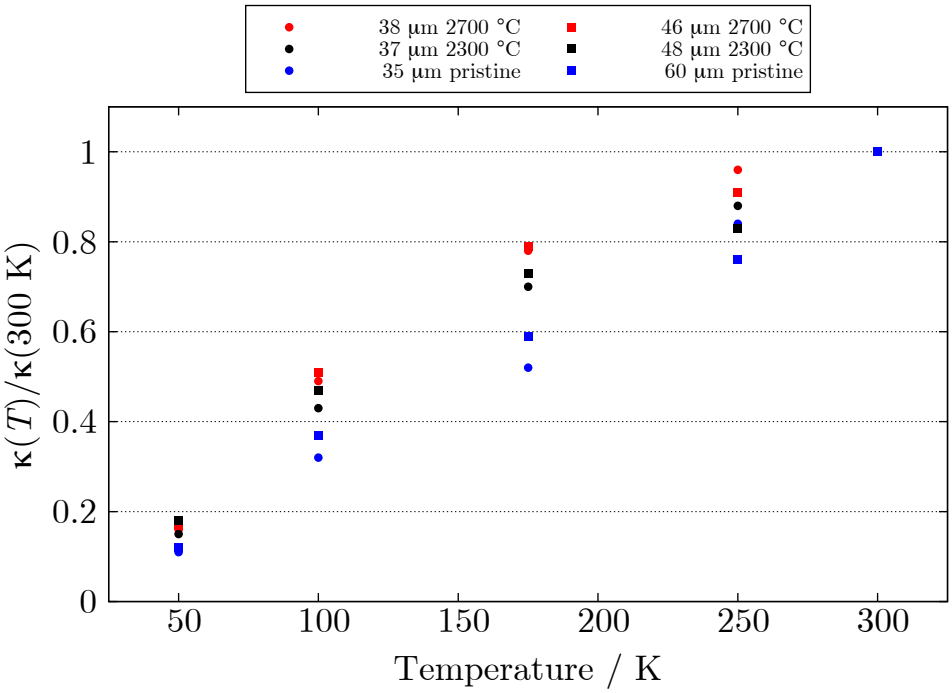


Figure 5.27: Normalized thermal conductivity as a function of temperature.

The room-temperature $\kappa$ values compare very well with previously reported results for pristine, dry-spun MWCNT yarns, as summarized in Table 5.2. The yarns used in this work were prepared in a very similar way to those in Ref. [6], in which the highest (then world record) thermal conductivity was 60 $\mathrm{W{\cdot}m^{-1}{\cdot}K^{-1}}$ for a 10 $\mu$m yarn. The 300 K thermal conductivities of CNT yarns are much higher than other

carbon fibre materials, such as Kevlar 49 ® (4 W·m$^{-1}$·K$^{-1}$ at 300 K [88]) or nylon (0.25 W·m$^{-1}$·K$^{-1}$ [89]).

Table 5.2: Room-temperature thermal conductivities of differently prepared CNT yarn materials.

| CNT yarn Sample | $\kappa_{app}$ (300 K) / W·m$^{-1}$·K$^{-1}$ | Measurement Type | Ref. |
|---|---|---|---|
| 10 $\mu$m array-spun | 60 ± 20 | PTC | [6] |
| 30 $\mu$m array-spun | 29 ± 4 | PTC | [6] |
| 12.5 $\mu$m array-spun | 40 | 3$\omega$ | [75] |
| 13.9 $\mu$m array-spun | 457 ± 71 | T-type | [76] |
| ∼90 $\mu$m acid-spun | 21 | Comparative | [37] |
| 9 $\mu$m acid-spun | 380 ± 15 | 3$\omega$ | [60] |
| 9 $\mu$m iodine doped | 635 | 3$\omega$ | [60] |
| 40 $\mu$m to 60 $\mu$m, pristine | 28±8 - 15±2 | PTC | this work |
| 37 $\mu$m to 48 $\mu$m, 2300 °C annealed | 52±8 - 41±8 | PTC | this work |
| 37 $\mu$m to 50 $\mu$m, 2700 °C annealed | 66±14 - 56±14 | PTC | this work |

The $T$ = 300 K thermal conductivity results for the differently annealed samples are summarized in Figure 5.28. There is clearly a trend of increased thermal conductivity after high-temperature annealing. Also, thermal conductivity decreased with increasing yarn diameter, as shown for electrical conductivity in Figure 5.13.

Figure 5.29 shows that the $T$ = 300 K thermal conductivity of several CNT yarns correlates with the Raman spectroscopy $I_G/I_D$ ratio. Thermal conductivity increased almost linearly with crystallinity, due to the increased phonon mean free path.

Since $\kappa$ measurements are very involved and time consuming, even in comparison to the $\sigma$ measurements, this result shows that Raman spectroscopy can be used to quickly assess the relative thermal conductivities of dry-spun CNT yarns, as has been proposed for electrical conductivity [57].

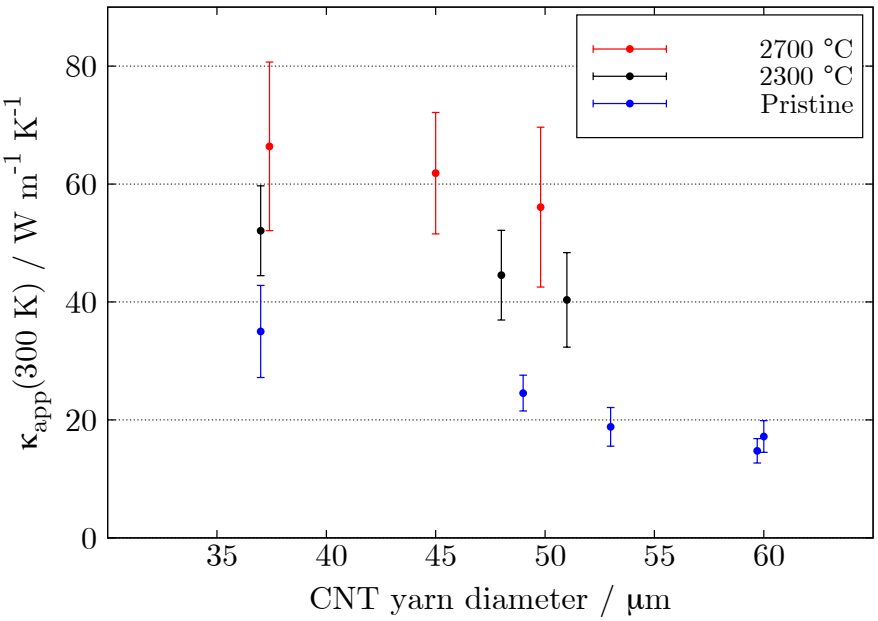


Figure 5.28: Room temperature thermal conductivity of differently annealed CNT yarn samples as a function of yarn diameter. The uncertainty in diameter is typically 2 $\mu$m. This plot shows qualitatively similar trend with diameter and annealing temperature to the $\sigma$(300 K) results, Figure 5.11.

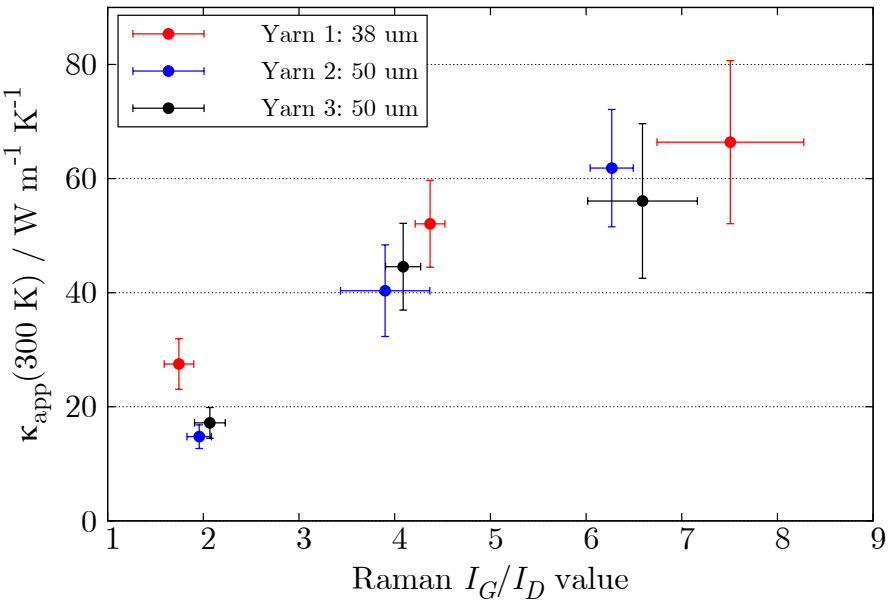


Figure 5.29: $T = 300$ K apparent thermal conductivity as a function of Raman $I_G/I_D$ ratio of three different CNT yarn samples. A nearly linear increase in $\kappa$ is observed with increasing annealing temperature.

### 5.5.1 Effective Lorenz Number

The effective Lorenz number, $L_{\text{eff}} = \kappa/\sigma T$, gives the relative contributions of electronic versus phononic thermal conductivity. For metals, electrons contribute significantly to $\kappa$, and the Lorenz number, $L_0 \approx 2.44 \times 10^{-8}$ W Ω K$^{-2}$ [8]. For CNT materials, $L_{\text{eff}}$ is typically two orders of magnitude higher than $L_0$ at all temperatures, indicating that thermal conductivity is always dominated by phonons [6, 9].

In this work, the thermal and electrical conductivities of CNT yarn samples were measured, and therefore the $L_{\text{eff}}$ can be calculated as a function of temperature. It should be noted $\sigma$ and $\kappa$ measurements were made on similar, but not identical sections of yarn. However, for each sample discussed here, the diameters of the yarns used for $\kappa$ and $\sigma$ measurements were similar, allowing for $L_{\text{eff}}$ to be estimated.

Figure 5.30 shows the calculated value of $L_{\text{eff}}$ for a 50 $\mu$m pristine CNT yarn from 25 K to 300 K, as well as for a CNT array [4] and CNT sheet [5]. It should be noted that the values of $\sigma$ used to calculate $L_{\text{eff}}$ in Figure 5.30 were without degassing in vacuum, to compare with the $\sigma$ measurements in Refs. [4] and [5] which were made without degassing.

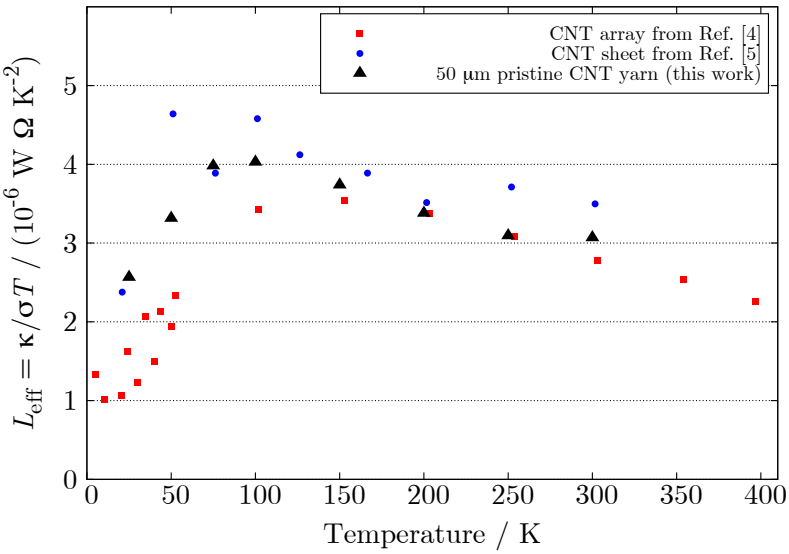


Figure 5.30: Effective Lorenz number, $L_{\text{eff}} = \kappa/\sigma T$, for several CNT materials, including a 50 $\mu$m pristine CNT yarn from the present work [4, 5].

The magnitude of $\kappa/\sigma T$ for this pristine yarn is two orders of magnitude higher than $L_0$, suggesting that $\kappa$ is dominated by phonons in this yarn, as with other CNT materials [4, 5]. All of these CNT materials show a broad peak between 50 K and 100 K, indicating a maximum in the phononic contribution to thermal conductivity in this temperature range. The fact that this peak is observed for each material suggests that the phenomenon is likely an inherent property of the CNTs, and independent of the bulk geometry.

Annealing the CNT yarns has a large affect on the magnitude of $\kappa/\sigma T$, as shown in Figure 5.31. In this plot $L_{\text{eff}}$ was calculated using both oxygen/$H_2O$ saturated and degassed values of $\sigma$, but saturated values of $\kappa$. The PTC stage used in this work is not capable of being heated to 390 K for degassing because of the cellulose acetate strip, and therefore $\kappa$ measurements were made without degassing.

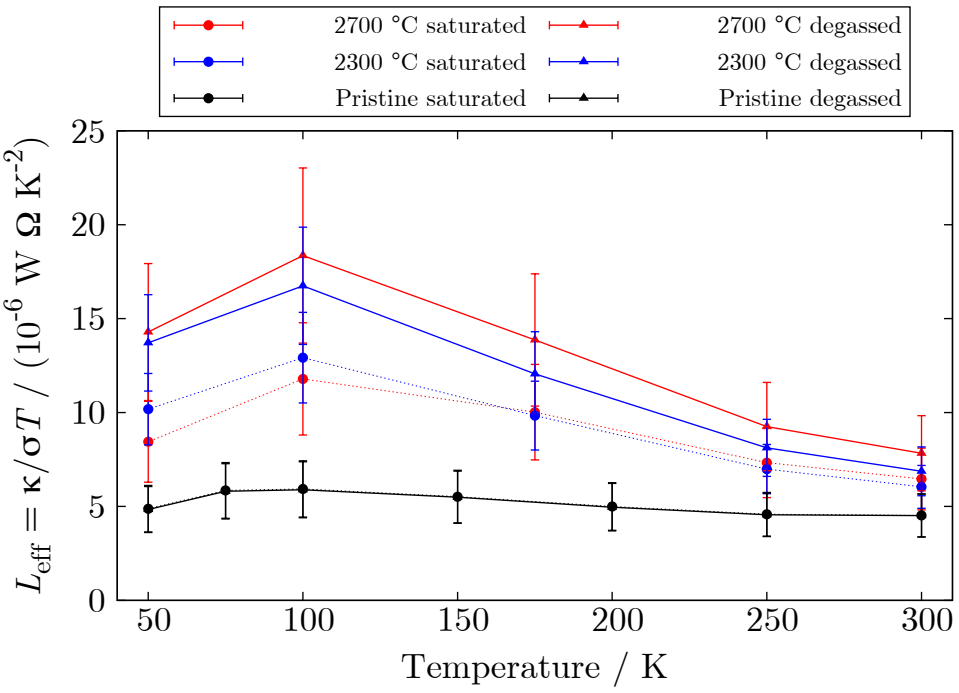


Figure 5.31: Effective Lorenz number, $L_{\text{eff}}$, as a function of temperature for differently annealed ~50 $\mu$m CNT yarns before and after degassing in vacuum. Annealing causes an increase in the peak near 100 K. Lines are included as a guide to the eye. Note that the pristine saturated and degassed data lie on top of each other.

At each temperature the value of $\kappa/\sigma T$ increased significantly after annealing, implying that annealing causes a more substantial increase to $\kappa$ than $\sigma$ at all temperatures. This behaviour was also observed for the 35 $\mu$m yarns. Improving the CNT crystallinity likely has a larger impact on the phonon mean free path than on the electron mean free path. The increase in $L_{\text{eff}}$ was especially apparent in the range of the peak. Since phonon conduction was observed to dominate in this temperatures range, increasing the CNT crystallinity would clearly increase the phonon contribution, and thus increase the peak.

After degassing, $L_{\text{eff}}$ increased for the annealed samples because degassing decreases $\sigma$ (increases $R$), as shown in Figure 5.8. The pristine samples (Figure 5.7) do not show significant degassing at 390 K, and therefore show little change in $L_{\text{eff}}$.

# Chapter 6

# Other Systems Investigated

## 6.1 Reactor-Spun CNT Fibres

The thermal conductivities of small diameter ($\sim$10 $\mu$m) CNT fibres from Prof. Alan Windle's group at the University of Cambridge were studied using the PTC method, as discussed in Section 4.6. These CNT fibres were spun directly from a floating catalyst CVD reactor, shown schematically in Figure 6.1, in a method similar to that discussed in Ref. [90]. The reactor-spinning technique has some advantages over dry-spinning and liquid-spinning, including the reduction in the number of steps required to produce CNT fibres, producing fibres with low wall-number CNTs, and the possibility of using longer CNTs, which would be advantageous for transport and mechanical properties [90].

In the floating catalyst CVD method, ferrocene ($Fe(C_5H_5)_2$) and thiophene ($C_4H_4S$) were decomposed to form Fe/S catalyst particles. The carbon precursor gas (either methane or toluene) was then added at 1290 °C, and CNTs were grown on the catalyst particles. The CNTs eventually reached a spatial density at which they formed an aerogel that could be mechanically removed from the reactor. As the fibre was removed it was condensed by collection onto two rotational winders, as shown in Figure 6.1. The efficiency of carbon precursor converted to CNT fibre is on the order of 2 %, and roughly 50 % of the iron from the ferrocene precursor is thought to remain in the fibre [91].

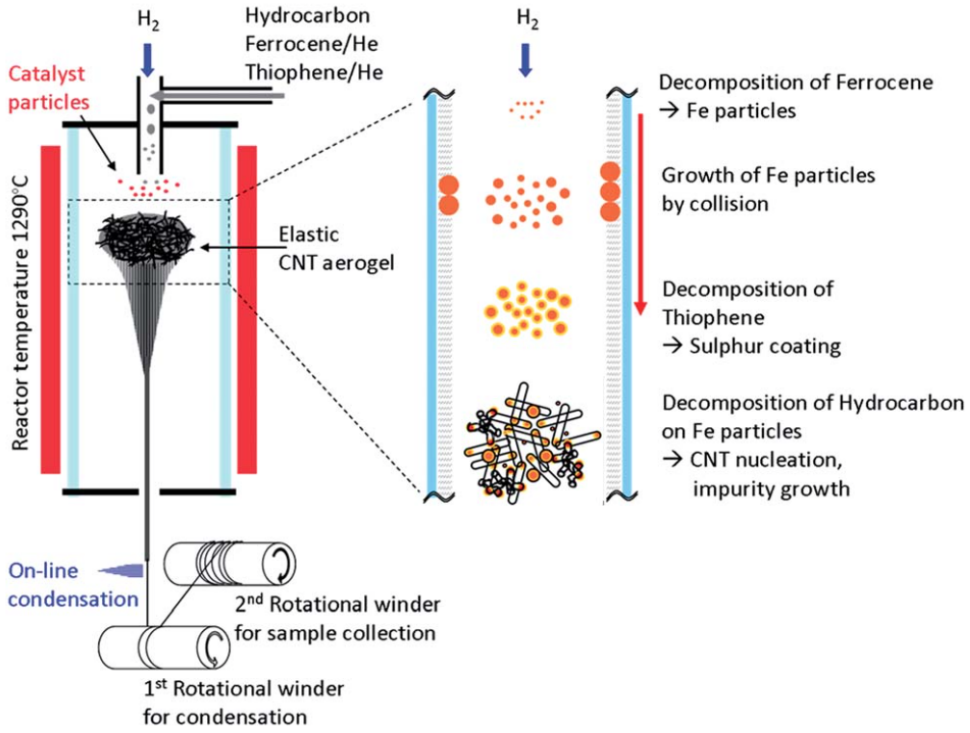


Figure 6.1: Schematic of the floating catalyst CVD method used to produce direct-spun CNT fibres. Reproduced from Ref. [90] with permission from The Royal Society of Chemistry.

The diameters and lengths of the CNTs in each fibre are on the order of 0.9 to 1.5 nm and 100 $\mu$m, respectively [91]. The CNTs in the Type A fibre are a mix of SWCNT and MWCNT (up to 15 walls), whereas the Type B fibre is thought to be composed mainly of SWCNTs [91]. The dimensions of the fibres are shown in Table 6.1, including the linear mass density in tex (the mass of fibre in grams per 1000 m). The Type A fibres had a mediocre strength of 0.6 to 1 N·tex$^{-1}$ while the Type B fibres were much stronger, $\sim$2 N·tex$^{-1}$, similar to the strength of Kevlar® 49 [91].

Table 6.1: Summary of the physical dimensions and precursor carbon sources for two CNT fibres, Type A (methane) and Type B (toluene).

| CNT yarn sample | Average diameter / $\mu$m | Linear density / tex | Density / g·cm$^{-3}$ |
|---|---|---|---|
| Type A: methane | 8.1 | 0.026 | 0.505 |
| Type B: toluene | 7.4 | 0.023 | 0.535 |

An SEM micrograph of the Type B yarn is shown in Figure 6.2. The cross section of this fibre is clearly not homogeneous. This is because when the fibre was pulled from the reactor, it often condensed into an oval or flattened shape [91]. However, the measured linear densities of the yarns were consistent through the spinning process, suggesting that changes to the cross-sectional structure of the yarns are only a geometrical effect.

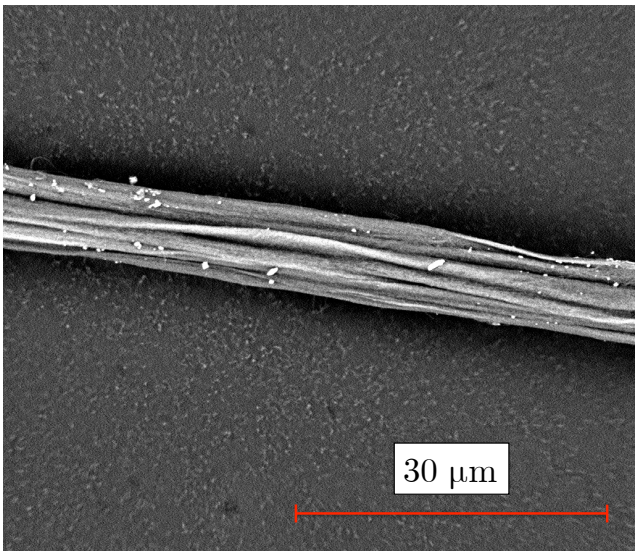


Figure 6.2: SEM micrograph of a Type B SWCNT yarn.

The thermal conductivities of the Type A and Type B yarns were measured using the parallel thermal conductance method. As with the MWCNT yarns discussed previously, the cross-sectional area of these yarns were calculated from the outer dimensions, as measured using SEM. Therefore, the presented values of $\kappa$ are "apparent" values, as discussed in Section 3.2.3.

Figure 6.3 shows the calculated apparent thermal conductivities of the Type A and Type B fibres from $T = 100$ K to 325 K. For these small diameter yarns, radiation at higher temperatures was less than the larger yarns discussed in Section 5.5. Because of their small diameter, the samples were attached to the PTC stage by continuously winding the fibres between the two platforms, instead of cutting the fibres into small

segments. The sample conductances of these small diameter CNT fibres were only 30 % of the typical conductances measured for the 35 $\mu$m to 60 $\mu$m CNT yarns discussed is Section 5.5, which made measurements of $\kappa$ below 100 K impossible.

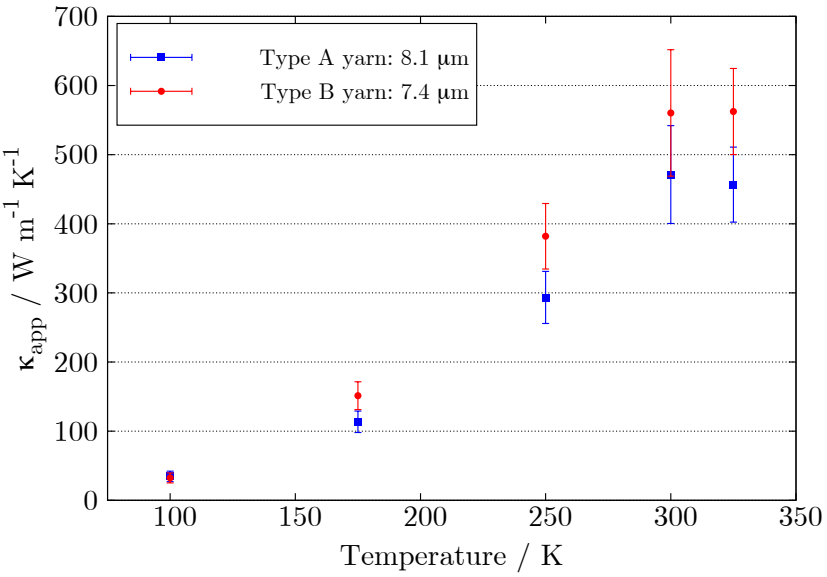


Figure 6.3: Apparent thermal conductivity of two reactor-spun CNT fibres. The precursor gases used to grow the Type A and Type B fibres were methane and toluene, respectively.

The 300 K thermal conductivities of the Type A and Type B fibres were 460 $\pm$ 50 W·m$^{-1}$·K$^{-1}$ and 560 $\pm$ 60 W·m$^{-1}$·K$^{-1}$, respectively. These conductivities are the highest reported values to date for pristine CNT fibres, with the previous highest being 456 W·m$^{-1}$·K$^{-1}$ for a 12.2 $\mu$m dry-spun CNT yarn [76]. Both fibres show evidence of a broad peak in $\kappa(T)$ near 300 K, as has been observed previously in individual SWCNTs [2] and some MWCNTs [87].

Figure 6.3 shows that the Type B (toluene precursor) fibre had a thermal conductivity 90 W·m$^{-1}$·K$^{-1}$ (20 %) higher at 300 K than the Type A (methane precursor) fibre. This result in good agreement with previously measured differences in the mechanical and electrical properties of these two fibres, which have shown the Type B fibres to be superior [91].

## 6.2 Boron Nitride Nanotube Materials

The thermal conductivities of several boron nitride nanotube materials were measured using the PTC method. The materials were provided by the National Research Council of Canada Emerging Technologies Division.

H-BN is isostructural to graphite, and much as "rolling" graphene can form a carbon nanotube, BNNTs can be formed from rolling monolayer h-BN [92]. BNNTs are isostructural to CNTs, with nitrogen and boron atoms alternately replacing carbon atoms at close to a 1:1 ratio [93]. BNNTs were first synthesized in 1995, shortly after the CNT structure was first identified [94].

BNNTs can be single-walled, but are usually multi-walled because the partially ionic nature of the B-N bond increases the interaction between adjacent layers and stabilizes the formation of multi-walled BNNTs [92]. These interactions also limit rotational freedom between walls, and make it more likely for there to be a correlated stacking order between walls, which is not observed in CNTs.

As with CNTs, individual BNNTs have many desirable physical properties, including high thermal conductivity [95] and mechanical strength [96] equal to or greater than CNTs, while being electrically insulating [97, 98] and more thermally and chemically stable [99]. This combination of properties makes BNNTs more suitable than CNTs for some applications, such as a composite filler that must be electrically insulating but thermally conductive, or for use at high temperatures or in hazardous environments [92].

BNNTs have a bandgap of 5.5 eV, essentially independent of tube diameter or chirality [92], unlike CNTs which change bandgap from metallic to semiconducting depending on chirality and diameter. Because of this large bandgap, pristine BNNTs are white, which could be advantageous over black CNTs for certain applications.

Simulations have predicted that the thermal conductivity of BNNTs could be equal to that of SWCNTs [95]. However, only a limited number of thermal conductivity reports exist on BNNTs and BNNT materials. The highest thermal conductivities of a BNNT material measured to date were 325 $W \cdot m^{-1} \cdot K^{-1}$ at 300 K for isotopically pure $^{11}$BNNTs, and 200 $W \cdot m^{-1} \cdot K^{-1}$ for natural-abundance BNNTs [100].

Despite these exciting potential applications, fundamental research concerning BNNTs and development of bulk BNNT materials has significantly lagged behind that of CNTs, mainly because of the difficulty in producing useable quantities of high-quality BNNTs, as will be discussed below.

### 6.2.1 Synthesis

The majority of BNNT synthesis methods used to date have been based on methods which are successful for CNT production, including CVD [101], ball-milling [102], arc discharge [103], pyrolysis [104], arc-jet plasma [105], and laser ablation [106]. The BNNT yield from most of these synthesis methods is typically on the order of grams per hour. Of this yield, most of the BNNTs are short, large diameter, large wall-number, and low-quality [92].

Recently, major advances in the production of high quality BNNTs have been made at the National Research Council Canada using a hydrogen-catalyzed induction thermal plasma technique [107]. This technique continuously produces small diameter, high purity BNNTs at a rate of 20 g/hr, with ∼200 g produced in a single run. The overall conversion efficiency of the BN feedstock to BNNTs is 30-35% [107].

For the materials studied in this work, the induction thermal plasma technique used a feedstock h-BN power with nitrogen and hydrogen gases injected into a high-temperature plasma (>8000 K) [107]. The h-BN feedstock is only stable to 3500 K, and was therefore vaporized by the plasma within milliseconds, decomposing into a plasma of B, N, and H. As the plasma entered the reactor, it cooled at a rate of

$\sim 10^5$ K/s, and formed nano-scale boron droplets. Nitrogen-containing gas species (polyborazylene, ammonia boron, etc.) reacted with the B droplets, which nucleated BNNTs on the droplet surface. As the droplets moved through the reactor, more nitrogen was incorporated onto the droplet surfaces, and BNNTs grew by the root-growth mechanism. This growth continued until the droplet fell below the critical reaction temperature ($>$ 2300 K, the B-N solid-liquid transition temperature), or until the droplet became encapsulated by h-BN. This root growth mechanism has been confirmed by TEM [107].

The majority of BNNTs produced by the thermal plasma technique have a low number of walls (2 to 5) and appear to be highly crystalline. TEM micrographs of of BNNTs with different wall number produced by the thermal plasma technique are shown in Figure 6.4

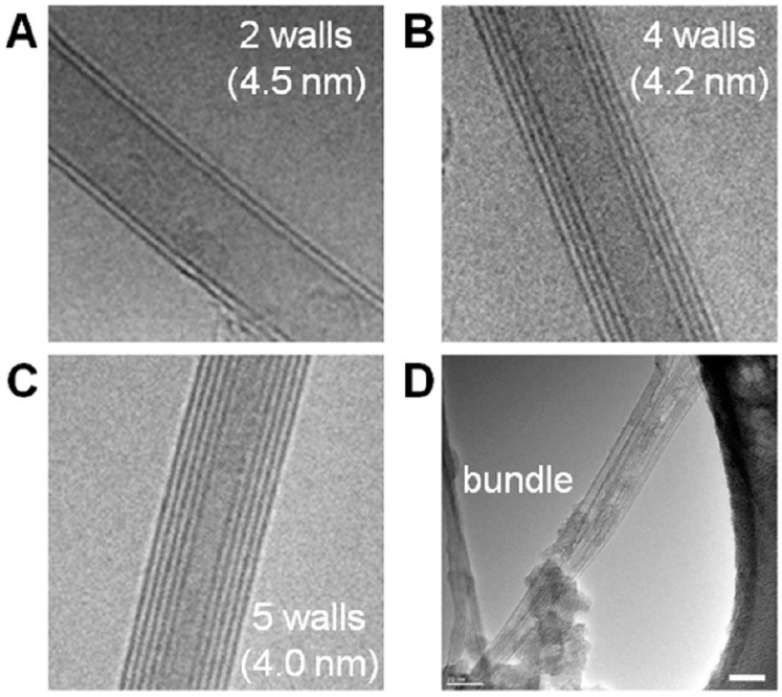


Figure 6.4: SEM micrographs of small diameter BNNTs produced by plasma synthesis. Reprinted with permission from Ref. [107]. Copyright (2014) by the American Chemical Society.

The yield from a typical synthesis run (∼200 g) is shown in Figures 6.5 (a) and (b). The as-produced BNNTs were deposited on the sides of the reactor, and had a beige appearance because of the presence of amorphous boron. The amorphous boron was removed by thermal oxidation in air (425 °C for three days) to produce $B_2O_3$, which was then removed using methanol or water [107].

### 6.2.2 BNNT Materials

As with carbon nanotubes, bulk BNNT materials such as yarns, sheets, and bucky-papers, are required to fully utilize the properties of BNNTs. Producing bulk BNNT materials has been difficult to date because of the very small quantities of high quality BNNTs available. This has limited bulk BNNT materials to rudimentary yarns [108], sheets [109], and BNNT/epoxy composites [110].

The induction plasma synthesis method discussed above is advantageous because it is capable of producing several different bulk morphologies depending on where the BNNTs are deposited within the reactor, seen in Figure 6.5 [107]. The bulk morphologies typically produced are: dense entangled fibrils (Figure 6.5 (c)); cloth-like layered sheets (Figure 6.5 (d)); and low density cotton-like deposits (Figure 6.5 (e)). These bulk BNNT structures were formed by gas-flow driven segregation of the BNNTs during the reaction process. The structure and properties of the individual BNNTs in each material are identical, only the mesoscopic and macroscopic morphologies are different, as seen in Figure 6.6.

The dense fibrils were made of micrometer-sized strands, which have rough alignment along the fibril axis. Hand-spun yarns over 20 cm in length can be produced from these fibrils. This rudimentary yarn has a Young's modulus of 0.5 GPa and a tensile strength of 10 MPa [107]. It is also possible that this method could be modified to produce continuously spun yarns directly from the reactor, as has been done with CNTs [40].

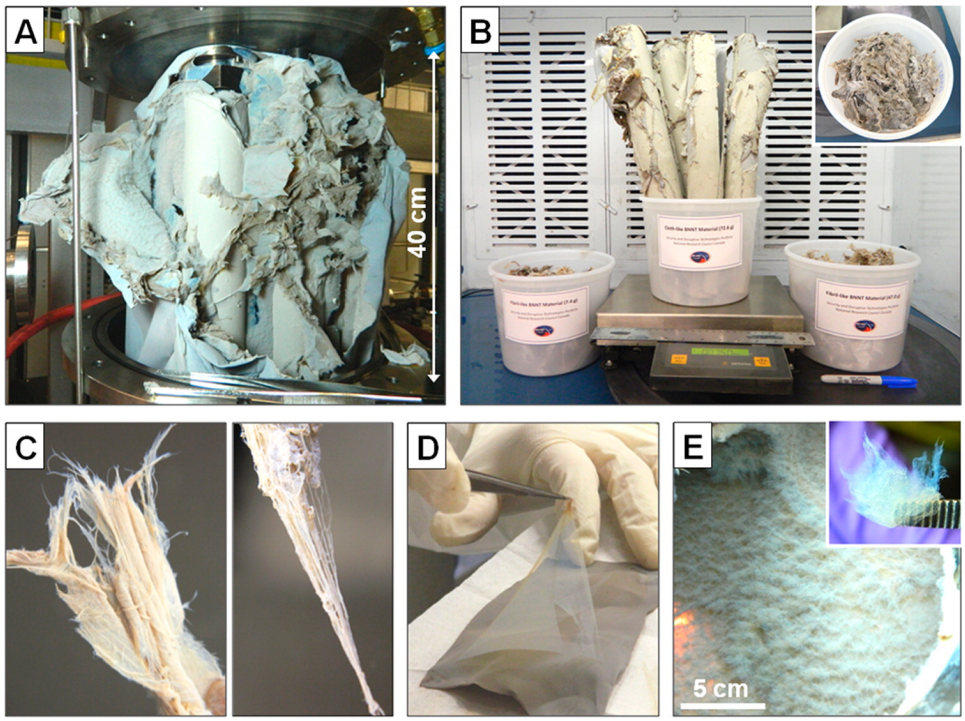


Figure 6.5: Different BNNT morphologies produced by the induction thermal plasma synthesis method. (A) and (B) ∼200 g of BNNTs produced during an 11 hour synthesis run (C) dense BNNT fibrils (D) multi-layered BNNT sheets showing a single layer being removed (E) a low density BNNT deposit. Reprinted with permission from Ref. [107]. Copyright (2014) by the American Chemical Society.

The cloth-like BNNTs were deposited as ∼20×50 $cm^2$ sheets that were on the order of millimetres thick. The APs consisted of multiple layers that can be easily separated. Two AP sheets were studied in this work, referred to as AP1 and AP2, and were produced by the thermal plasma method using slightly different synthesis conditions. The density of the AP sheets were ∼ 0.15 $g/cm^3$.

Bulk BN nanotube materials can also be processed from solution to create non-woven, unaligned sheets up to 30×30 nm in area, known as BPs [107, 111]. Similar materials have been produced previously using CNTs [112, 113]. The BNNT BPs were produced by dispersion of randomly oriented purified BNNTs produced by the thermal plasma synthesis method in methanol, followed by vacuum filtration [107]. The resulting BPs are flexible, ∼ 15 to 150 $\mu$m thick, and have densities of ∼ 0.45

g/cm$^3$. Preliminary mechanical measurements have shown a Young's modulus of 0.3 GPa and tensile strength of 1.5 MPa [107].

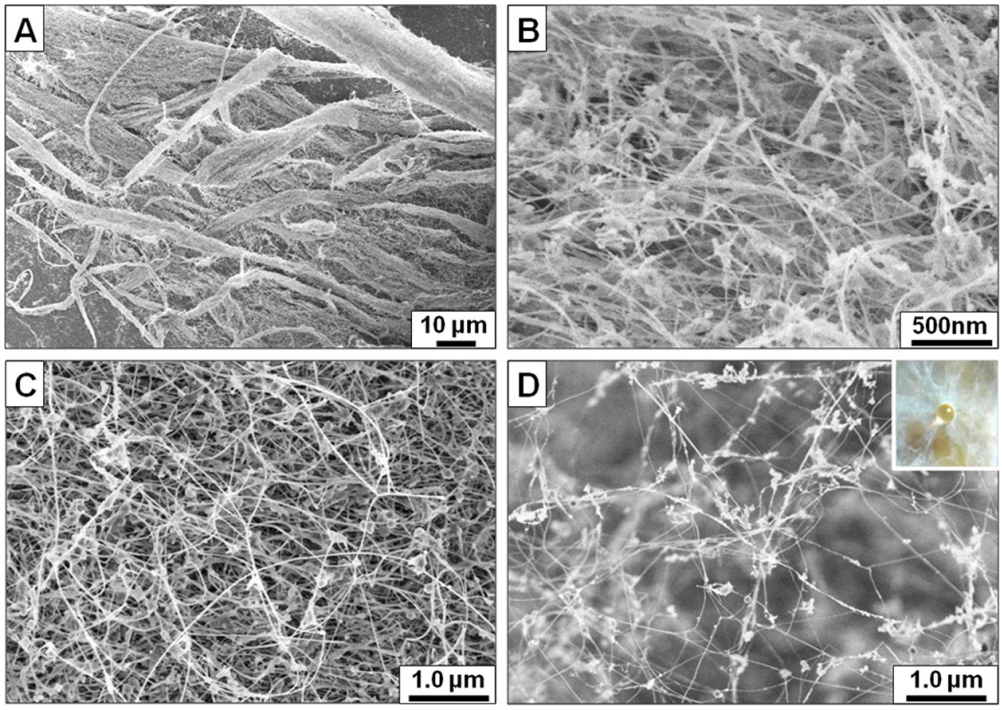


Figure 6.6: SEM micrographs of BNNT materials produced by plasma synthesis showing different morphologies: (A) and (B) dense fibrils showing rough alignment (C) randomly oriented sheet-like material (D) a low-density BNNT deposit. Reprinted with permission from Ref. [107]. Copyright (2014) by the American Chemical Society.

BNNT/polymer composites were prepared by impregnating the BNNT BPs with two different epoxies, as discussed in detail in Ref. [111]. The resulting composites were ∼30 wt. % BNNT, and were higher density than the pristine BPs. The composites were cut into 1 mm × 3 mm sections to be mounted on the PTC stage.

### 6.2.3 Results and Discussion

The apparent thermal conductivities of the AP1 sheet and 100 $\mu$m thick BP were measured from $T$ = 50 K to 300 K using the PTC method are shown in Figure 6.7. The AP1 sheet and BP show 300 K conductivity values of 1.3 ± 0.2 W·m$^{-1}$·K$^{-1}$ and 0.5 ± 0.1 W·m$^{-1}$·K$^{-1}$, respectively.

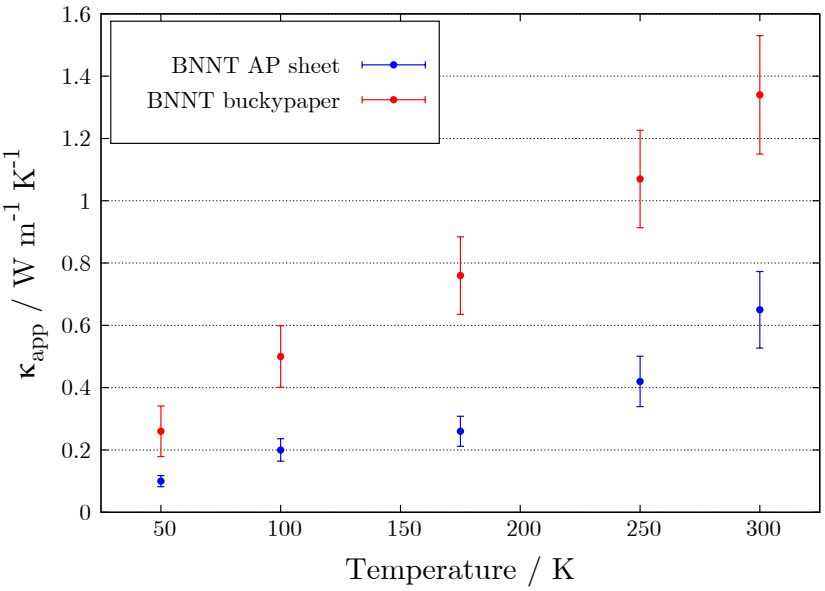


Figure 6.7: Thermal conductivity of two BNNT materials: (blue) as-prepared BNNT sheet and (red) vacuum filtered BNNT buckypaper.

These values are two orders of magnitude lower than the experimental thermal conductivities of individual BNNTs ($\sim$ 300 W·m$^{-1}$·K$^{-1}$) [100], but compare well with previous measurements of similar BNNT and CNT materials [5, 114]. As with all bulk materials based on nanotubes, the measured thermal conductivity is much lower than the values of individual nanotubes because of the decreased density, misalignment, and thermal resistance between individual tubes [5, 6]. The thermal conductivity of the BP is higher than that of the AP sheet in large part because of the $\sim$3 times difference in density.

Figure 6.8 shows a summary of the $\kappa$(300 K) results for the various BNNT materials measured. All of the results are very self-consistent. The AP1 and AP2 sheets show no significant difference in thermal conductivity, suggesting that the two synthesis methods produced similar BNNTs. Composite 1 shows slightly higher conductivity (2.7 $\pm$ 0.3 W·m$^{-1}$·K$^{-1}$) than Composite 2 (2.2 $\pm$ 0.2 W·m$^{-1}$·K$^{-1}$). The slight discrepancy between the two measured conductivities for Composite 1 are likely due to imperfect cutting of the edges in the composite sample, which lowered $\kappa$.

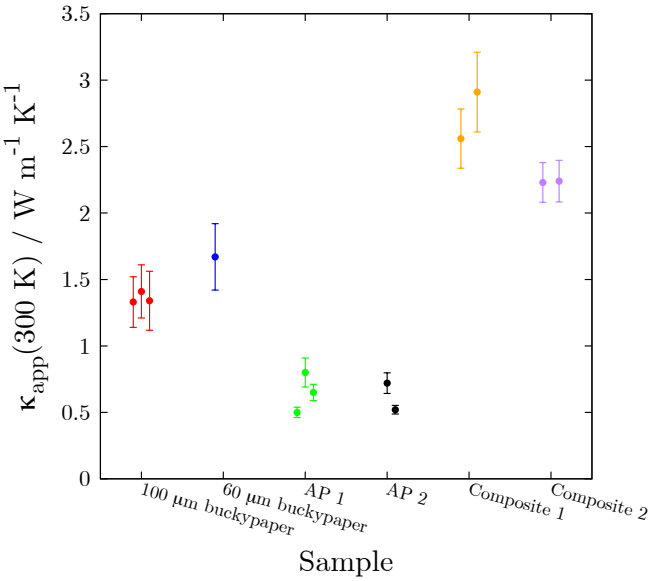


Figure 6.8: Apparent thermal conductivities of various BNNT sheet and buckypaper materials as determined using the parallel thermal conductance method.

The difference in thermal conductivity between the buckypapers and sheets is mostly due to the $\sim 3$ times density difference. Figure 6.9 shows the density-corrected $T = 300$ K thermal conductivities $(\kappa/\rho)$ of the two materials, which show much better agreement than the results shown in Figure 6.8. This suggests that the thermal conductivity of the individual BNNTs in the AP sheet and BP are likely very similar.

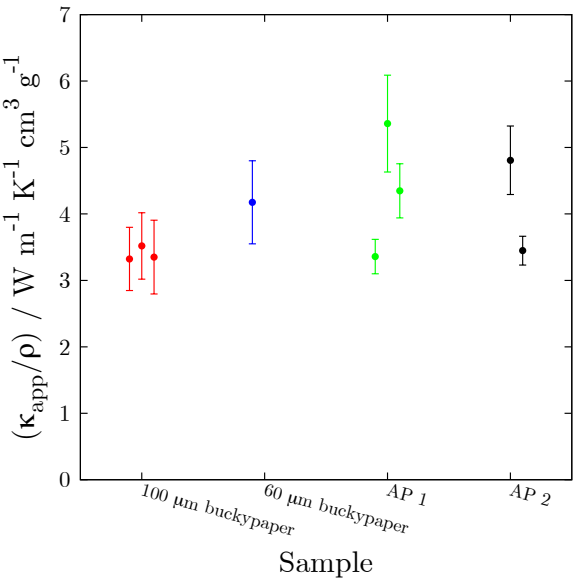


Figure 6.9: Density normalized apparent thermal conductivities of various BNNT sheet and buckypaper materials.

The values of $\kappa$ measured in this work compare well with previously measured thermal conductivities of BNNT and CNT materials, as shown in Table 6.2. Although the thermal conductivities of these materials are low in comparison to denser and more aligned nanotube materials, they could still be thermally conductive enough for some applications, such as an electrically insulating but thermally conductive packaging or substrate material.

Table 6.2: Summary of $T = 300$ K apparent thermal conductivity results for several BNNT materials and composites.

| Sample | $\kappa_{app}$ (300 K) / $W \cdot m^{-1} \cdot K^{-1}$ | Ref. |
|---|---|---|
| CNT sheet | 2.54 ± 0.48 | [5] |
| BNNT mat | 2 | [114] |
| BCN nanotube mat | 4 | [114] |
| Isotopically pure individual $^{11}$BNNT | 325 | [100] |
| BNNT/PVA composite | 0.54 | [110] |
| Pristine BNNT sheet | 0.50 - 0.8 | this work |
| BNNT buckypaper | 1.33 - 1.67 | this work |
| BNNT/polymer composites | 2.2 - 2.9 | this work |

# Chapter 7

# Conclusions

There is a large range of data (quality and quantity) in the literature for the thermal and electrical conductivities of bulk carbon nanotube materials because of the differences in synthesis and measurement techniques. This fact has made it difficult to understand how the synthesis techniques, nanotube properties, and bulk morphologies impact the properties of the resulting materials. A major goal of this work was to isolate the influence of one parameter, namely high-temperature annealing, to study how it influences the physical properties of dry-spun CNT yarns.

Carbon nanotube arrays were synthesized using chemical vapour deposition, and CNT yarns with diameters between 35 and 60 $\mu$m were spun from the CNT arrays using a semi-automated technique. The yarns were then annealed up to 2700 °C in argon atmosphere. The influence of annealing on the crystallinity and thermal and electrical properties of the yarns were then measured using a variety of techniques.

Raman spectroscopy was performed to characterize the relative quality of the CNTs in the yarns before and after annealing. The ratio of intensities of the Raman D-peak (associated with defects) and G-peak (associated with graphitic planes) was used to compare the relative crystallinity of the samples. The value of $I_G/I_D$ was found to increase monotonically with annealing temperature, from an average of 1.5 for the pristine yarns up to $\sim 7$ after annealing at 2700 °C, impling that high-temperature annealing greatly improved the crystallinity of the CNT yarns. Also, the broad amorphous carbon peak observed for the pristine yarns decreased after annealing due to the removal of amorphous carbon leftover from the synthesis process. The

improvement in crystallinity and removal of amorphous carbon are both important steps in optimizing the transport properties of CNT materials.

Electrical properties, including electrical conductivity, $IV$-curves, and magnetoresistance, were measured from 2 to 390 K in vacuum using a Physical Properties Measurement System. It was observed that the electronic properties of these CNT yarns are extremely sensitive to adsorbed species, including oxygen and water, as was demonstrated recently [52]. The presence of adsorbed species is not often discussed in the literature, and could contribute to the discrepancy between reported electrical properties of CNT materials. Degassing at 390 K under vacuum ($10^{-4}$ Torr) was observed to cause an increase in electrical resistance of $\sim$10 % for the pristine yarns and $\sim$25 % for the annealing yarns. It is possible that degassing at 390 K is not sufficient to remove the adsorbed species from the pristine yarns, since gases are more tightly bonded to CNT defects [52].

Electrical conductivities of the pristine yarns decreased with increasing yarn diameter, $d$, from 160 $\pm$ 10 S·cm$^{-1}$ for the 35 $\mu$m yarn to $\sim$100 $\pm$ 6 S·cm$^{-1}$ for the 60 $\mu$m yarn. This trend has been observed previously, and is likely due to the decrease in yarn density with increasing diameter [6]. The values of $\sigma$ fit well to a $d^{-1}$ trend with data from similarly prepared yarns [44].

Electrical conductivity was improved after annealing for each CNT yarn. For the 2300 °C and 2700 °C samples, conductivity increased $\sim$40 % and $\sim$100 %, respectively, for both the 35 $\mu$m and 50 $\mu$m yarns. The highest measured electrical conductivity was 310 $\pm$ 25 S·cm$^{-1}$ for a 37 $\mu$m yarn annealed at 2700 °C. This improvement was due to the improved crystallinity of the CNTs in the yarns, which increased the electron mean free path. The semiconducting temperature dependence of the yarns also increased after annealing. The electrical conductivity as a function of temperature was found to fit well to a model combining variable-range hopping and fluctuation-assisted tunneling [82].

The $IV$-curves of the yarns were found to become non-linear below 10 K, as has been observed previously for CNT materials [6, 5]. Joule heating was shown to be a likely contribution to the non-ohmic behaviour at these low temperatures.

Negative magnetoresistance was measured at all temperatures for the yarns after degassing. Without degassing, slightly positive magnetoresistance was observed above 300 K. For the annealed yarns, the magnitude of negative magnetoresistance was significantly larger at all temperatures, as has been seen previously [84].

The high-current behaviour in atmosphere up to thermal failure was measured for 50 $\mu$m CNT yarns. The pristine yarn reached a maximum current of 60 mA, whereas the annealed samples reached currents of $\sim$80 mA. The improvement in maximum current was because of the reduction in bulk defects. Failure was observed to occur suddenly, which could be detrimental to some potential applications of CNT yarns [78]. Post-failure SEM showed that failure results in a clean break of the yarn structure, vapourizing the CNTs and leaving behind no visible residue.

Thermal conductivity, $\kappa$, was measured between 50 K and 300 K under vacuum using the PTC method. The PTC method was improved in comparison to the versions used previously [5, 6] by adding a more precise current source and improving automation. As with $\sigma$, $\kappa$ was observed to be dependent on diameter, and varied from 30 $\pm$ 8 W$\cdot$m$^{-1}\cdot$K$^{-1}$ for the 35 $\mu$m pristine yarn to 15 $\pm$ 2 W$\cdot$m$^{-1}\cdot$K$^{-1}$ for the 60 $\mu$m pristine yarn. As with $\sigma$, annealing caused a monotonic increase in $\kappa$. The conductivity of the 2300 °C annealed samples improved by between 190 % to 220 % relative to the pristine samples, and the 2700 °C annealed samples improved further by between 240 % and 300 %.

The effective Lorenz number, $L_{\text{eff}}$, gives the relative contribution of phonon and electrons to the thermal conductivity of a material. For these CNT yarns, $L_{\text{eff}}$ was two orders of magnitude larger than that of an ideal metal, showing that $\kappa$ is donimated by phonons. $L_{\text{eff}}$ displayed a broad peak near 75 K, where the phonon contribution

to $\kappa$ is a maximum. This has been observed previously for other CNT materials [4, 5, 6]. After annealing, the peak in $L_{\text{eff}}$ became more pronounced, likely because the improvement in crystallinity had a larger affect on the phonon mean free path and the electron mean free path, and therefore the increase in the phonon contribution to $\kappa$ was more significant.

In conclusion, high-temperature annealing of CNT yarns was found to improve their crystallinity, electrical conductivity, and thermal conductivity. This work showed that annealing could be a viable method to improve the properties of dry-spun CNT yarns, and that Raman spectroscopy could be used to rapidly assess the relative conductivities of CNT materials.

The thermal conductivities of various BNNT materials and small-diameter CNT fibres were also measured using the parallel thermal conductance method.

The apparent thermal conductivity of pristine BNNT sheets and buckypapers were found to be $\sim$0.65 $\pm$ 0.06 W$\cdot$m$^{-1}\cdot$K$^{-1}$ and 1.3 $\pm$ 0.2 W$\cdot$m$^{-1}\cdot$K$^{-1}$, respectively. The density corrected thermal conductivities of BNNT sheets and buckypapers were found to all be on the order of $\sim$4 W$\cdot$m$^{-1}\cdot$K$^{-1}\cdot$cm$^{-1}\cdot$g$^{-1}$, suggesting that the conductivities of the individual BNNTs in each material are similar. The thermal conductivities of two BNNT/polymer composites had $T = 300$ K conductivities of 2.7 $\pm$ 0.3 W$\cdot$m$^{-1}\cdot$K$^{-1}$ and 2.2 $\pm$ 0.2 W$\cdot$m$^{-1}\cdot$K$^{-1}$. These results are the first known direct measurements of thermal conductivity for bulk BNNT materials.

The thermal conductivities of two reactor-spun $\sim$10 $\mu$m CNT fibres prepared from methane and toluene precursors were found to be 460 $\pm$ 50 W$\cdot$m$^{-1}\cdot$K$^{-1}$ and 560 $\pm$ 60 W$\cdot$m$^{-1}\cdot$K$^{-1}$ at 300 K. These values are the highest known thermal conductivities reported to date for CNT fibres [76].

In future work, efforts could be made to improve the PTC method. The background conductance should be reduced to improve the relative contribution of the

sample to the measured conductance. This would improve the accuracy of the measurement and also allow for the thermal conductivity of smaller diameter or lower conductance samples to be measured over a larger temperature range. Furthermore, an improved technique would be developed for the sample mounting process for the PTC method. This would improve consistency between different samples, and make the mount process faster. Effort could also be made to make the PTC method data collection more automated.

Other nanotube materials could also be studied. For example, a variety of CNT sheets have been provided by the Prof. Alan Windle's group for both thermal conductivity and electrical conductivity measurements. This work will investigate the influence of various precursor carbon gases, as well as geometric influences (width and thickness) on the transport properties of CNT sheets.

## References


[1] M.-F. Yu, O. Lourie, M. J. Dyer, K. Moloni, T. F. Kelly, and R. S. Ruoff. Strength and Breaking Mechanism of Multiwalled Carbon Nanotubes Under Tensile Load. *Science* 287 (2000), pp. 637–640.

[2] E. Pop, D. Mann, Q. Wang, K. Goodson, and H. Dai. Thermal Conductance of an Individual Single-Wall Carbon Nanotube above Room Temperature. *Nano Letters* 6.1 (2006), pp. 96–100.

[3] T. W. Ebbesen, H. J. Lezec, H. Hiura, J. W. Bennett, H. F. Ghaemi, and T. Thio. Electrical conductivity of individual carbon nanotubes. *Nature* 382 (1996), pp. 54–56.

[4] M. B. Jakubinek, M. A. White, G. Li, C. Jayasinghe, W. Cho, M. J. Schulz, and V. Shanov. Thermal and electrical conductivity of tall, vertically aligned carbon nanotube arrays. *Carbon* 48 (2010), pp. 3947–3952.

[5] J.-H. Pöhls, M. B. Johnson, M. A. White, R. Malik, B. Ruff, C. Jayasinghe, M. J. Schulz, and V. Shanov. Physical properties of carbon nanotube sheets drawn from nanotube arrays. *Carbon* 50.11 (2012), pp. 4175–4183.

[6] M. B. Jakubinek, M. B. Johnson, M. A. White, C. Jayasinghe, G. Li, W. Cho, M. J. Schulz, and V. Shanov. Thermal and electrical conductivity of array-spun multi-walled carbon nanotube yarns. *Carbon* 50.1 (2012), pp. 244–248.

[7] M. A. White. *Physical Properties of Materials*. 2nd ed. CRC Press, 2012.

[8] C. Kittel. *Introduction to Solid State Physics*. 8th ed. John Wiley & Sons, Inc., 2005.

[9] R. Saito, G. Dresselhaus, and M. S. Dresselhaus. *Physical Properties of Carbon Nanotubes*. Imperial College Press, 1998.

[10] A. B. Kaiser. Electronic transport properties of conducting polymers and carbon nanotubes. *Reports on Progress in Physics* 64 (2001), pp. 1–49.

[11] A. Bachtold, C. Strunk, J.-P. Salvetat, J.-M. Bonard, L. Forró, T. Nussbaumer, and C. Schönenberger. Aharonov-Bohm oscillations in carbon nanotubes. *Nature* 397 (1999), pp. 673–675.

[12] A. A. Bright. Negative magnetoresistance of pregraphitic carbons. *Physical Review B* 20.12 (1979), pp. 5142–5149.

[13] B. Kramer and A. MacKinnon. Localization: Theory and Experiment. *Reports on Progress in Physics* 12.1993 (56), pp. 1469–1564.

[14] J. Chen, J. Shan, T. Tsukada, F. Munekane, A. Kuno, M. Matsuo, T. Hayashi, Y. Kim, and M. Endo. The structural evolution of thin multi-walled carbon nanotubes during isothermal annealing. *Carbon* 45 (2007), pp. 274–280.

[15] M. B. Johnson and M. A. White. *Inorganic Materials: Multi Length-Scale Characterisation*. Ed. by D. W. Bruce, D. O'Hare, and R. I. Walton. Wiley, 2014.

[16] S. Iijima. Helical microtubules of graphitic carbon. *Nature* 354 (1991), pp. 56–58.

[17] M. Reibold, P. Paufler, A. A. Levin, W. Kochmann, N. Pätzke, and D. C. Meyer. Carbon nanotubes in an ancient Damascus sabre. *Nature* 444 (2006), p. 286.

[18] J.-C. Charlier, X. Blase, and S. Roche. Electronic and transport properties of nanotubes. *Reviews of Modern Physics* 79 (2007), pp. 677–732.

[19] D. Fathi. A Review of Electronic Band Structure of Graphene and Carbon Nanotubes Using Tight Binding. *Journal of Nanotechnology* 2011 (2011), pp. 1–6.

[20] S. Berber, Y.-K. Kwon, and D. Tománek. Unusually High Thermal Conductivity of Carbon Nanotubes. *Physical Review Letters* 84.20 (2000), pp. 4613–4616.

[21] J. Hone, M. Whitney, C. Piskoti, and A. Zettl. Thermal conductivity of single-walled carbon nanotubes. *Physical Review B* 59.4 (1999), pp. 2514–2516.

[22] A. Jorio, G. Dresselhaus, and M. S. Dresselhaus, eds. *Topics in Applied Physics: Carbon Nanotubes*. Vol. 111. Springer, 2008.

[23] N. Mingo and D. A. Broido. Carbon Nanotube Ballistic Thermal Conductance and Its Limits. *Physical Review Letters* 95 (2005), p. 096105.

[24] A. M. Marconnet, M. A. Panzer, and K. E. Goodson. Thermal conduction phenomena in carbon nanotubes and related nanostructured materials. *Reviews of Modern Physics* 85 (2012), pp. 1295–1326.

[25] A. E. Aliev, M. H. Lima, E. M. Silverman, and R. H. Baughman. Thermal conductivity of multi-walled carbon nanotube sheets: radiation losses and quenching of phonon modes. *Nanotechnology* 21 (2010), p. 035709.

[26] J. Chen, T. Çağin, and W. A. G. III. Thermal conductivity of carbon nanotubes. *Nanotechnology* 11 (2000), pp. 65–69.

[27] X. H. Yan, Y. Xiao, and Z. M. Li. Effects of intertube coupling and tube chirality on thermal transport of carbon nanotubes. *Journal of Applied Physics* 99 (2006), p. 123405.

[28] M. J. Schulz, V. N. Shanov, and Z. Yin. *Nanotube Superfiber Materials*. Elsevier, 2014.

[29] G. D. Nessim. Properties, synthesis, and growth mechanisms of carbon nanotubes with special focus on thermal chemical vapor deposition. *Nanoscale* 2 (2010), pp. 1306–1323.

[30] K. Balasubramanian and M. Brghard. Chemically Functionalized Carbon Nanotubes. *Small* 1.2 (2005), pp. 180–192.

[31] V. Shanov, W. Cho, R. Malik, M. Haase, B. Ruff, M. Kienzle, T. Ochmann, D. Mast, and M. Schulz. CVD growth, characterization and applications of carbon nanostructured materials. *Surface and Coatings Techology* 230 (2013), pp. 77–86.

[32] K. Jiang, Q. Li, and S. Fan. Spinning continuous carbon nanotube yarns. *Nature* 419 (2002), p. 801.

[33] Q. Zhang, D. G. Whang, J. Q. Huang, W. P. Zhou, G. H. Luo, and W. Z. Qian. Dry spinning yarns from vertically aligned carbon nanotube arrays produced by an improved floating catalyst chemical vapor deposition method. *Carbon* 48.10 (2010), pp. 2855–2861.

[34] A. A. Kuznetsov, A. F. Fonseca, R. H. Baughman, and A. A. Zakhidov. Structural Model for Dry-Drawing of Sheets and Yarns from Carbon Nanotube Forests. *ACS Nano* 5.2 (2011), pp. 985–993.

[35] K. Liu, Y. Sun, P. Liu, J. Wang, Q. Li, S. Fan, and K. Jiang. Periodically striped films produced from super-aligned carbon nanotube arrays. *Nanotechnology* 20 (2009), p. 335705.

[36] B. Vigolo, A. Pénicaud, C. Coulon, C. Sauder, R. Pailler, C. Journet, P. Bernier, and P. Poulin. Macroscopic Fibers and Ribbons of Oriented Carbon Nanotubes. *Science* 290.5495 (2000), pp. 1331–1334.

[37] L. M. Ericson, H. Fan, H. Peng, V. A. Davis, W. Zhou, J. Sulpizio, Y. Wang, R. Booker, J. Vavro, C. Guthy, A. N. G. Parra-Vasquez, M. J. Kim, S. Ramesh, R. K. Saini, C. Kittrell, G. Lavin, H. Schmidt, W. W. Adams, W. E. Billups, M. Pasquali, W.-F. Hwang, R. H. Hauge, J. E. Fischer, and R. E. Smalley. Macroscopic, Neat, Single-Walled Carbon Nanotube Fibers. *Science* 305.5689 (2004), pp. 1447–1450.

[38] M. E. Kozlov, R. C. Capps, W. M. Sampson, V. H. Ebron, J. P. Ferrais, and R. H. Baughman. Spinning Solid and Hollow Polymer-Free Carbon Nanotube Fibers. *Advanced Materials* 17.5 (2005), pp. 614–617.

[39] H. Zhu, C. Xu, D. Wu, B. Wei, R. Vajtai, and P. Ajayan. Direct Synthesis of Long Single-Walled Carbon Nanotube Strands. *Science* 296.5569 (2002), pp. 884–886.

[40] Y.-L. Li, I. A. Kinloch, and A. H. Windle. Direct Spinning of Carbon Nanotube Fibers from Chemical Vapor Deposition Synthesis. *Science* 304.5668 (2004), pp. 276–278.

[41] C. Jayasinghe, S. Chakrabarti, M. Schulz, and V. Shanov. Spinning yarn from long carbon nanotube arrays. *Journal of Materials Research* 26.5 (2011), pp. 645–651.

[42] N. Alvarez, P. Miller, M. Haase, N. Kienzle, L. Zhang, M. Schulz, and V. Shanov. Carbon nanotube assembly at near-industrial natural-fibre spinning rates. *Carbon* 86 (2015), pp. 350–357.

[43] M. Miao. Electrical conductivity of pure carbon nanotube yarns. *Carbon* 49 (2011), pp. 3755–3761.

[44] K. Sears, C. Skourtis, K. Atkinson, N. Finn, and W. Humphries. Focused ion beam milling of carbon nanotube yarns to study the relationship between structure and strength. *Carbon* 48 (2010), pp. 4450–4456.

[45] H. Misak and S. Mall. Investigation into microstructure of carbon nanotube multi-yarn. *Carbon* 72 (2014), pp. 321–327.

[46] B. Yakobson and L. Couchman. Persistence length and nanomechanics of random bundles of nanotubes. *Journal of Nanoparticle Research* 8 (2006), pp. 105–110.

[47] B. Smith, Z. Benes, D. Luzzi, J. Fischer, D. Walters, M. Casavant, J. Schmidt, and R. E. Smalley. Structural anisotropy of magnetically aligned single wall carbon nanotube films. *Applied Physics Letters* 77 (2000), pp. 663–665.

[48] A. Lekawa-Raus, J. Patmore, L. Kurzepa, J. Bulmer, and K. Koziol. Electrical Properties of Carbon Nanotube Based Fibers and Their Future Use in Electrical Wiring. *Advanced Functional Materials* 24 (2014), pp. 3661–3682.

[49] K. Bradley, S.-H. Jhi, P. Collins, J. Hone, M. Cohen, S. Louie, and A. Zettl. Is the Intrinsic Thermoelectric Power of Carbon Nanotubes Positive? *Physical Review Letters* 85.20 (2000), pp. 4361–4364.

[50] P. Collins, K. Bradley, M. Ishigami, and A. Zettl. Extreme Oxygen Sensitivity of Electronic Properties of Carbon Nanotubes. *Science* 287 (2000), pp. 1801–1804.

[51] A. Lekawa-Raus, K. K. K. Koziol, and A. H. Windle. Piezoresistive Effect in Carbon Nanotube Fibers. *ACS Nano* 8.11 (2014), pp. 11214–11224.

[52] A. Lekawa-Raus, L. Kurzepa, G. Kozlowski, S. C. Hopkins, M. Wozniak, D. Lukawski, B. A. Glowacki, and K. K. Koziol. Influence of atmospheric water vapour on electrical performance of carbon nanotube fibres. *Carbon* 87 (2015), pp. 18–28.

[53] P. N. Nirmalraj, P. E. Lyons, S. De, J. N. Coleman, and J. J. Boland. Electrical Connectivity in Single-Walled Carbon Nanotube Networks. *Nano Letters* 9.11 (2009), pp. 3890–3895.

[54] R. L. McCreery. *Raman Spectroscopy for Chemical Analysis*. Ed. by J. D. Winefordner. Vol. 157. Chemical Analysis. Wiley-Interscience, 2002.

[55] M. S. Dresselhaus, A. Jorio, M. Hofmann, G. Dresselhaus, and R. Saito. Perspectives on Carbon Nanotubes and Graphene Raman Spectroscopy. *Nano Letters* 10 (2010), pp. 751–758.

[56] K. Behler, S. Osswald, H. Ye, S. Dimovski, and Y. Gogotsi. Effect of thermal treatment on the structure of multi-walled carbon nanotubes. *Journal of Nanoparticle Research* 8 (2006), pp. 615–625.

[57] M. Cole, J. tsai, Y. Chiao, C. Li, and Y. Zhang. Multi-walled Carbon Nanotube Conductivity Enhancement and Band Gap Widening via Rapid Pulsed Thermal Annealing. *Fullerenes, Nanotubes and Carbon Nanostructures* 22.6 (2014), pp. 545–554.

[58] X. Zhang, Q. Li, T. G. Holesinger, P. N. Arendt, J. Huang, P. D. Kirven, T. G. Clapp, R. F. DePaula, X. Liao, Y. Zhao, L. Zheng, D. E. Peterson, and Y. Zhu. Ultrastrong, Stiff, and Lightweight Carbon-Nanotube Fibers. *Advanced Materials* 19 (2007), pp. 4198–4201.

[59] K. Liu, Y. Sun, R. Zhou, H. Zhu, J. Wang, L. Liu, S. Fan, and K. Jiang. Carbon nanotube yarns with high tensile strength made by a twisting and shrinking method. *Nanotechnology* 21 (2010), p. 045708.

[60] N. Behabtu, C. C. Young, D. E. Tsentalovich, O. Kleinerman, X. Wang, A. W. K. Ma, E. A. Bengio, R. F. ter Waarbeek, J. J. de Jong, R. E. Hoogerwerf, S. B. Fairchild, J. B. Ferguson, B. Maruyama, J. Kono, Y. Talmon, Y. Cohen, M. J. Otto, and M. Pasquali. Strong, Light, Multifunctional Fibers of Carbon Nanotubes with Ultrahigh Conductivity. *Science* 339.6116 (2013), pp. 182–186.

[61] R. Jin, Z. X. Zhou, D. Mandrus, I. N. Ivanov, G. Eres, J. Y. Howe, A. A. Puretzky, and D. B. Geohegan. The effect of annealing on the electrical and thermal transport properties of macroscopic bundles of long multi-wall carbon nanotubes. *Physica B* 388 (2007), pp. 326–330.

[62] W. Huang, Y. Wang, G. Luo, and F. Wei. 99.9% purity multi-walled carbon nanotubes by vacuum high-temperature annealing. *Carbon* 41 (2003), pp. 2585–2590.

[63] A. P. Pierlot, A. L. Woodhead, and J. S. Church. Thermal annealing effects on multi-walled carbon nanotube yarns probed by Raman spectroscopy. *Spectrochimica Acta Part A* 117 (2014), pp. 598–603.

[64] J. T. H. Tsai and A. A. Tseng. Defect reduction of multi-walled carbon nanotubes by rapid vacuum arc annealing. *Journal of Experimental Nanoscience* 4.1 (2009), pp. 87–93.

[65] G. Yamamoto, K. Shirasu, Y. Nozaka, Y. Sato, T. Takagi, and T. Hashida. Structure-property relationships in thermally-annealed multi-walled carbon nanotubes. *Carbon* 66 (2014), pp. 219–226.

[66] J. Park, M. F. P. Bifano, and V. Prakash. Sensitivity of thermal conductivity of carbon nanotubes to defect concentrations and heat-treatment. *J. Appl. Phys.* 113 (2013), p. 0340312.

[67] R. Andrews, D. Jacques, D. Qian, and E. Dickey. Purification and structural annealing of multiwalled carbon nanotubes at graphitization temperatures. *Carbon* 39 (2001), pp. 1681–1687.

[68] R. H. Hurt, M. Monthioux, and A. Kane. Toxicology of carbon nanomaterials: Status, trends, and perspectives on the special issue. *Carbon* 44 (2006), pp. 1028–1033.

[69] D. Mattia, M. P. Rossi, B. M. Kim, G. Korneva, H. H. Bau, and Y. Gogotsi. Effect of Graphitization on the Wettability and Electrical Conductivity of CVD-Carbon Nanotubes and Films. *J. Phys. Chem. B* 110 (2006), pp. 9850–9855.

[70] E. Mayhew and V. Prakash. Thermal conductivity of individual carbon nanofibers. *Carbon* 62 (2013), pp. 493–500.

[71] URL: http://www.firstnano.com/products/easytube3000/docs/ET3000.pdf.

[72] H. Romero, G. Sumanasekera, G. Mahan, and P. Eklund. Thermoelectric power of single-walled carbon nanotube films. *Physical Review B* 65 (2002), p. 205410.

[73] J.-H. Pöhls. "Physical Properties of a Carbon Nanotube Tape". Masters thesis. University of Kiel, 2011.

[74] B. M. Zawilski, R. T. Littleton, and T. M. Tritt. Description of the parallel thermal conductance technique for the measurement of the thermal conductivity of small diameter samples. *Review of Scientific Instruments* 72.3 (2001), pp. 1770–1774.

[75] A. E. Aliev, C. Guthy, M. Zhang, S. Fang, A. A. Zakhidov, J. E. Fischer, and R. H. Baughman. Thermal transport in MWCNT sheets and yarns. *Carbon* 45 (2007), pp. 2880–2888.

[76] E. Mayhew and V. Prakash. Thermal conductivity of high performance carbon nanotube yarn-like fibers. *J. Appl. Phys.* 115 (2014), p. 174306.

[77] S. Badaire, V. Pichot, C. Zakri, P. Poulin, P. Launois, J. Vavro, C. Guthy, M. Chen, and J. E. Fischer. Correlation of properties with preferred orientation in coagulated and stretch-aligned single-wall carbon nanotubes. *J. Appl. Phys.* 96.12 (2004), pp. 7509–7513.

[78] L. Song, G. Toth, J. Wei, Z. Liu, W. Gao, L. Ci, R. Vajtai, M. Endo, and P. M. Ajayan. Sharp burnout failure observed in high current-carrying double-walled carbon nanotube fibers. *Nanotechnology* 23 (2012), p. 015703.

[79] D. S. Grierson, A. V. Sumant, A. R. Konicek, T. A. Friedmann, J. P. Sullivan, and R. W. Carpick. Thermal stability and rehybridization of carbon bonding in tetrahedral amorphous carbon. *Journal of Applied Physics* 107.3 (2010), p. 033523.

[80] J. Hone, M. C. Llaguno, N. M. Nemes, and A. T. Johnson. Electrical and thermal transport properties of magnetically aligned single wall carbon nanotube films. *Applied Physics Letters* 77.5 (2000), pp. 666–668.

[81] W. Zhou, J. Vavro, C. Guthy, K. Winey, J. Fischer, L. Ericson, S. Ramesh, R. Saini, V. Davis, C. Kittrell, M. Pasquali, R. Hauge, and R. Smalley. Single wall carbon nanotube fibers extruded from super-acid suspensions: Preferred orientation, electrical, and thermal transport. *Journal of Applied Physics* 95.2 (2004), pp. 649–655.

[82] A. B. Kaiser, V. Skákalová, and S. Roth. Modelling conduction in carbon nanotube networks with different thickness, chemical treatment and irradiation. *Physica E* 40 (2008), pp. 2311–2318.

[83] A. Lekawa-Raus, K. Walczak, G. Kozlowski, M. Wozniak, S. C. Hopkins, and K. Koziol. Resistance-temperature dependence in carbon nanotube fibres. *Carbon* 84 (2015), pp. 118–123.

[84] V. L. Kuznetsov, K. V. Elumeeva, A. V. Ishchenko, N. Y. Beylina, A. A. Stepashkin, S. I. Moseenkov, L. M. Plyasova, I. Y. Molina, A. I. Romanenko, O. B. Anikeeva, and E. N. Tkachev. Multi-walled carbon nanotubes with ppm level of impurities. *Phys. Status Solidi B* 247.11-12 (2010), pp. 2695–2699.

[85] J. Barzola-Quiquia, N. Klingner, J. Krüger, A. Molle, P. Esquinazi, A. Leonhardt, and M. T. Martínez. Quantum oscillations and ferromagnetic hysteresis observed in iron filled multiwall carbon nanotubes. *Nanotechnology* 23 (2012), p. 015707.

[86] J. Barzola-Quiquia, P. Esquinazi, M. Lindel, D. Spemann, M. Muallem, and G. Nessim. Magnetic order and superconductivity observed in bundles of double-wall carbon nanotube. *Carbon* 88 (2015), pp. 16–25.

[87] P. Kim, L. Shi, A. Majumdar, and P. L. McEuen. Thermal Transport Measurements of Individual Multiwalled Nanotubes. *Physical Review Letters* 87.21 (2001), p. 215502.

[88] G. Ventura and V. Martelli. Thermal conductivity of Kevlar 49 between 7 and 290 K. *Cryogenics* 49 (2009), pp. 735–737.

[89] M. Locatelli and A. M. Routin. Thermal conductivity of some insulating materials materials below 1 K. *Cryogenics* 16.6 (1976), pp. 374–375.

[90] T. Gspann, F. Smail, and A. Windle. Spinning of carbon nanotube fibres using the floating catalyst high temperature route: purity issues and the critical role of sulphur. *Faraday Discussions* 173.47 (2014), pp. 47–65.

[91] D. T. Gspann. Private communications. 2015.

[92] D. Golberg, Y. Bando, C. Tang, and C. Zhi. Boron Nitride Nanotubes. *Advanced Materials* 19 (2007), pp. 2413–2432.

[93] R. Arenal, X. Blase, and A. Loiseau. Boron-nitride and boron-carbonitride nanotubes: synthesis, characterization and theory. *Advances in Physics* 59.2 (2010), pp. 101–179.

[94] N. Chopra, R. Luyken, K. Cherrey, V. Crespi, M. Cohen, S. Louie, and A. Zettl. Boron Kitride Nanotubes. *Science* 269.5226 (1995), pp. 966–967.

[95] Y. Xiao, X. H. Yan, J. Xiang, Y. L. Mao, Y. Zhang, J. X. Cao, and J. W. Ding. Specific heat of single-walled boron nitride nanotubes. *Applied Physics Letters* 84.23 (2004), pp. 4626–4628.

[96] N. G. Chopra and A. Zettl. Measurement of the elastic modulus of a multi-wall boron nitride nanotube. *Solid State Communications* 105.5 (1998), pp. 297–300.

[97] X. Blase, A. Rubio, S. Louie, and M. Cohen. Stability and Band Gap Constancy of Boron Nitride Nanotubes. *Europhysics Letters* 28.5 (1994), pp. 335–340.

[98] H. Chen, Y. Chen, Y. Liu, L. Fu, C. Huang, and D. Llewellyn. Over 1.0 mm-long boron nitride nanotubes. *Chemical Physics Letters* 463 (2008), pp. 130–133.

[99] Y. Chen, J. Zou, S. J. Campbell, and G. L. Caer. Boron nitride nanotubes: Pronounced resistance to oxidation. *Applied Physics Letters* 84.13 (2004), pp. 2430–2432.

[100] C. Chang, A. Fennimore, A. Afanasiev, D. Okawa, T. Ikuno, and H. Garcia. Isotope effect on the thermal conductivity of boron nitride nanotubes. *Physical Review Letters* 97 (2006), p. 085901.

[101] D. P. Yu, X. S. Sun, C. S. Lee, I. Bello, S. T. Lee, H. D. Gu, K. M. Leung, G. W. Zhou, Z. F. Dong, and Z. Zhang. Synthesis of boron nitride nanotubes by means of excimer laser ablation at high temperature. *Applied Physics Letters* 72 (1998), pp. 1966–1968.

[102] Y. Chen, J. F. Gerald, J. Williams, and S. Bulcock. Synthesis of boron nitride nanotubes at low temperatures using reactive ball milling. *Chemical Physics Letters* 299.3 (1999), pp. 260–264.

[103] J. Cumings and A. Zettl. Mass-production of boron nitride double-wall nanotubes and nanococoons. *Chemical Physics Letters* 316 (2000), pp. 211–216.

[104] R. Sen, B. Satishkumar, A. Govindaraj, K. Harikumar, G. Raina, J.-P. Zhang, A. Cheetham, and C. Rao. B–C–N, C–N and B–N nanotubes produced by the pyrolysis of precursor molecules over Co catalysts. *Chemical Physics Letters* 287 (1998), pp. 671–676.

[105] C. Lee, S. Choi, S. Choi, and S. Hong. Synthesis of boron nitride nanotubes by arc-jet plasma. *Current Applied Physics* 6.2 (2006), pp. 166–170.

[106] T. Laude, Y. Matsui, A. Marraud, and B. Jouffrey. Long Ropes of Boron Nitride Nanotubes Grown by a Continuous Laser Heating. *Applied Physics Letters* 76 (2000), pp. 3239–3241.

[107] K. S. Kim, C. T. Kingston, A. Hrdina, M. B. Jakubinek, J. Guan, M. Plunkett, and B. Simard. Hydrogen-Catalyzed, Pilot-Scale Production of Small-Diameter Boron Nitride Nanotubes and Their Macroscopic Assemblies. *ACS Nano* 8.6 (2014), pp. 6211–6220.

[108] M. W. Smith, K. C. Jordan, C. Park, J.-W. Kim, P. T. Lillehei, R. Crooks, and J. Harrison. Very long single- and few-walled boron nitride nanotubes via the pressurized vapor/condenser method. *Nanotechnology* 20 (2009), p. 505604.

[109] L. H. Li and Y. Chen. Superhydrophobic Properties of Nonaligned Boron Nitride Nanotube Films. *Langmuir* 26.7 (2009), pp. 5135–5140.

[110] T. Terao, C. Zhi, Y. Bando, M. Mitome, C. Tang, and D. Golberg. Alignment of Boron Nitride Nanotubes in Polymeric Composite Films for Thermal Conductivity Improvement. *J. Phys. Chem. C* 114 (2010), pp. 4340–4344.

[111] K. S. Kim, M. B. Jakubinek, Y. Martinez-Rubi, B. Ashrafi, J. Guan, K. O'Neill, M. Plunkett, A. Hrdina, S. Lin, S. Dénommée, C. Kingston, and B. Simard. Polymer nanocomposites from free-standing, macroscopic boron nitride nanotube assemblies. *RSC Advances* 5 (2015), pp. 41186–41192.

[112] M. B. Jakubinek. "Thermal and electrical conductivity of carbon nanotube materials". PhD thesis. Dalhousie University, 2009.

[113] M. B. Jakubinek, B. Ashrafi, J. Guan, M. B. Johnson, M. A. White, and B. Simard. 3D chemically cross-linked single-walled carbon nanotube buckypapers. *RSC Advances* 4 (2014), pp. 57564–57573.

[114] C. W. Chang, W.-Q Han, and A. Zettl. Thermal conductivity of B-C-N and BN nanotubes. *Applied Physics Letters* 86 (2005), p. 173102.